

# UC Riverside

## UC Riverside Electronic Theses and Dissertations

### Title

A Study of Massive and Evolved Galaxies at  $z > 3$

### Permalink

<https://escholarship.org/uc/item/7379d0g5>

### Author

Nayyeri, Hooshang

### Publication Date

2014

Peer reviewed|Thesis/dissertation

UNIVERSITY OF CALIFORNIA  
RIVERSIDE

A Photometric and Spectroscopic Study of Massive and Evolved Galaxies at  $z > 3$

A Dissertation submitted in partial satisfaction  
of the requirements for the degree of

Doctor of Philosophy

in

Physics

by

Hooshang Nayyeri

December 2014

Dissertation Committee:

Dr. Bahram Mobasher, Chairperson  
Dr. Gillian Wilson  
Dr. Brian Siana

The Dissertation of Hooshang Nayyeri is approved:

---

---

---

Committee Chairperson

University of California, Riverside

## Acknowledgements

Here I wish to take the opportunity to thank everyone that helped me during my academic career. I wish to thank my parents for giving me the opportunity to pursue my studies to this level and my family for always supporting me in different circumstances.

My greatest appreciation and thank goes to my mentor Professor Bahram Mobasher. It was only through his constant support and guidance that I was able to achieve this and it was through all the memorable science discussions that I got ever more interested in Astronomy. I am forever indebted to him for all of this.

I am very grateful to my dissertation committee members Dr. Brian Siana and Dr. Gillian Wilson for reading this dissertation in detail and providing very useful comments and suggestions. I wish to additionally thank Brian for the very useful science discussions that we had during the journal clubs and in the hallways.

I wish to thank all my friends in Riverside that made graduate school a very fun experience for me. Special thanks goes to Shoubaneh Hemmati for this and the very useful discussions that we always had. I also wish to acknowledge the very interesting discussions that I had from time to time with Behnam Darvish in science and beyond!

Particularly memorable coffee break dialogs with Shoubaneh Hemmati, Behnam Darvish, Irene Shivaie and Mostafa Khezri were always a good distraction from the hardships of graduate work. I am very thankful for their friendship.

I finally wish to thank Mark Dickinson and Henry Ferguson for their guidance and support throughout my graduate work for which I am exceptionally grateful.

This work is partly based on research that is published in the *Astrophysical Journal* (ApJ, 794, 68).

To my parents.

## ABSTRACT OF THE DISSERTATION

A Photometric and Spectroscopic Study of Massive and Evolved Galaxies at  $z > 3$

by

Hooshang Nayyeri

Doctor of Philosophy, Graduate Program in Physics  
University of California, Riverside, December 2014  
Dr. Bahram Mobasher, Chairperson

I use deep data taken as part of the Hubble Space Telescope (HST) Wide Field Camera 3 (WFC3) observations by the Cosmic Assembly Near-infrared Deep Extragalactic Legacy Survey (CANDELS) along with ground-based and Spitzer Space Telescope data to identify massive and evolved galaxies at  $z > 3$ . This is performed using the strength of the Balmer break feature at rest-frame  $3648\text{\AA}$  which is an age dependent diagnostic of the stellar population, to develop a Balmer Break Galaxy (BBG) selection. Fitting the spectral energy distribution (SED) of the candidates show that these systems have average estimated ages of  $\sim 800$  Myr and average stellar masses of  $\sim 5 \times 10^{10} M_{\odot}$ , consistent with being old and massive. I find a number density of  $\sim 3.2 \times 10^{-5} Mpc^{-3}$  for these systems corresponding to a mass density of  $\sim 2.0 \times 10^6 M_{\odot}/Mpc^3$  at  $3 < z < 4.5$ . Given the old age and the passive evolution, it is argued that some of these objects formed the bulk of their mass only a few hundred million years after the Big Bang and could be the descendants of the highly star forming galaxies at very high redshifts. I follow up sources identified through BBG selection with the Keck Telescope DEIMOS optical spectrograph and confirm several of these systems at  $z \sim 3 - 4$ . The stacked spectrum of BBGs shows relatively stronger metal absorption features and relatively smaller velocity offsets from the systemic with respect to the LBG

selected star forming galaxies. This seems to indicate that the passive systems are less dominated by outflows that are characteristics of star forming systems at high redshifts. I measure the sizes of these systems and find that the most massive old galaxies in the Universe at  $z \gtrsim 3$  are far more compact than lower redshift early type galaxies. Using the GALFIT measured sizes, I confirm that the physical size of the early type galaxies evolve rapidly with redshift according to:  $R_e \propto (1+z)^{-1.48}$  out to  $z \sim 3.3$ .

# Contents

<b>1</b>	<b>Introduction</b>	<b>1</b>
1.1	The Search for High Redshift Galaxies . . . . .	1
1.1.1	The Lyman Break Selection . . . . .	1
1.1.2	The Formation of the Red Sequence . . . . .	3
1.2	Hierarchical Models of Galaxy Formation . . . . .	6
1.3	Massive and Old Galaxies at High Redshifts . . . . .	8
1.4	Thesis Plan . . . . .	9
<b>2</b>	<b>Photometric Data</b>	<b>10</b>
2.1	Introduction . . . . .	10
2.2	Data . . . . .	11
2.2.1	HST Observations . . . . .	12
2.2.2	Ground-based Observations . . . . .	13
2.2.3	Spitzer InfraRed Observations . . . . .	13
2.3	Photometry . . . . .	16
2.3.1	HST Photometry . . . . .	16
2.3.2	The hot + cold mode . . . . .	17
2.3.3	Low Resolution Photometry . . . . .	19
2.4	Data Quality Checks . . . . .	20
2.4.1	Color Validation Check . . . . .	20
2.4.2	Photometry Validation Check . . . . .	25

2.5	Conclusion and Summary . . . . .	26
<b>3</b>	<b>A Study of Massive and Evolved Galaxies at High Redshift</b>	<b>29</b>
3.1	Introduction . . . . .	29
3.2	The Photometric Data . . . . .	31
3.3	BBG Selection Criteria . . . . .	33
3.3.1	Color-Color selection method . . . . .	33
3.3.2	Simulations . . . . .	37
3.3.3	Candidate Identification from the color-color Criteria . . . . .	40
3.3.4	Effect of Nebular Emission on the BBG Selection . . . . .	45
3.4	Measurements of the Observable Parameters . . . . .	48
3.4.1	Effect of Nebular Emission on Parameter Estimation . . . . .	50
3.4.2	Photometric Redshift . . . . .	54
3.4.3	Mass Measurement . . . . .	54
3.4.4	Extinction . . . . .	54
3.4.5	Age . . . . .	55
3.5	MIPS detected BBGs . . . . .	55
3.6	Comparison between the sources selected by the LBG and BBG techniques	56
3.7	Discussion . . . . .	62
<b>4</b>	<b>Morphology of Passive Galaxies at <math>z &gt; 3</math></b>	<b>67</b>
4.1	Introduction . . . . .	67
4.2	Sample and Data . . . . .	69
4.3	Size Measurements of Passive Galaxies . . . . .	70
4.3.1	The Mass-Size Relation for Passive Galaxies . . . . .	75
4.3.2	Size Evolution of Massive Galaxies with Redshift . . . . .	76
4.4	Discussion . . . . .	77

<b>5</b>	<b>Spectroscopic Study of Passive Galaxies at <math>z &gt; 3</math></b>	<b>82</b>
5.1	Introduction . . . . .	82
5.2	Spectroscopic Candidates and Data . . . . .	84
5.2.1	Passive Candidates . . . . .	84
5.2.2	Star forming Candidates . . . . .	84
5.2.3	Spectroscopic Data . . . . .	85
5.2.4	Photometric Data . . . . .	86
5.3	Analyzing the Spectroscopic Data . . . . .	86
5.3.1	Spectroscopic Data Reduction . . . . .	86
5.3.2	Spectroscopic Redshift Assignments . . . . .	87
5.3.3	Comparing the Photometric and Spectroscopic Redshifts . . . . .	90
5.3.4	Stacking the Spectra . . . . .	90
5.4	Spectroscopic Properties of the Passive and Star Forming Systems . . . . .	92
5.4.1	Equivalent Width Measurements and Velocity Offsets . . . . .	92
5.4.2	Error Estimation For the Stacked Spectra . . . . .	97
5.4.3	Caveats . . . . .	98
5.5	Discussion . . . . .	99
<b>6</b>	<b>Conclusions</b>	<b>105</b>
	<b>References</b>	<b>110</b>

# List of Figures

1.1	The mean cosmic transmission for a source at redshifts 3, 4 and 5 (solid lines from left to right) demonstrating the drop in the restframe UV flux as it travels through the neutral Hydrogen. The ACS filter throughputs are also plotted as dashed/dotted lines. The plot is adopted from Madau et al., 1996.	3
1.2	The Lyman Break Galaxy (LBG) selection criteria (also known as the UGR selection for the filters used) developed by Steidel et al., 1999 to identify star forming galaxies at $z \sim 3$ . The three different redshift dependent color evolutionary tracks are drawn for star forming galaxies with three different values of extinction. . . . .	4
1.3	The color magnitude distribution of the local galaxies in the Sloan Digital Sky Survey (SDSS). The galaxies are color coded based on the spectral type with the red corresponding to early type, blue corresponding to late type and green corresponding to bulge galaxies (Sa-Sb). The contours are for equal densities and the solid line shows the empirical separation between the red sequence and the other galaxies. The plot is adopted from Gavazzi et al., 2010.	5
1.4	The (U-V) vs (V-J) color-color diagram (also know as the UVJ diagram) from Williams et al., 2009 used for separating the star forming and quiescent galaxies based on the 4000Å/Balmer break. The quiescent galaxies are shown in red as objects with very low Specific Star Formation Rates (star formation rate per unit mass). . . . .	6

1.5	The galaxy merger tree as discussed in Lacey and Cole, 1993 showing the growth of the dark matter halos with time. Time is on the y-axis with the present time at the bottom of the plot. Each horizontal cut in the plot shows the distribution of the halos at a given time. . . . .	7
2.1	The transmission curves of the optical, near infrared and infrared filters in the CANDELS GOODS-S. . . . .	12
2.2	The outline of the CANDELS GOODS-S HST/WFC3 observations (Grogin et al., 2011).The CANDELS Early Release Science is shown in red while the Deep and Wide areas are shown in blue and green respectively. . . . .	14
2.3	The sky coverage of the survey in the GOODS-S field. The gray shaded area shows the exposure map of observations in the WFC3 F160W band. The IRAC coverage is from deep observations of the GOODS-S by the SEDS progma (Spitzer warm mission; Ashby et al., 2013). . . . .	16
2.4	The hot and cold mode detected sources in the GOODS-S. The cold mode selected sources are shown blue. These are relatively local high surface brightness extended sources. The hot mode selected source sources are shown in red. These are small low surface brightness objects that are identified by setting low detection thresholds and areas in the SExtractor input parameters. The final sources in the catalog are shown with green circles in the figure. These are identified from the combination of hot and cold mode selected sources using the routine developed for GALAPAGOS. The yellow region shows an area were multiple hot detected sources would only lead to one detected source in the final catalog according to the combination routine.	18

2.5	The stacked ACS selection image (top left) along with sample TFIT residual maps in the VLT/ISAAC J and Ks and the Spitzer IRAC infrared. Sources that are well separated in the high resolution ACS image could well be blended in the lower resolution images. The residuals left in the images are mostly for objects with very centrally concentrated light for which the PSF used is under-subtracting the core (white region at the center) and over-subtracting the wings (dark regions at the wings). . . . .	21
2.6	BzK color-color plots (Daddi et al., 2004) and the extensions of the color selection to higher redshifts (the so-called VJL and iHM selection; Guo et al., 2012) showing the distribution of the star-forming and passive galaxies. The dashed line shows the expected position of stars on the color-color plot. The stars in the field are shown with red circles on the plot. . . . .	22
2.7	The (J-Ch1) vs (V-J) color-color plot (VJL) developed by Guo et al., 2012 used to separate the star forming and passive population at $z \sim 3$ . The red circles are the observed color of the stars which agrees with the locus predicted by Guo et al., 2012 for point source objects. . . . .	23
2.8	The (H-Ch2) vs (i-H) color-color plot (iHM) used at $z \sim 4$ with the red circles showing the our measured colors of the stars in the field. This agrees with the predictions by Guo et al., 2012 for the stellar locus. . . . .	24
2.9	The color-color diagrams showing the color of stars in the GOODS-S field (yellow). The color of observed stars is consistent with the color of model stars from the BaSeL library (shown in black). . . . .	26
2.10	ACS Stacked photometry comparison with the CANDELS H-band selected catalog. The dashed magenta line shows the median difference between our magnitudes and that of the H-band selected catalog in bins of 0.25 magnitudes. The red points show the stellar locus on the diagrams. . . . .	27

3.1	A post-starburst galaxy template SED ( $F_\lambda$ ) at $z = 3.9$ (black) with the WFC3 $H_{160}$ (blue) and HAWK-I $K_s$ filters (red) straddling the Balmer break at observed $1.8 \mu m$ (the plots have been normalized to a peak of one). . . .	34
3.2	$(Y - J)$ versus $(H - K_s)$ (left) and $(J - H)$ versus $(H - K_s)$ (right) evolutionary tracks from BC03 models. In both plots solid red, solid blue and dashed black evolutionary tracks represent elliptical, dusty starburst and post starburst galaxies respectively. The parameters used to generate the model tracks are listed in Table 3.1. The yellow and red circles on the post-starburst galaxy tracks correspond to redshifts 3.0 and 4.5 respectively. The BBG selection criteria is identified by the grey shaded area on the plots. . . . .	38
3.2	Continued. . . . .	39
3.3	Simulation color-color diagrams. The blue, red and green data points correspond to elliptical, dusty starburst and post starburst galaxies from our simulation respectively with the BBG selection shown as grey shaded area. Although we get very little contamination from the lower redshift early type galaxies (red points), the dusty star-forming systems could still contaminate the sample (blue points). . . . .	41
3.3	Continued. . . . .	42
3.4	Left: The $(Y - J)$ vs $(H - K_s)$ selection criteria (Eq. 1) applied to the CANDELS WFC3 $H$ -band selected TFIT data (black data points). Right: Plot of $(J - H)$ vs $(H - K_s)$ (Eq. 2). Blue circles correspond to the selected candidates that lie within the selection criteria and are not detected in the U and B bands (i.e., are at $z \sim 3$ and $z \sim 4$ ). The red triangles are the UVJ selected passive systems by Straatman et al., 2014. The final candidates are from the two combined color-color plots. . . . .	43
3.4	Continued. . . . .	44

3.5	Distribution of the near infrared color selected BBG sources on the rest-frame UVJ color selection criteria (Williams et al., 2009). The area on the plot shows the UVJ predicted location for quiescent galaxies. The BBG selected sources fall close to the boundary of dusty star forming and quiescent candidates. . . . .	46
3.6	Example of an SED fit to a BBG candidate at $z=3.60$ without nebular emission (green) and with nebular emission (blue). This shows the extent to which nebular emission could mimic the Balmer break feature shifted to near IR. . . . .	48
3.7	Top: The observed IRAC colors of the 4 BBG candidates with strong contribution from the $H\alpha$ shifted to the infrared pass-bands are plotted against the best fit model color with no nebular emission contributions incorporated in the fit. Bottom: Same as the left plot but with nebular emission added to the fit. . . . .	49
3.8	Comparison of the stellar mass values for BBGs estimated with and without including nebular emission contribution. The blue filled circles correspond to sources with an age estimate difference of larger than 0.5 dex in fits with and without nebular emission. . . . .	51
3.9	The age distribution of BBGs shown with filled symbols in Figure 3.8. The red histogram shows the age distribution of these sources without nebular emission added to the SED fit and the blue histogram is the age distribution with the nebular emission effect added to the fit. These are the galaxies for which both their age and stellar masses are sensitive to the inclusion of nebular emission lines. Clearly including nebular emission lines leads to younger ages and lower stellar mass estimates. . . . .	52

3.10	Postage stamp images of the BBG candidates. From left to right, the VLT/VIMOS U band, ACS optical, WFC3 near-IR, VLT/HAWKI $K_s$ , Spitzer IRAC and MIPS 24 micron bands. The candidates are very faint in the bluer bands and get brighter in the redder bands. Three of the candidates are marginally detected in the MIPS 24 $\mu\text{m}$ . The cutouts are $5'' \times 5''$ in size. . . . .	53
3.11	Properties of the BBG candidates selected from the color-color criteria. From left to right: Photometric redshift distribution showing that most of the color selected BBGs has Phot-z distributions that are consistent with the redshift range of interest here. Mass distribution showing that the BBG selection is targeting the more massive galaxy population. Age distribution indicating that our selection targets evolved systems. Extinction distribution showing the range of reddening values. . . . .	57
3.12	Distribution of the properties for the LBGs (blue) and BBGs (red) in the GOODS-S from the same photometric catalog. The distributions had been normalized. Both populations are selected in the same redshift range. From the distribution, we see that the BBG selection is targeting a more evolved and massive population than the LBG selection. . . . .	58
3.13	The stacked best-fit template SED of the BBG candidates (red) and the LBGs (blue) both normalized to the flux at 2000 $\text{\AA}$ . The LBGs are distinguishable from BBGs by having bright rest-frame UV and strong nebular emission lines.	59
3.14	Optical color-color plot of LBG B drop out selection. The color selected BBG sources are plotted as black points and the color selected BBG sources that are also identified as an LBG are plotted as blue. The arrows represent $2\sigma$ upper limits on the ACS bands for the optically faint BBGs. The B drop out selection criteria is identified as the shaded area. . . . .	60

4.1	The CANDELS $H_{F160}$ band cutouts of the BBGs (left), GALFIT models (middle) and residual maps (right). The models are generated by fitting a single Sersic function as described in section 5.3 (double Sersic for #12178). The residual maps are the model subtracted images of the galaxy. The galaxy cutouts are $\sim 5'' \times 5''$ in size. . . . .	71
4.1	Continued. . . . .	72
4.1	Continued. . . . .	73
4.1	Continued. . . . .	74
4.2	The size-mass evolution of star-forming and quiescent galaxies in the CANDELS GOODS-S at $z \gtrsim 3$ . The old and massive BBG sources are show in red and the star-forming LBG sources are plotted in blue. The LBGs are binned in mass and each point represents the median in each bin. The dashed line corresponds to the size-mass relation for local early type galaxies in the SDSS by (Shen et al., 2003). I see that the BBGs are generally more compact than the local relation. The dashed-dotted line shows the size-mass relation for the late type star-forming galaxies by (van der Wel et al., 2014) at $z \sim 2.5$ . The subplots show the distribution of mass and size for the two populations. . . . .	78
4.3	The size evolution relation for passive (red triangle) and star-forming galaxies (blue square). The star-forming galaxies LBG and GALEX selected UV bright systems (Mosleh et al., 2011) and the low redshift quiescent galaxies is a from a sample by van Dokkum et al., 2008. The quiescent galaxy size is reported as the median size of the most massive non-MIPS detected BBG galaxies at the median redshift of the sample and is shown by the yellow star. The size-redshift relation for the quiescent galaxies is given by $R_e \propto (1+z)^{-1.48}$ and is shown by the dashed line. . . . .	79
5.1	Reduced DEIMOS 1D and 2D spectra of a sample galaxy at $z \sim 4.5$ . The $\text{Ly}\alpha$ emission at $6994 \text{ \AA}$ is visible in both spectra. . . . .	88

5.2	The photometric and spectroscopic redshift comparison for the passive galaxy candidates. The plot is color coded in terms of the assigned spectroscopic redshift confidence. . . . .	91
5.3	The stacked spectra of quiescent (BBG selected) and star forming (LBG and LAE) galaxies at $z > 3$ . . . . .	93
5.3	Continued. . . . .	94
5.4	The Lyman- $\alpha$ emission in the stacked spectra of BBG, LBG and LAE galaxies. We see that Ly $\alpha$ is shifted with respect to the systemic redshift of the galaxy. . . . .	95
5.5	The high ionization absorption in the stacked spectra of BBG, LBG and LAE galaxies. . . . .	96
5.6	The low ionization absorption in the stacked spectra of BBG, LBG and LAE galaxies. . . . .	96
5.7	The stacked BBG spectrum with the standard deviation shown in green. The SiII absorption (1260 Å) is detected with $\sim 3\sigma$ . . . . .	98

# List of Tables

2.1	Summary of the GOODS-S CANDELS Broad-Band Data. . . . .	15
3.1	Parameters used for the model evolutionary tracks. . . . .	35
3.2	List of the color-selected BBG candidates in the CANDELS GOODS-S. . .	66
4.1	GALFIT best fit Sersic parameters for the BBGs. . . . .	75
5.1	The Keck/DEIMOS Observations Summary. . . . .	101
5.2	List of the high confidence BBG selected old and massive systems. . . . .	102
5.3	List of lower confidence BBGs. . . . .	102
5.4	List of the star forming LBG selected galaxies. . . . .	103
5.5	List of the Ly $\alpha$ emitters. . . . .	104

# Chapter 1

## Introduction

### 1.1 The Search for High Redshift Galaxies

Before the advent of the Hubble Space Telescope (HST), with its unprecedented resolution, very sensitive CCDs and infrared detectors, and the introduction of the largest ground-based observatories with their immense light collecting capabilities, the study of the most distant objects in the Universe was very limited or impossible. The Hubble Space Telescope made it possible to not only find the most distant objects in the Universe but to also understand their physical properties in detail. The detailed spectroscopic observations by the largest ground based telescopes (such as the W. M. Keck 10 meter telescope) opened up new possibilities for studying galaxy evolution and formation back to only a few hundred million years after the Big Bang. In this section I will briefly discuss the efforts made for finding and studying the most distant objects in the very early Universe.

#### 1.1.1 The Lyman Break Selection

The Universe is almost entirely made of Hydrogen. The Hydrogen is found in its neutral (HI), ionized (HII) or molecular form and exists in the stars that make galaxies, in the medium between stars (the Inter-Stellar Medium; ISM) and in the space between galaxies

(Inter-Galactic Medium; IGM). The Hydrogen has an ionization potential of -13.6 eV and can get ionized or excited by the UV radiation from star formation in galaxies.

The Hydrogen atomic transition wavelengths is given by the following equation:

$$1/\lambda = R_H (1/n_1^2 - 1/n_2^2) \quad (1.1)$$

where  $R_H$  is the Rydberg's constant ( $R_H = 1.097 \times 10^7 \text{ m}^{-1}$ ). For  $n = 1$  (the Lyman series), a photon of light could excite the atomic Hydrogen if it has a wavelength shorter than the excitation wavelength (for  $n_2 = \infty$ ) given by the above equation. The first transition of the electron (with  $n_2 = 2$  and  $n_1 = 1$  in the above equation) requires a photon of wavelength 1216Å. The UV photons with the right wavelength shorter than 1216Å could excite the Hydrogen and any photon with a wavelength shorter than 912Å (the Lyman limit) could fully ionize the Hydrogen atom (with  $n_2 = \infty$  and  $n_1 = 1$  in the above equation). The IGM and ISM is filled with neutral Hydrogen (among other elements). The distribution of these regions could be clumpy or uniform with different column densities and they are at different distances in the IGM with respect to us. The UV photons generated by the most massive stars in galaxies pass through these regions before reaching us and would be absorbed and reemitted by this neutral gas several times. Figure 1.1 shows the mean cosmic transmission at  $z=3, 4$  and  $5$  as a function of observed wavelength (Madau et al., 1996) demonstrating the drop in the restframe UV flux of distant galaxies as it travels through the neutral Hydrogen in the IGM.

In his pioneering work Steidel et al., 1996 used this feature of the redshifted UV emission of star forming galaxies to develop a technique to identify the most distant objects in the Universe. This technique is based on the sudden change in the color of a galaxy in different broad-band filters as the pass-bands straddle the Lyman break feature. The galaxies identified using this technique are known as Lyman Break Galaxies (or LBGs). Figure 1.2 shows the color-color diagram for the LBG selection at  $z \sim 3$  from Steidel et al., 1999 using the U, G and R filters. The different lines correspond to the redshift dependent color evolutionary

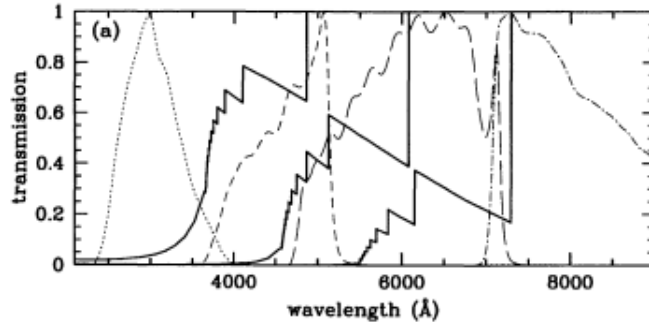


**Figure 1.1:** The mean cosmic transmission for a source at redshifts 3, 4 and 5 (solid lines from left to right) demonstrating the drop in the restframe UV flux as it travels through the neutral Hydrogen. The ACS filter throughputs are also plotted as dashed/dotted lines. The plot is adopted from Madau et al., 1996.

tracks of different extinction values for star forming galaxies. The U and G filters straddle the Lyman break and the sudden change in the color is mainly used to develop the criteria for identifying LBGs.

### 1.1.2 The Formation of the Red Sequence

Galaxy populations in the Universe are very diverse with varying properties and appearances. Although quite different, galaxies could still be classified according to several distinct properties. The most basic classification of galaxies is by looking at their basic properties (color, mass, etc) and morphologies. According to this classification, galaxies are grouped into late type star forming galaxies and early type quiescent systems. The late type galaxies are usually disk or irregular systems that are bluer and are relatively rich in gas with high star formation while the early type galaxies are redder and more massive gas deprived systems with featureless morphologies better known as elliptical galaxies. The bimodality in galaxy distribution is evident in the local Universe and is very well demonstrated on the color magnitude diagrams. Figure 1.3 shows the distribution of the local galaxies from the Sloan Digital Sky Survey on the color magnitude diagram. We clearly see the separation of the two populations of galaxies on this plot.

Several studies show that the number density of quiescent early type galaxies drop rapidly at higher redshifts (Ilbert et al., 2013). The high redshift star forming galaxies

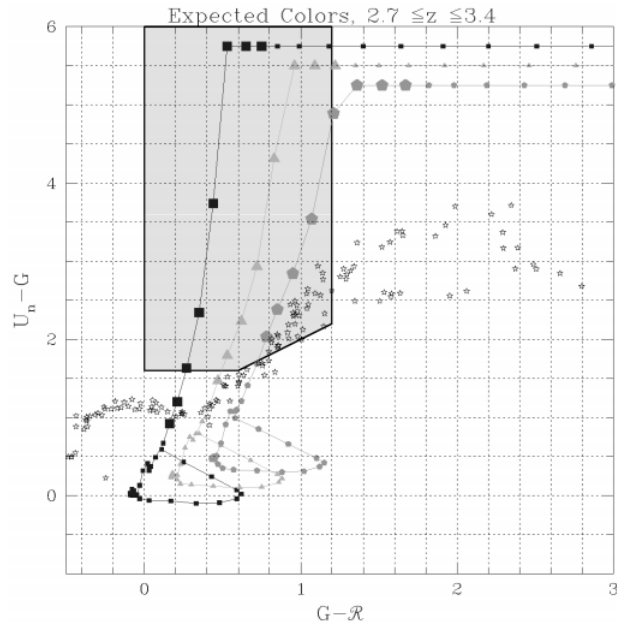


**Figure 1.2:** The Lyman Break Galaxy (LBG) selection criteria (also known as the UGR selection for the filters used) developed by Steidel et al., 1999 to identify star forming galaxies at  $z \sim 3$ . The three different redshift dependent color evolutionary tracks are drawn for star forming galaxies with three different values of extinction.

are usually identified by the LBG selection technique which is sensitive to UV bright star forming systems, as I discussed in the previous section. Recently, however, there have been several studies that indicate the presence of quiescent galaxies and provide evidence for the formation of the red sequence at redshifts as high as  $z \sim 2$  (Franx et al., 2003; Labbé et al., 2005; Williams et al., 2009). Figure 1.4 shows the color-color diagram with the distinct separation of the two populations of star forming and quiescent galaxies to  $z \sim 2.5$ . These quiescent systems are mostly made of redder and cooler stars and therefore are relatively faint in the restframe UV.

Because of this faintness and due to the lack of prominent emission features associated with the passive nature, spectroscopic confirmation of these systems is challenging. In a recent study Kriek et al., 2009 obtained ultra deep spectra of a compact quiescent galaxy at  $z \sim 2.2$  and confirmed its existence through optical absorption lines. Study of high redshift LBG selected star forming galaxies show that these systems have distinct spectroscopic features that are tightly correlated with the galaxy properties (Shapley et al., 2003). Using

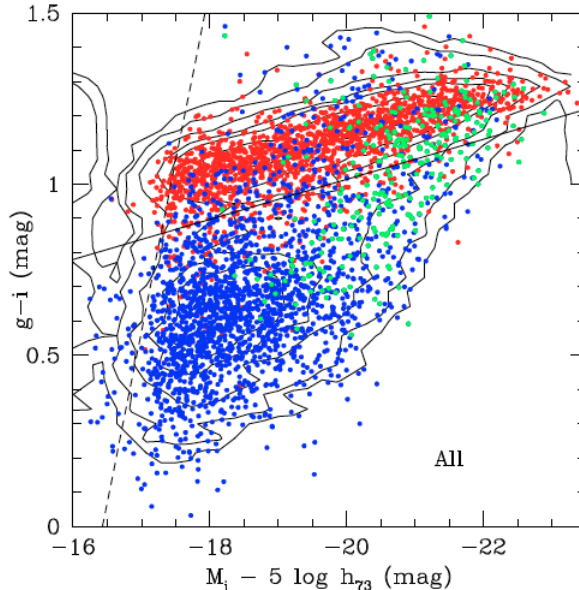


**Figure 1.3:** The color magnitude distribution of the local galaxies in the Sloan Digital Sky Survey (SDSS). The galaxies are color coded based on the spectral type with the red corresponding to early type, blue corresponding to late type and green corresponding to bulge galaxies (Sa-Sb). The contours are for equal densities and the solid line shows the empirical separation between the red sequence and the other galaxies. The plot is adopted from Gavazzi et al., 2010.

a large sample of spectroscopically confirmed LBGs at  $z \sim 3$  Shapley et al., 2003 showed that the Lyman- $\alpha$  equivalent width is tightly correlated with the low ionization absorption line and the continuum extinction. These results could be understood in terms of the distribution and kinematics of cold neutral gas in these systems. Studying the spectra of relatively quiescent galaxies at these high redshifts could reveal the nature of the interstellar medium in these newly quenched systems and give us further insight into the role of outflowing material in star formation suppression. Very deep spectroscopic observations of a large number of quiescent galaxies at high redshift is needed before we could reach any conclusion about the nature of these systems at high redshifts.

The confirmed quiescent massive galaxies at  $z \sim 2$  are shown to have very small sizes with most of the mass concentrated in a very small region of a few kpc in diameter (van Dokkum et al., 2008; Barro et al., 2013). These Compact Quiescent Galaxies (CQGs) or red nuggets are much smaller than their local early type counterparts of similar mass. There are several mechanisms proposed for the size growth of these high redshift compact galaxies

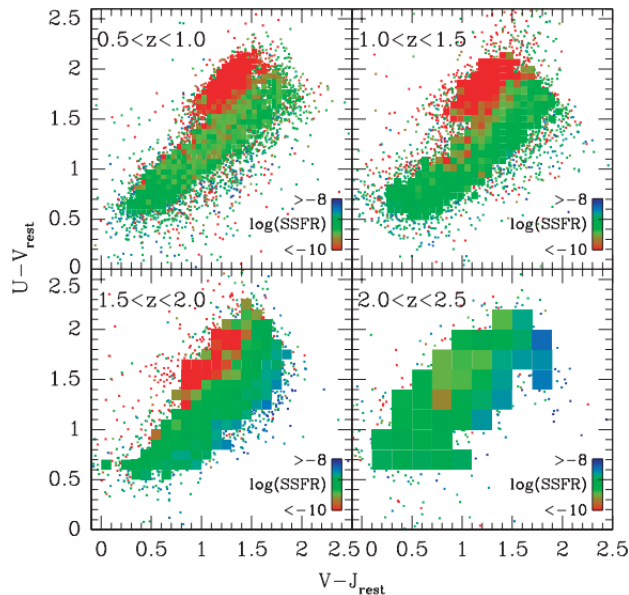


**Figure 1.4:** The (U-V) vs (V-J) color-color diagram (also known as the UVJ diagram) from Williams et al., 2009 used for separating the star forming and quiescent galaxies based on the  $4000\text{\AA}$ /Balmer break. The quiescent galaxies are shown in red as objects with very low Specific Star Formation Rates (star formation rate per unit mass).

at constant mass down to the local Universe with minor mergers playing an important role (Bezanson et al., 2009; Bell et al., 2012; Newman et al., 2012; Shankar et al., 2013; Hilz et al., 2013; Belli et al., 2014a). The formation of these compact systems is also poorly understood with recent studies indicating that they could be the progenitors of compact star forming galaxies quenching their star formation through outflowing gas (Barro et al., 2013; Williams et al., 2014a). Studying the size evolution of the most massive quiescent galaxies and the comparison with the star forming galaxies would help us understand the underlying physical principles responsible for this evolution.

## 1.2 Hierarchical Models of Galaxy Formation

The currently accepted theory for galaxy formation is the hierarchical model of Cold Dark Matter (CDM). According to the  $\Lambda$ -CDM scenario, galaxies assembled most of their mass through sequential merging, becoming more massive as they move down to lower redshifts

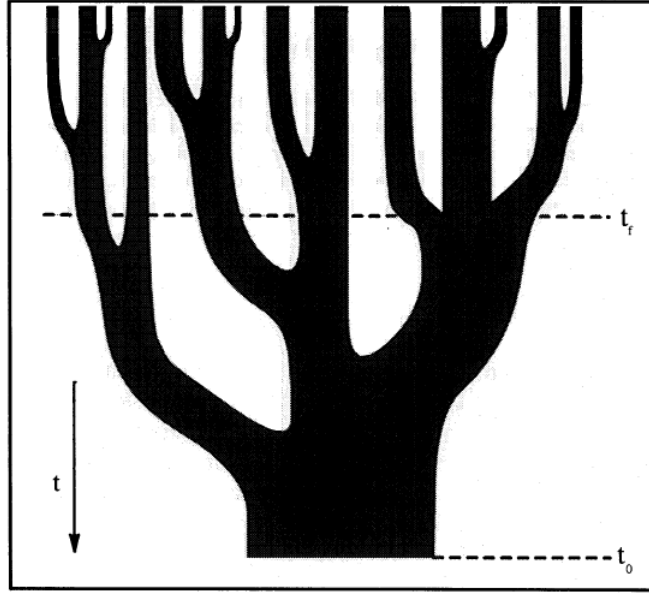


**Figure 1.5:** The galaxy merger tree as discussed in Lacey and Cole, 1993 showing the growth of the dark matter halos with time. Time is on the y-axis with the present time at the bottom of the plot. Each horizontal cut in the plot shows the distribution of the halos at a given time.

(Kauffmann et al., 1993; Reed et al., 2003). These hierarchical models predict that dark matter halos become ever more massive as we move to the more recent past, with the gravitational potential wells produced by these halos providing the required seeds for gas collapse, leading to formation of galaxies (Sheth et al., 2001; Navarro et al., 1996). As a result, more massive galaxies are expected to form in massive halos at lower redshifts with younger and less massive systems often located at a more distant past (i.e., higher redshifts). Figure 1.5 shows a schematic diagram of the mass assembly in this hierarchical model. According to this Figure, the most massive galaxies are expected to be found most abundantly in more recent times in the most massive halos that form from the merger of the smaller halos. I will discuss this further in the next section in the context of old and massive galaxies at high redshifts.

### 1.3 Massive and Old Galaxies at High Redshifts

The LBG selection of identifying high redshift galaxies is most sensitive to identifying galaxies with relatively bright UV continuum. The rest-frame UV light in these systems originate from massive O and B type stars in these galaxies that are produced by recent star formation. The relatively older systems lack the bright UV continuum characteristic of star forming galaxies and will be missed by LBG selections. Recent studies indicate the presence of a population of old and massive galaxies at redshifts as high as  $z \sim 2$  identified from very deep near infrared and infrared observations targeting the old population within these galaxies. The existence of such systems at high redshifts in large numbers could strongly constrain galaxy formation scenarios. As discussed in the previous section these old and massive galaxies are expected to live in the most massive Dark Matter Halos (DMHs) which are relatively scarce at high redshifts. Given the old ages and large stellar masses, most of these systems must have formed bulk of their mass at very high redshift in a burst of star formation with  $\text{SFR} \gtrsim 1000 M_{\odot} \text{Yr}^{-1}$ . The very highly star forming galaxies at high redshift identified in radio observations as sub-mm galaxies are proposed as possible progenitors for these old and massive systems although the exact mass assembly process is still poorly understood. Having a correct census of these massive galaxies could also help us better understand the contribution of the different populations of galaxies to the global stellar mass density and to study the high mass end of the stellar mass function.

In this study I plan to identify old and massive systems at  $z > 3$ . The main aim of this work would be to study the photometric and spectroscopic properties of this population and how these properties compare to that of the star forming galaxies. I will also aim to study the number density and mass density of these systems to understand the contribution to the global stellar mass density. Equally important is to study the effect of the presence of this population on CDM models of galaxy formation and to study the progenitors of these systems. In the following section I will outline the thesis plan used to address these statements.

## 1.4 Thesis Plan

In this work I will present a novel selection technique for identifying massive and evolved systems at  $z \gtrsim 3$  using very deep observations by the Hubble Space Telescope and Spitzer Space Telescope in the optical, near infrared and infrared bands. The selection criteria is developed to identify relatively quiescent systems at  $z \sim 3 - 4$  using the strength of the Balmer break (an age dependent diagnostic at restframe  $3648\text{\AA}$ ) in the spectra of post-starburst galaxies while avoiding contamination from lower redshift red dusty systems. We confirm several of the massive and old candidate systems with very deep observations with Keck/DEIMOS. I stack the obtained spectra of star forming and quiescent galaxies to compare the most important spectroscopic features of star forming and quiescent systems at  $z \sim 3 - 4$ . In particular I look at the Lyman- $\alpha$  resonance line, the SiIII and OI low ionization absorption features and the SiIV and CIV high ionization absorption features. The relative strength of these lines with respect to one another and to the physical properties of the galaxy give us insight into the cold neutral and hot ionized interstellar medium of star forming and quiescent galaxies at high redshifts and help us understand the role of this interstellar medium and kinematics associated with it in the quenching of star formation. Finally I use very deep near infrared observations by HST/WFC3 to measure the size of the quiescent galaxies at  $z \sim 3 - 4$  and compare this with the size of star forming galaxies at similar redshifts and explore the size evolution relation for star forming and quiescent galaxies.

In Chapter 2 I will present the data used in this study. I will discuss this in the context of a template fitting package used to extract the photometry. In Chapter 3 I will present the selection method that I developed to identify the old and massive systems at high redshifts ( $z \gtrsim 3$ ). The study of the size evolution and mass-size relation for quiescent galaxies at  $z \sim 3 - 4$  is presented in Chapter 4. I will discuss the Keck spectroscopic results of relatively quiescent systems in Chapter 5. Throughout this work I assume a standard cosmology with  $H_0 = 70 \text{ kms}^{-1}\text{Mpc}^{-1}$ ,  $\Omega_m = 0.3$  and  $\Omega_\Lambda = 0.7$ .

## Chapter 2

# Photometric Data

### 2.1 Introduction

One of the major goals of modern observational cosmology is to study the formation and evolution of galaxies with cosmic time. The HST high resolution observations with its wide wavelength coverage, made it possible to acquire the deepest images of the sky in multiple bands. In particular the installation of the Wide Field Camera 3 (WFC3) on board HST with the UltraViolet and Near Infrared filters set a totally new stage for studying galaxy evolution in many different frontiers.

There exist a very wide range of galaxy populations at different look back times ranging from the very blue star forming populations to the very red dusty or very old systems. Understanding the evolution of these population relies on the availability of multi wavelength photometric data from the bluest bands to the reddest possible. In this work I will present a multiwavelength catalog of galaxies that combine the best and deepest observations by the HST with the deep ground-based observations and Spitzer Space Telescope data and generate consistent photometry for all these observations. This brings a unique opportunity to study the galaxy evolution and compare the properties of different populations of galaxies at the HST depth and resolution.

In this work I will take advantage of the very deep HST observations by the Cosmic

Assembly Near-infrared Deep Extragalactic Legacy Survey (CANDELS; PI. S. Faber and H. Ferguson; see Grogin et al., 2011. CANDELS Koekemoer et al., 2011) is the largest project ever approved on the HST (with more than 900 orbits) and it is designed to use the deep observations by the HST/WFC3 and Advanced Camera for Survey (ACS) instruments to study the galaxy formation and evolution throughout cosmic time in different fields. The CANDELS images are publicly available after acquisition. One of the fields that has been targeted by CANDELS is the Great Observatories Origins Deep Survey (GOODS; Giavalisco et al., 2004b) southern field. The GOODS-S field (centered at  $\alpha(J2000) = 03^h32^m30^s$  and  $\delta = -27^\circ48'20''$ ) has been studied extensively by many ground-based and space observatories over the past few years and in particular more recently with the HST/WFC3 by the CANDELS.

In this work I will present the multi-wavelength photometric catalog for the GOODS-S field. This catalog is generated from the deepest optical data by the HST/ACS and base the selection on the combined blue to red optical bands. This brings a unique opportunity to study different populations of galaxies using the same photometric catalog in an unbiased way by providing a complete census of the different type of galaxies. The photometric catalog is simultaneously sensitive to blue star forming and red dusty or old systems and further complements other photometric catalog in the field by CANDELS team selecting galaxies in the near infrared.

In Section 2.2 I will present the photometric data used in this study. I will discuss our method for estimating the photometry on the ground based, HST and Spitzer data in Section 2.3 and perform the data quality checks on the estimated photometries in Section 2.4.

## 2.2 Data

The GOODS-S field Giavalisco et al., 2004b has been observed in many different wavelengths from the X-ray to the far infrared. These are observations by the Very Large Telescope

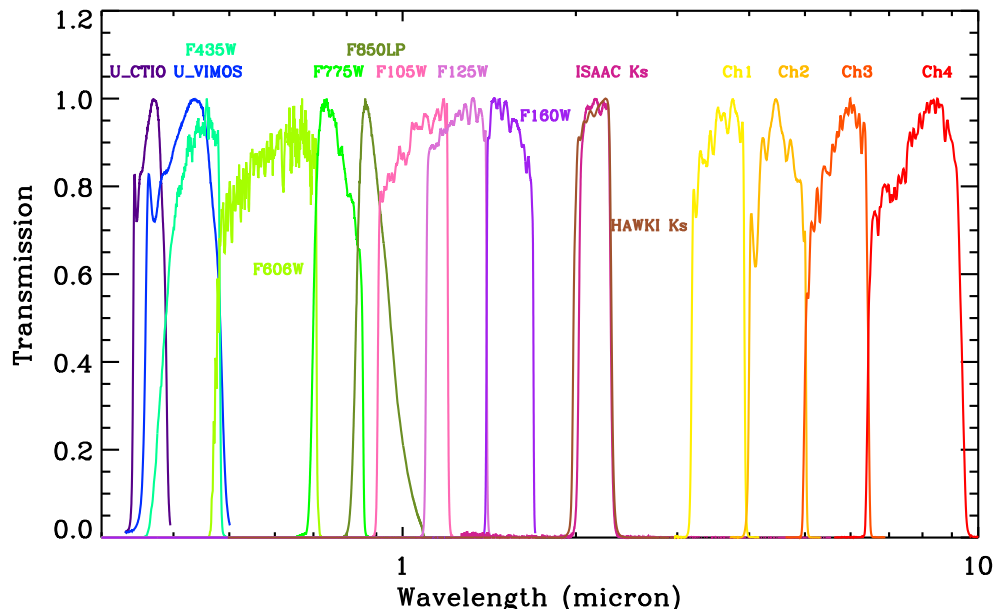


**Figure 2.1:** The transmission curves of the optical, near infrared and infrared filters in the CANDELS GOODS-S.

(VLT) in the U and in the near infrared and by the Spitzer in the four IRAC bands. As part of the CANDELS program the field was reobserved using the Hubble Space Telescope in both the optical and the near infrared. Figure 2.1 shows the transmission curves for all the broad band optical, near infrared and infrared data in the GOODS-S CANDELS catalog. In this section I will discuss the data used in this study.

### 2.2.1 HST Observations

The GOODS-S is observed by the HST/ACS instrument in the F435W, F606W, F814W and F850LP filters ( $B_{435}$ ,  $V_{606}$ ,  $i_{814}$  and  $z_{850}$ ) with angular resolution of 0.125 arcsec. These observations in the GOODS-S are centered around the Chandra Deep Field South (CDFS) and cover an area of approximately  $10' \times 16'$ . The GOODS-S field has been re-observed by the ACS in the  $B_{435}$ ,  $V_{606}$ ,  $i_{775}$  and  $z_{850}$ ) as part of the CANDELS which ultimately provided an unprecedented depth in the optical bands in the field.

The GOODS-S field is recently observed by the new WFC3near infrared instrument

in the F098M, F105W, F125W and the F160W ( $Y_{098}$ ,  $Y_{105}$ ,  $J_{125}$  and  $H_{160}$ ) as part of the CANDELS. The CANDELS WFC3 observations are in the wide and deep section with areas of  $\sim 9'.9 \times 14'.9$  and  $\sim 6'.8 \times 10'.0$  respectively. The main difference between the two sections is the depth of the observations. The deep section has been observed on average over 13 orbits while the wide section is observed with the HST over 3 orbits. The CANDELS GOODS-S deep area consists of a rectangular grid of  $3 \times 5$  WFC3/IR tiles that are oriented at a position angle of  $70^\circ$  (Grogin et al., 2011). Figure 2.2 shows the CANDELS HST/WFC3 survey outline in the GOODS-S. The observation depth, effective wavelength and the PSF information for each of the filters are summarized in Table 2.1.

## 2.2.2 Ground-based Observations

The ground based data in the multiwavelength catalog is from several observatories. The GOODS-S field is targeted by the VLT/VIMOS in the U-band. The VIMOS U-band is significantly deeper than the previous observations by the CTIO (Nonino et al., 2009). The ground-based near infrared observations in the GOODS-S field is by the VLT/ISAAC in the J, H and Ks bands. Figure 2.3 shows the sky coverage of the different ground based and space data in the GOODS-S CANDELS.

## 2.2.3 Spitzer InfraRed Observations

The GOODS-S field is observed by the Spitzer Space Telescope IRAC instrument (Fazio et al., 2004) in the main four channels with effective wavelengths of  $3.6 \mu m$ ,  $4.5 \mu m$ ,  $5.8 \mu m$ ,  $8.0 \mu m$ . The observations in the  $3.6 \mu m$ ,  $4.5 \mu m$  bands are complemented by deeper observations from the Spitzer warm mission (Ashby et al., 2013). These observations are more than a magnitude deeper than the original GOODS IRAC observations (Dickinson et al., 2004).

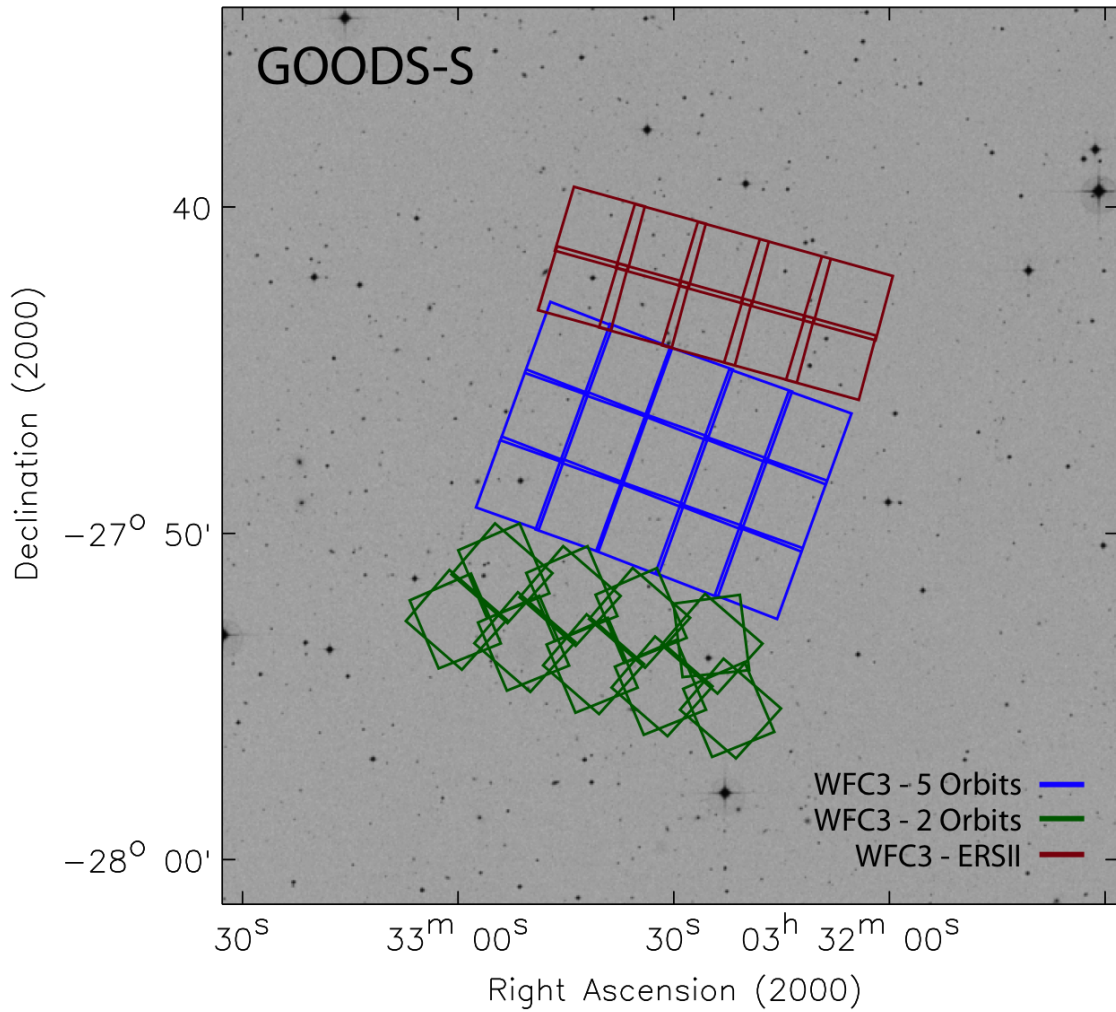


**Figure 2.2:** The outline of the CANDELS GOODS-S HST/WFC3 observations (Grogin et al., 2011). The CANDELS Early Release Science is shown in red while the Deep and Wide areas are shown in blue and green respectively.

**Table 2.1:** Summary of the GOODS-S CANDELS Broad-Band Data.

Instrument	Filter	Effective Wavelength (Å)	PSF FWHM (arcsec)	5 $\sigma$ limiting depth ( $r_{ap} = 1\text{FWHM}$ ) (AB magnitude)
VLT/VIMOS	<i>U</i>	3722	0.80	27.97
HST/ACS	<i>F435W</i>	4317	0.08	28.95
	<i>F606W</i>	5918	0.08	29.35
	<i>F775W</i>	7693	0.08	28.55
	<i>F850LP</i>	9055	0.09	28.55
HST/WFC3	<i>F105W</i>	10550	0.15	28.45
	<i>F125W</i>	12486	0.16	28.34
	<i>F160W</i>	15370	0.17	28.16
	<i>Ks</i>	21605	0.48	25.09
VLT/ISAAC Spitzer/IRAC	3.6 $\mu m$	35508	1.66	26.52
	4.5 $\mu m$	44960	1.72	26.25
	5.8 $\mu m$	57245	1.88	23.75
	8.0 $\mu m$	78840	1.98	23.72

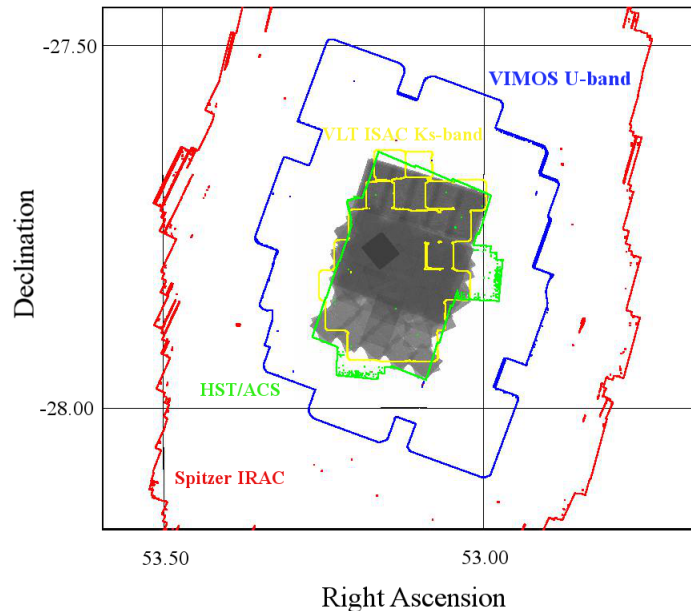


**Figure 2.3:** The sky coverage of the survey in the GOODS-S field. The gray shaded area shows the exposure map of observations in the WFC3 F160W band. The IRAC coverage is from deep observations of the GOODS-S by the SEDS program (Spitzer warm mission; Ashby et al., 2013).

## 2.3 Photometry

In generating the multiwavelength catalog, the high resolution data (HST/ACS and WFC3) is treated differently from the low resolution data (ground-based and Spitzer IRAC). In this section I will discuss the photometric extraction for our full data set in the GOODS-S CANDELS field.

### 2.3.1 HST Photometry

I performed photometry on the high resolution (ACS + WFC3) data using SExtractor (Bertin and Arnouts, 1996). I use a modified SExtractor which is changed in several ways (Galamez et al., 2013): I. The inner annulus adopted by the code and used for the local sky background determination is at least  $1''$  II. A modified cleaning procedure that ensures that the non-detections sources are not merged with the real sources when the code is merging all the split sources in the end. III. There are also several minor modifications such that

for example in dual mode the code uses the gain of the measurement image (and not the detection) to calculate isophotal corrected magnitudes.

Galaxies exist in varying forms in the Universe with different masses, star formation rates and histories, interstellar gas and dust and ages. Because of these distinct properties, galaxies would be observed differently in different filters and would have colors characteristic of their underlying stellar population. Dust free star forming galaxies would generally look blue and the older more passively evolving systems would look redder. Any selection of galaxies based on a single passband would be biased against a given population depending on the selected band with bluer bands being biased against red dusty star forming local or high redshift galaxies and red quiescent systems and a redder bands being biased against the very blue star forming systems. In order to address this issue I generated a stacked optical detection bands from the four high resolution HST/ACS observations in the  $B_{435}$ ,  $V_{606}$ ,  $i_{775}$  and  $z_{850}$ . The stacked image is generated by combining the optical images using an inverse variance weighting with the help of the rms maps. The stacked rms map is also generated from the combination of the individual rms maps using the square root of the sum of the quadratures of the maps. This image is then used as the detection image in the SExtractor in dual mode where the photometry is done on all the other bands.

### **2.3.2 The hot + cold mode**

Given the diverse nature of galaxies with different surface brightnesses and sizes, it is difficult, if not impossible, to identify all populations of galaxies using only a single given set of parameters (signifying the area, signal to noise, background, etc) for the extraction (Galametz et al., 2013; Guo et al., 2013). In order to address this I used one set of parameters to address bright source detection and focus on deblending extended sources and a second set of parameters to address the detection of the most distant and faint galaxies at high redshift. This method is also know as the hot+cold mode for source selection (Rix et al., 2004; Galametz et al., 2013; Guo et al., 2013). Basically the cold mode SExtractor parameters are optimized to detect the brighter more extended sources while the hot mode

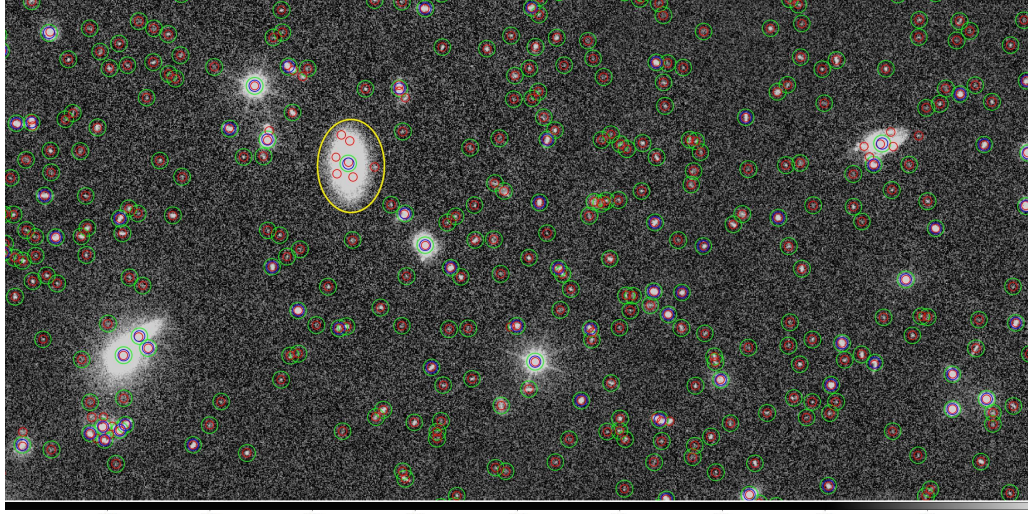


**Figure 2.4:** The hot and cold mode detected sources in the GOODS-S. The cold mode selected sources are shown blue. These are relatively local high surface brightness extended sources. The hot mode selected source sources are shown in red. These are small low surface brightness objects that are identified by setting low detection thresholds and areas in the SExtractor input parameters. The final sources in the catalog are shown with green circles in the figure. These are identified from the combination of hot and cold mode selected sources using the routine developed for GALAPAGOS. The yellow region shows an area were multiple hot detected sources would only lead to one detected source in the final catalog according to the combination routine.

parameters are optimized to identify sources with faintest surface brightnesses. This is done by choosing different values for the analysis threshold and area and the convolution filter in the SExtractor paramters (Galamez et al., 2013). The two given catalogs generated by the hot and cold SExtractor parameters are then combined using the routine developed for the GALAPAGOS Barden et al., 2012. According to this all the cold mode selected sources are added to the catalog. The code then checks for the hot mode selected sources. If a hot source falls within a kron ellipse of a cold source it would be discarded, otherwise it would be added to the final catalog according to this algorithm. This would then make the final high resolution detection catalog which has the photometry in the HST/ACS  $B_{435}$ ,  $V_{606}$ ,  $i_{775}$  and  $z_{850}$  and HST/WFC3  $Y_{098}$ ,  $Y_{105}$ ,  $J_{125}$  and  $H_{160}$  bands. Figure 2.4 shows the hot and cold selected sources along with the sources in the combined catalog.

### 2.3.3 Low Resolution Photometry

All the non-HST bands in our catalog are the low resolution data for photometry extraction. This includes all the ground-based data discussed above and the Spitzer infrared data in the four IRAC bands. In order to measure the photometry in these bands I use the Template FITting method (TFIT; Laidler et al., 2007).

TFIT is a robust algorithm for measuring photometry in mixed resolution data sets. Sources that are often well separated in the high resolution image (HST) could be blended in the low resolution image (ground-based or Spitzer). TFIT uses prior information (position and light profiles) from the high resolution image to calculate templates that are used to measure the photometry in the low resolution image. TFIT does that by smoothing the high resolution image by the PSF of the low resolution image using a convolution kernel (Galamez et al., 2013). Fluxes in the low resolution image are then measured using these templates while fitting the sources simultaneously.

In order to successfully run TFIT we need to perform preparation routines on the low resolution images that I outline below:

I. The low resolution image has to be background subtracted. I use the routine developed by the CANDELS team to estimate the background for each low resolution image using source masked images as described in Galamez et al., 2013. Basically the routine first determines a rough background approximation by smoothing the image on large scale using a large annulus ring-median filter. The image is then smoothed to the image PSF scale and sources are masked (Galamez et al., 2013).

II. The low resolution image pixel scale has to be an integer multiple of the high resolution image. The ACS stacked images have pixel scales of  $0.06''$ . I used Swarp (Bertin, 2010) to change the pixel scale of the low resolution image to match the high resolution image. To do this we need the astrometry information for both the high resolution and low resolution images and the scale factor for which we need to use to transform one image to the other as outlined in the Swarp manual.

In addition to this we need to generate a Point Spread Function (PSF) for the low and

high resolution images. The PSF is made using unsaturated isolated stars in the field. The light profile of these well behaved stars are stacked to produce the PSF for the high-res and low-res passbands. I use this PSF information for the high-res and low-res images to find a convolution kernel that would transform one to the other as outlined in Galametz et al., 2013.

We run TFIT with parameter file that lists the following input files: I. the high resolution image II. the low resolution image (with the correct pixel scale and rotation as outlined above) III. the high resolution image PSF IV. the low resolution image PSF V. the segmentation map from the SExtractor VI. the high resolution source catalog (from the SExtractor) VII. the low resolution image rms map.

TFIT then runs the several steps outlined in Laidler et al., 2007 to estimate the flux in the low resolution image while simultaneously fitting for these objects. In addition to the output photometry catalog, TFIT produces residual collage images made from subtracting the model templates from the low resolution image as a visual indicator for the goodness of fit. Figure 2.5 shows sample residual maps in the optical, near-infrared and infrared bands after running TFIT with the ACS stacked image taken as the detection band. Table 2.1 summarizes the PSF information used for the high and low resolution images.

## 2.4 Data Quality Checks

I check the TFIT measured photometry and colors by comparing it with other independently measured photometry in the field and also perform self consistency checks within the catalog. In this section I discuss the validations checks performed on the catalog.

### 2.4.1 Color Validation Check

In order to check the robustness of the measured colors, I looked at the distribution of the sources on color-color diagrams. One such well calibrated diagram is the BzK color plot that can be used to separate star forming, quiescent galaxies and stars (Daddi et al., 2004).

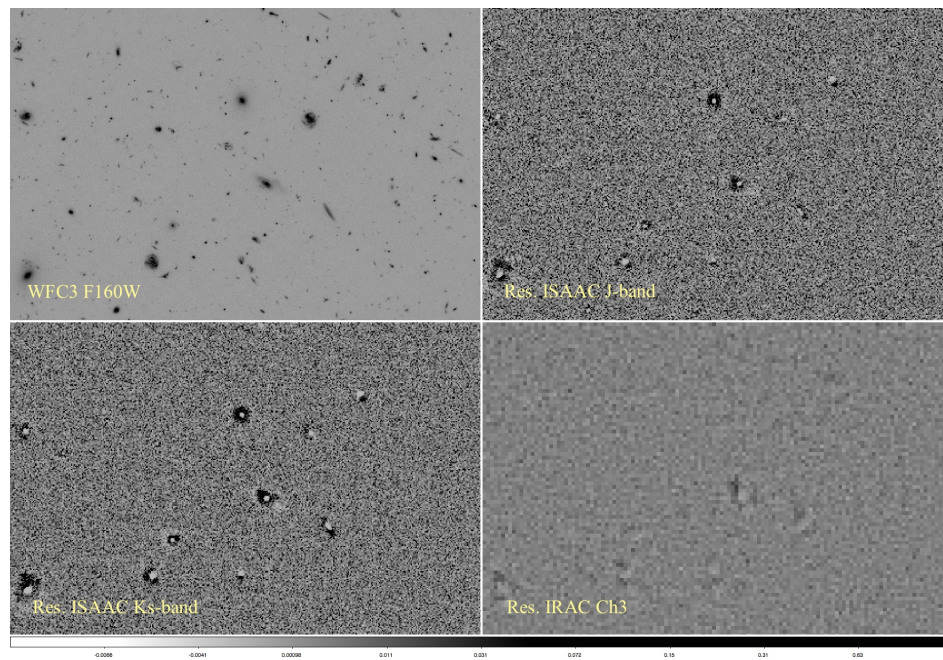


**Figure 2.5:** The stacked ACS selection image (top left) along with sample TFIT residual maps in the VLT/ISAAC J and Ks and the Spitzer IRAC infrared. Sources that are well separated in the high resolution ACS image could well be blended in the lower resolution images. The residuals left in the images are mostly for objects with very centrally concentrated light for which the PSF used is under-subtracting the core (white region at the center) and over-subtracting the wings (dark regions at the wings).

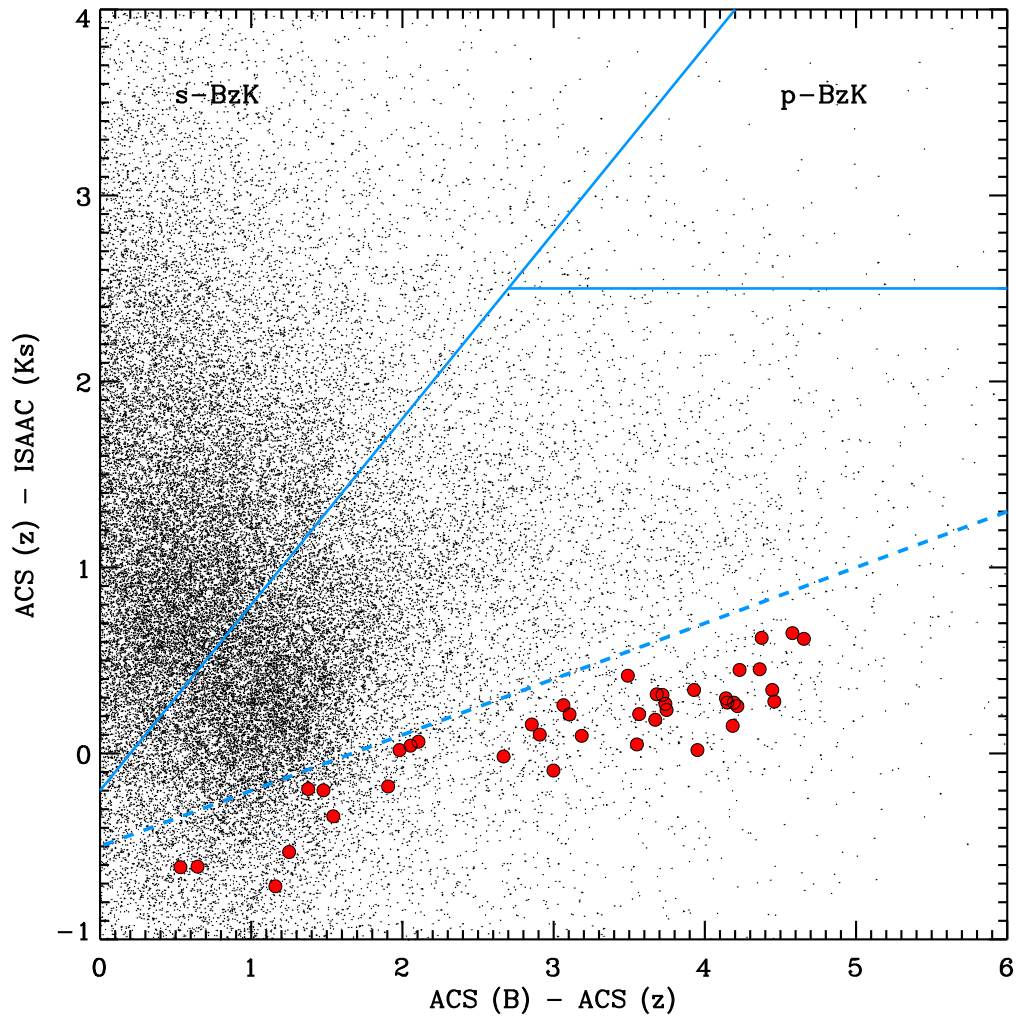


**Figure 2.6:** BzK color-color plots (Daddi et al., 2004) and the extensions of the color selection to higher redshifts (the so-called VJL and iHM selection; Guo et al., 2012) showing the distribution of the star-forming and passive galaxies. The dashed line shows the expected position of stars on the color-color plot. The stars in the field are shown with red circles on the plot.

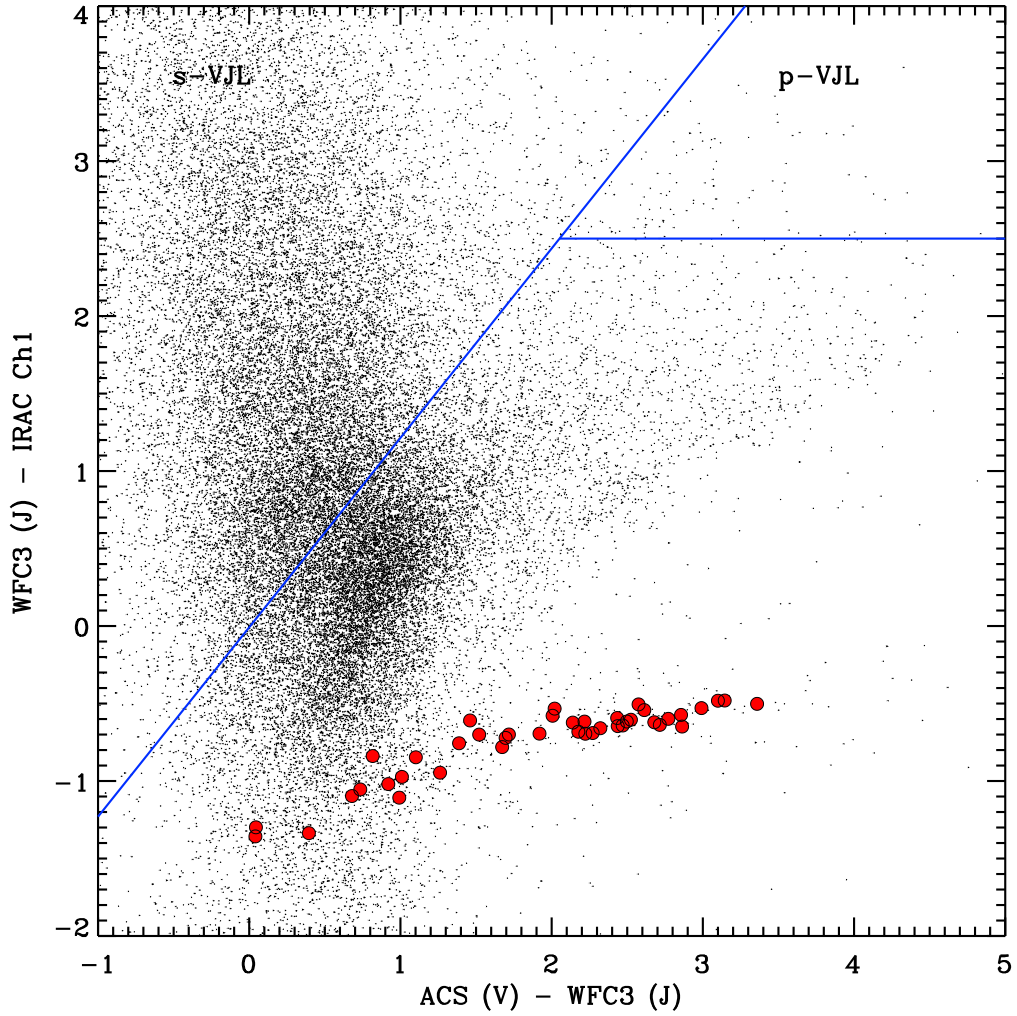


**Figure 2.7:** The (J-Ch1) vs (V-J) color-color plot (VJL) developed by Guo et al., 2012 used to separate the star forming and passive population at  $z \sim 3$ . The red circles are the observed color of the stars which agrees with the locus predicted by Guo et al., 2012 for point source objects.

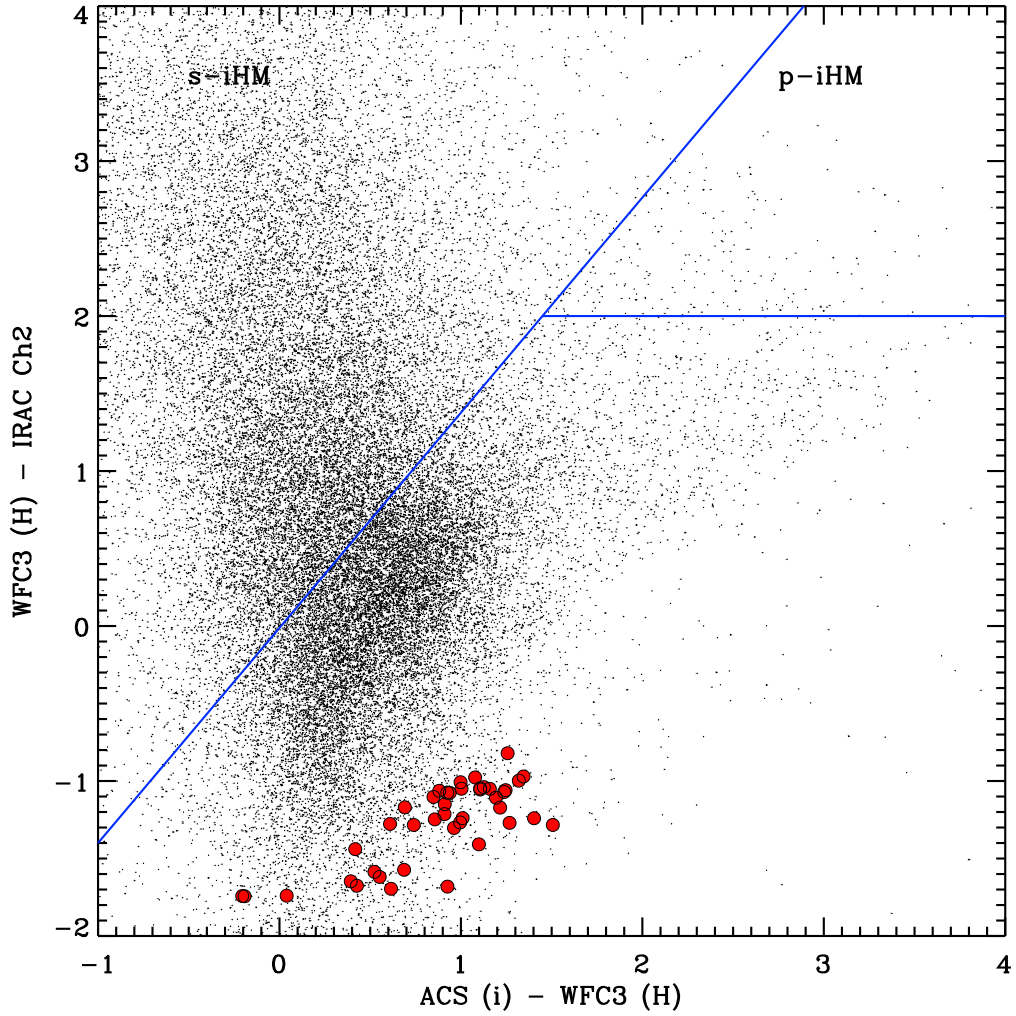


**Figure 2.8:** The (H-Ch2) vs (i-H) color-color plot (iHM) used at  $z \sim 4$  with the red circles showing the our measured colors of the stars in the field. This agrees with the predictions by Guo et al., 2012 for the stellar locus.

Figure 2.6 shows the BzK color-color plot along with the higher redshift iHM and VJL plots in Figures 2.7 and 2.8. The iHM and VJL color plots are the extension of the BzK method to redshifts  $z \sim 3-4$  using different sets of filters for separating the star forming and passive galaxies as discussed in Guo et al., 2012. The dashed line in the BzK plot shows the stellar locus on the diagram as predicted by Daddi et al., 2004. We see that the distribution of the color of stars on the diagram is relatively consistent with the predicted locus.

In order to check the robustness of the estimated photometry I checked the color of the stellar sources in the catalog and compared it with the color trends of library of stellar models. For the model stars I used the BaSeL library (Westera et al., 2002). I convolved the SEDs in the stellar library with the filter throughputs in the field and computed the colors for the stellar models. Figure 2.9 shows the color-color diagrams of the stars in the GOODS-S field along with the stellar models from the BaSeL library. We see from the Figure that our measured colors of stars in the field is consistent with the colors of model stars from the library.

#### 2.4.2 Photometry Validation Check

In this section I check the robustness of the estimated photometry of the sources in our stacked ACS selected TFIT catalog with the public photometry available in the GOODS-S. In order to check the photometry I use the  $H_{160}$  band selected photometric catalog generated by the CANDELS team in the GOODS-S (Guo et al., 2013).

Figure 2.10 shows the photometry comparison of the TFIT catalog with the photometry in the GOODS-S fields. For the source matching I used a radius of  $\sim 1''$  between the TFIT catalog and the comparison catalog. In Figure 2.10 we are showing the distribution of our sources in the catalog with difference shown on the y-axis and the WFC3 F160W magnitude on the x-axis and with the stellar sources shown as red circles. We see from the comparison plots that our measured photometry is consistent with the public photometry in the field. The ISAAC Ks band shows an offset of  $\sim 0.08$  between our photometry and the CANDELS. This shift could be interpreted as a zero point offset between the two photometries due to

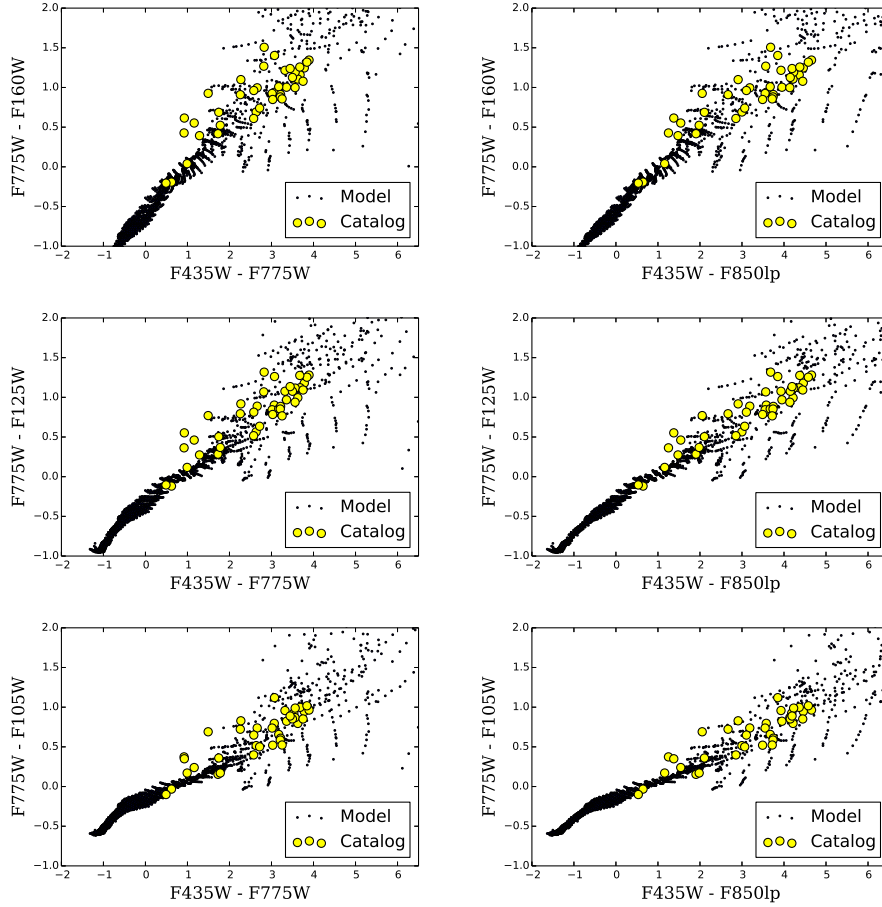


**Figure 2.9:** The color-color diagrams showing the color of stars in the GOODS-S field (yellow). The color of observed stars is consistent with the color of model stars from the BaSeL library (shown in black).

the consistent shift above the y-axis which seems to be independent of the magnitude of the source.

## 2.5 Conclusion and Summary

In this Chapter I presented the photometric catalog of galaxies in the GOODS-S generated from very deep stacked HST/ACS images. Selecting galaxies simultaneously in the blue and red bands (by the stacked image) allows us to look at the different populations of galaxies (star forming and quiescent) using the same photometric catalog that is not biased towards a given population.

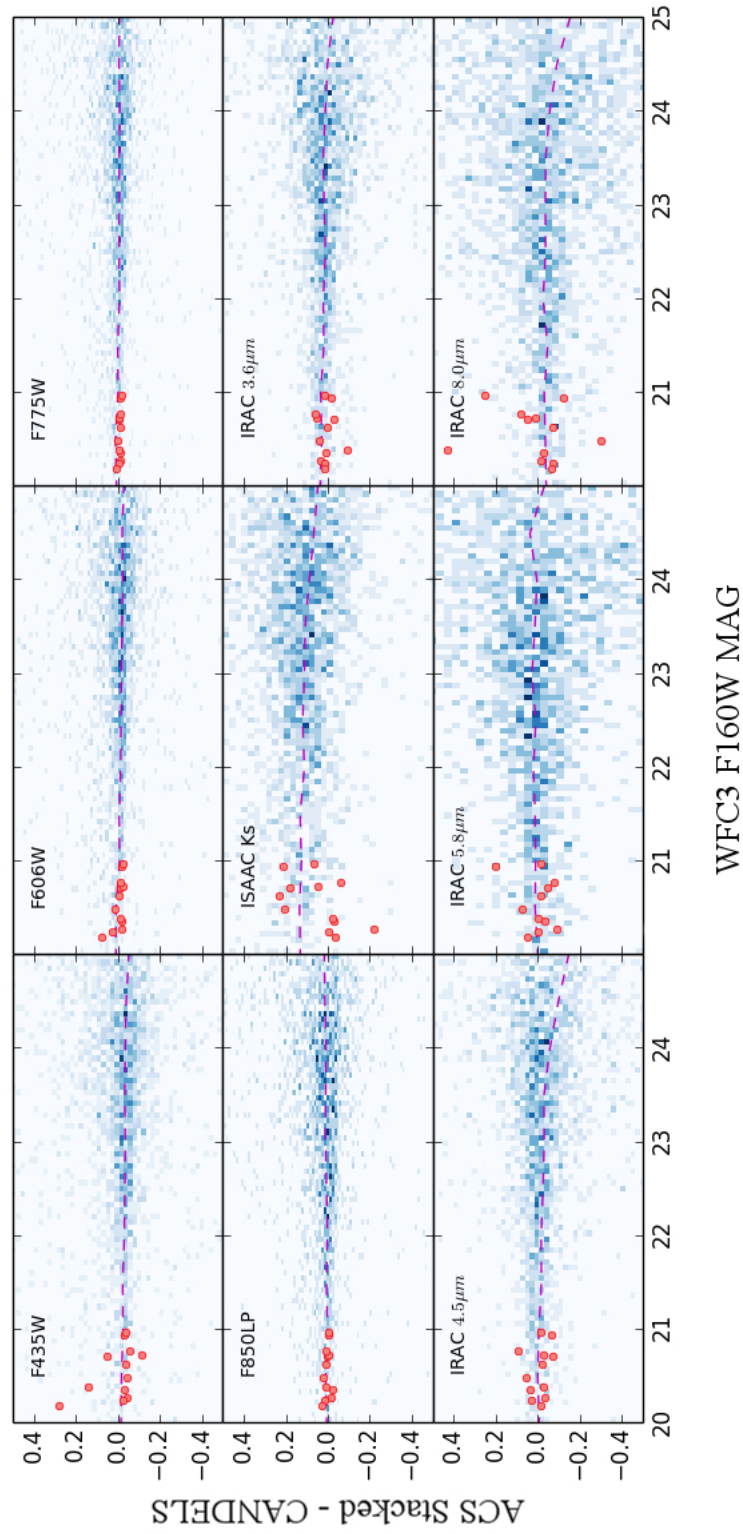


**Figure 2.10:** ACS Stacked photometry comparison with the CANDELS H-band selected catalog. The dashed magenta line shows the median difference between our magnitudes and that of the H-band selected catalog in bins of 0.25 magnitudes. The red points show the stellar locus on the diagrams.

I used TFIT to extract the ground-based and Spitzer photometry. TFIT is shown to be a very robust tool in measuring photometry for low resolution data in mixed resolution data-sets and in particular when source confusion becomes a problem. The photometric data that I measured using SExtractor and TFIT (for the high and low resolution data) is in very good agreement with previous measurements in the field.

This optically selected catalog is complementary to the near infrared selected catalogs in the field and in particular to the WFC3 H-band selected catalog of galaxies in the GOODS-S by the CANDELS team which is generated using similar algorithms and tools. The near infrared selected catalogs are more sensitive to the redder objects while biased against blue star forming galaxies. These catalogs generally pick more massive or more dust obscured systems at different redshifts. As a result of this it is important to have both catalogs for a comprehensive analysis of galaxy populations of different types across a large redshift.

## Chapter 3

# A Study of Massive and Evolved Galaxies at High Redshift

### 3.1 Introduction

One of the most important questions in modern astronomy is understanding galaxy formation and evolution. The general perception is that the youngest and bluest of galaxies are expected to be most abundantly found in the gas rich environments when the Universe was relatively young. At this very young Universe the dark matter halos hosting these galaxies are much smaller with weaker potential wells. According to this theoretical picture, the most massive dead galaxies are expected to be located in the more recent past. However, recent studies have indicated a new population of massive galaxies at redshifts as high as  $z \sim 5$  when the Universe was  $\sim 1$  Gyr old (Mobasher et al., 2005; Wiklind et al., 2008; Caputi et al., 2012). Furthermore, some of these galaxies show evidence for an evolved stellar population, formed through an initial burst of star formation followed by passive evolution (Labbé et al., 2005; Mancini et al., 2009; Fontana et al., 2009; Guo et al., 2012; Stefanon et al., 2013; Straatman et al., 2014; Oesch et al., 2013; Huang et al., 2011). This implies that most of these objects formed the bulk of their mass at very high redshifts.

A widely used method for selecting high redshift ( $z > 3$ ) galaxies is based on the iden-

tification of Lyman break feature, the so-called dropout technique (Steidel et al., 1996; Giavalisco et al., 2004a; Bouwens et al., 2007; Beckwith et al., 2006). Many of the evolved systems at high redshifts lack the strong UV continuum characteristic of star forming galaxies and therefore will be missed by such surveys. These evolved systems could strongly constrain galaxy formation scenarios and may constitute a significant fraction of the mass density of galaxies (Ilbert et al., 2013). Studying the contribution of this population to the global number and mass density will strongly constrain the high-mass end of the galaxy mass function at high redshifts. If such evolved and massive systems, missed from high redshift Lyman break selected surveys, exist in large numbers, they could put strong constraints on evolutionary scenarios and predictions from hierarchical models for galaxy formation.

I propose to identify these evolved systems by searching for the pronounced Balmer break feature at rest-frame  $3648\text{\AA}$  which is an age dependent diagnostic of their stellar population (hence the name Balmer Break Galaxies; BBGs). The Balmer break is most prominent in A-type stars with surface temperatures  $\sim 10^4\text{K}$ . The strength of the Balmer break feature does not monotonically increase with age and it reaches a maximum in stellar populations with ages 0.3 to 1 Gyr. Therefore it is an efficient tool for identifying relatively quiescent (quenching) systems with current star formation rates significantly lower than the past average (Kriek et al., 2008) .

In this work, I use the new Hubble Space Telescope/Wide Field Camera 3 (WFC3) near infrared data from observations taken as a part of the Cosmic Assembly Near-infrared Deep Extragalactic Legacy Survey <sup>1</sup> (CANDELS: PI. S. Faber and H. Ferguson; see Grogin et al., 2011 and Koekemoer et al., 2011) program to identify redshifted Balmer break features at  $3.0 < z < 4.5$ . In this redshift range the Balmer break falls between the H and K-band filters. Here I also take advantage of the very deep  $K_s$ -band observations (at  $\sim 2.2\ \mu\text{m}$ ) redward of the Balmer break from the VLT/HAWK-I instrument in the GOODS-S (Fontana et al. in prep.). The very deep near-IR photometry (from WFC3 and HAWK-I) ensures an accurate measurement of the Balmer break amplitude. Also the HST/WFC3 and optical

---

<sup>1</sup><http://candels.ucolick.org>

data (blue-ward of the break) help to break the degeneracy and avoid contamination by lower redshift dusty galaxies. This redshift range was chosen to take full advantage of the available deep WFC3 data when selecting the BBG candidates. This also reduces the lower redshift red color contaminants in the sample. Finally, since the objects are brighter at these lower redshifts, it provides a higher likelihood of successful spectroscopic observation compared to higher redshift (fainter) candidates (Wiklind et al., 2008).

The search for massive galaxies at high redshift is greatly aided by the availability of deep infrared data from the Spitzer Space Telescope. Massive galaxies are brightest in their rest-frame near-IR, which is shifted to mid-infrared Spitzer bands at higher redshifts. In this respect, Spitzer IRAC (Fazio et al., 2004) data provides an excellent probe of the stellar mass of galaxies at high redshifts (Papovich et al., 2006). Here I use Spitzer images, specifically the very deep IRAC observations at  $3.6\mu\text{m}$  and  $4.5\mu\text{m}$ , which are essential for estimating the stellar mass of these candidates.

This Chapter is organized as follows. In Section 2 I discuss the photometric data used for this study. In Section 3, I develop the criteria used to select the BBG candidates and discuss the robustness of the selection criteria. Section 4 presents the SED fitting of the candidate BBGs identified from the color-color plots and discuss the candidate properties. In Section 5 I discuss the MIPS detected BBG sample. I compare properties of the galaxies selected through the LBG and BBG techniques over the same redshift range in section 6 and I discuss the results in Section 7.

## 3.2 The Photometric Data

I use the multi-waveband deep photometric observations in the GOODS-S field (Giavalisco et al., 2004b). In this study I focus on the CANDELS GOODS-S Deep area, which has very deep observations by VLT HAWK-I instrument (Fontana et al. in prep.). The WFC3/IR observations in the CANDELS GOODS-S deep area consist of a rectangular grid of  $3 \times 5$  tiles ( $\sim 6.8' \times 10'$ ; Grogin et al., 2011) and photometric observations in more than fourteen

broadband filters. In the redshift range of interest here, I explore a volume of  $\sim 2.05 \times 10^5 \text{ Mpc}^3$ .

The GOODS-S has also been observed in the near-IR by the VLT HAWK-I in the  $K_s$  filter at effective wavelength  $2.2 \mu\text{m}$  (Fontana et al. in prep.). The HAWK-I  $K_s$  magnitude limit is 26.45 over an aperture radius of 0.4 arcseconds (Guo et al., 2013). This is more than a magnitude deeper than the previous VLT/ISAAC  $K_s$  data. The final field of view of this work is chosen to take advantage of the deep  $K_s$  band observations by the VLT/HAWK-I. The depth variation of the HAWK-I observations across GOODS-S does not play a significant role in selecting our candidates because of the small variations in the sky standard deviation at the position of our sources.

I use the WFC3  $H$ -band selected catalog for GOODS-S field which is generated using the Template-FITting (TFIT) algorithm (Guo et al., 2013; Laidler et al., 2007). TFIT is a robust method for combining multi wave-band data observed with different instruments. One of the complications of performing consistent multi-waveband photometry of objects is the difference in resolution and PSFs among different instruments. Objects that are well separated in high resolution images (ACS/WFC3) could be blended in the lower resolution data (ground based or IRAC).

TFIT uses prior information from high resolution images to construct object templates that are then fitted to the lower resolution image from which fluxes are extracted (Laidler et al., 2007). Here I used the  $H$ -band selected catalog because in the redshift range of interest here, the WFC3  $H_{160}$  falls blue-ward of the Balmer break feature and hence, we need detections in this filter to be able to identify the BBGs. The final photometric catalog has data in more than 12 bands including VLT/VIMOS U, HST/ACS  $B_{435}$ ,  $V_{606}$ ,  $i_{775}$  and  $z_{850}$ , HST/WFC3  $Y_{105}$ ,  $J_{125}$  and  $H_{160}$ , VLT/ISAAC and HAWK-I  $K_s$  and Spitzer/IRAC 3.6  $\mu\text{m}$ , 4.5  $\mu\text{m}$ , 5.8  $\mu\text{m}$  and 8.0  $\mu\text{m}$  bands (Guo et al., 2013).

### 3.3 BBG Selection Criteria

I use the strength of Balmer break feature, shifted to near infrared wavelengths, to develop a color criteria to identify post-starburst galaxies at  $3.0 < z < 4.5$ . The near infrared colors can also include a contribution from redshifted emission lines to broadband filters. Although we do not generally expect to have a strong emission spectrum for passively evolving galaxies, these emissions can mimic the Balmer break feature, leading to false identification of the BBGs. The post starburst galaxy SEDs in the redshift range of interest could get contributions from several nebular emission lines, with the most prominent being [OII] (3726Å and 3729Å), [OIII] (4959Å and 5007Å) and H $\beta$  (4861Å). In this Section I develop the method and the criteria for selection of the BBG candidates and discuss the effect of nebular emission on the BBG templates.

#### 3.3.1 Color-Color selection method

The Balmer break feature in post-starburst galaxies causes a break in the broadband colors of galaxies that can be used to identify the BBGs. In the redshift range of this study, the Balmer break (at rest-frame 3648Å) falls between the WFC3  $H_{160}$  and the HAWK-I  $K_s$  filters. Therefore, I use  $(H_{160} - K_s)$ , straddling the Balmer break feature, as the primary color for identifying the quiescent galaxies. Figure 3.1 shows a sample post-starburst galaxy template at redshift  $z = 3.9$  with relatively old stellar population (Age > 350 Myr) and no dust extinction. The blue and red curves show the filter response functions of the WFC3  $H_{160}$  and the HAWK-I  $K_s$  respectively. At the redshift of this galaxy these filters probe the blue and red sides of the Balmer break.

I use the synthetic spectral energy distribution code from Bruzual and Charlot 2003 (BC03; Bruzual and Charlot, 2003) to create a library of model SEDs of galaxies spanning a wide range in parameter space and different galaxy types. I consider an exponentially declining star formation history ( $\text{SFR} \propto \exp(-t/\tau)$ ) for all of our models with the characteristic time scale for star formation,  $\tau$ , ranging from 0 to 200 Myr with steps of 25 Myr. I

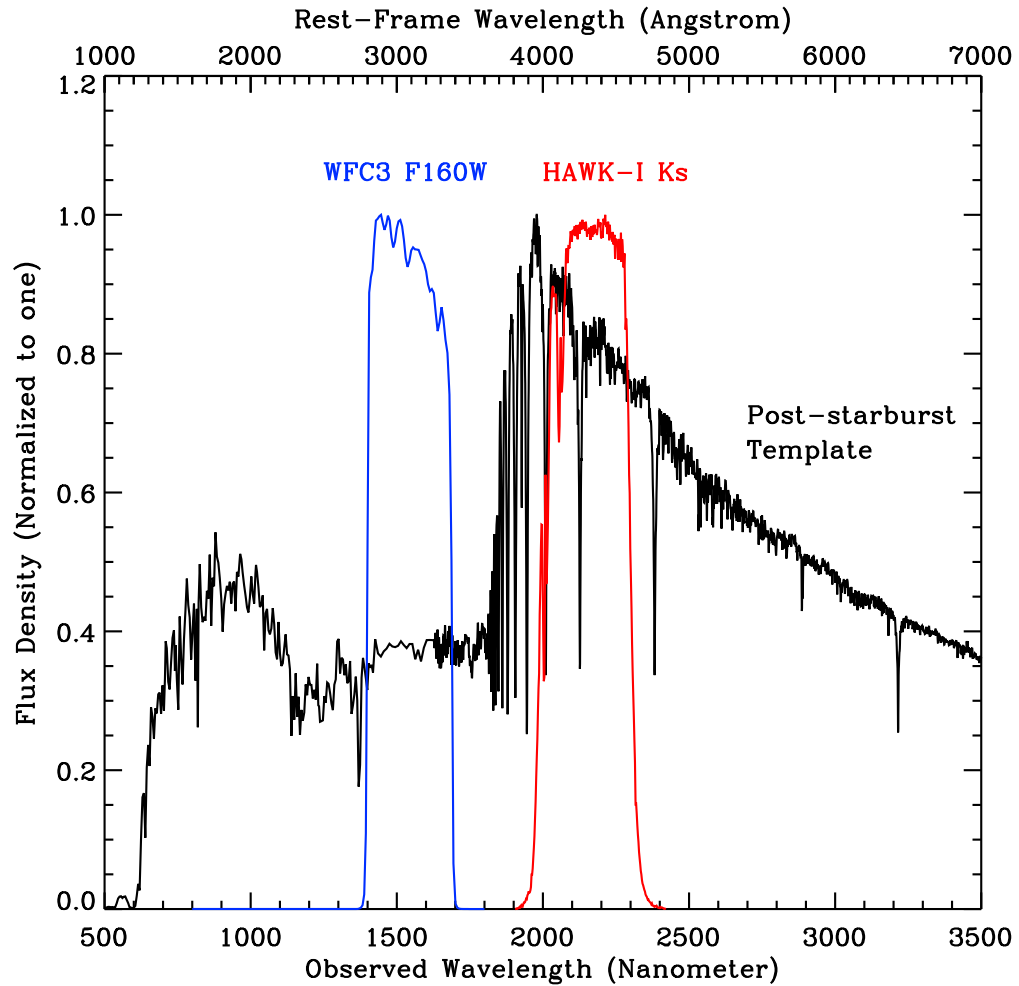


**Figure 3.1:** A post-starburst galaxy template SED ( $F_\lambda$ ) at  $z = 3.9$  (black) with the WFC3  $H_{160}$  (blue) and HAWK-I  $K_s$  filters (red) straddling the Balmer break at observed  $1.8 \mu m$  (the plots have been normalized to a peak of one).

**Table 3.1:** Parameters used for the model evolutionary tracks.

Models	Age (Gyr)	Extinction E(B-V)	$\tau$ (Gyr)	Redshift
Post Starburst	0.3-1.5	0.0-0.2	0.0	0.0-9.0
Dusty Starburst	0.005-0.1	0.4- 0.9	0.0-0.2	0.0-9.0
Elliptical	1.5-2.5	0.0	0.0	0.0-3.0

use a Salpeter initial mass function and use solar metallicity. I used the Calzetti attenuation curve (Calzetti et al., 2000) for treatment of the extinction with color excess E(B-V) ranging from 0 to 0.9 (corresponding to  $A_v = 0 - 3.6$ ) in steps of 0.05. Attenuation due to neutral Hydrogen in the intergalactic medium was estimated using Madau’s prescription (Madau, 1995) which is based on the neutral Hydrogen absorption of the UV flux of high redshift galaxies. The age parameter, defined as the time since the onset of recent star formation, ranges from 0 to 2.5 Gyr (from 5 to 30 Myr in steps of 5 Myr, from 30 to 100 Myr in steps of 10 Myr and steps of 100 Myr after that). The redshift range varied from  $z=0$  to 9 in redshift bins of  $\Delta z = 0.1$ . The maximum age possible in each redshift is limited to the age of the Universe at that redshift.

I divide galaxy models into three different categories: The dusty starburst galaxies with an exponentially declining star formation history, moderate to high values of extinctions and relatively young ages (measured from the onset of star formation); the elliptical galaxies with no dust extinction and old ages; and the passively evolving post-starburst galaxies with moderate ages and low extinction values. The dusty starburst galaxies could also have an older age but with a new burst of star formation. The post-starburst galaxy population is considered to be the phase after the initial starburst in galaxies when the more massive stars leave the main sequence after few hundred million years and is considered to be the phase before galaxies evolve into the early types at the lower redshifts with very old ages. The parameters used for the model evolutionary track are listed in Table 3.1.

I integrated the WFC3 near-IR and HAWK-I  $K_s$  band filter response functions over the model SEDs and found the corresponding magnitudes in the desired filters after incorporating the stellar and intergalactic extinctions. Changes in the color evolutionary tracks with

redshift were then calculated. The degeneracies in the stellar population model parameters such as age, redshift and extinction, can also lead to red ( $H_{160} - K_s$ ) colors. It is important to use more than one color to break the degeneracy between the high redshift relatively quiescent galaxies (BBGs) and the dusty starburst systems. Therefore, in addition to the main ( $H_{160} - K_s$ ) colors I used the WFC3 ( $J_{125} - H_{160}$ ) and ( $Y_{105} - J_{125}$ ) and also non-detection conditions in the U and  $B_{435}$  bands in order to minimize the fraction of the contaminants. The region on the color-color plots where BBG candidates are located is shown as the grey shaded area in Figure 3.2. This is adopted to minimize the number of contaminants.

Therefore, for the post starburst galaxies on the ( $Y_{105} - J_{125}$ ) vs ( $H_{160} - K_s$ ) plot, I choose the following selection criteria:

$$S/N(U) < 2, \tag{3.1a}$$

$$S/N(B_{435}) < 2, \tag{3.1b}$$

$$(Y_{105} - J_{125}) < -3.44 + 3.40 \times (H_{160} - K_s), \tag{3.1c}$$

$$(Y_{105} - J_{125}) > 1.03 - 0.67 \times (H_{160} - K_s), \tag{3.1d}$$

$$(Y_{105} - J_{125}) > -0.83 + 0.67 \times (H_{160} - K_s). \tag{3.1e}$$

and for the ( $J_{125} - H_{160}$ ) vs ( $H_{160} - K_s$ ) plot, I choose:

$$S/N(U) < 2, \tag{3.2a}$$

$$S/N(B_{435}) < 2, \tag{3.2b}$$

$$(J_{125} - H_{160}) < -2.48 + 2.80 \times (H_{160} - K_s), \tag{3.2c}$$

$$(J_{125} - H_{160}) > 1.70 - (H_{160} - K_s), \tag{3.2d}$$

$$(J_{125} - H_{160}) > -0.16 + 0.43 \times (H_{160} - K_s). \tag{3.2e}$$

Equations 3.1a-3.2e correspond to the shaded region in Figure 3.2 and are taken as our BBG selection criteria. In addition to the color location within the diagram, I imposed an additional constraint. The selected BBGs should also not be detected in the U and ACS  $B_{435}$  bands, as in the redshift range of our interest the Lyman break falls long-ward of these filters. These additional conditions help in removing the lower redshift contaminants from the sample.

To further test the validity of the selection criteria, I generated post-starburst and dusty starburst evolutionary tracks as a function of the age of the galaxy. Analysis of these age-dependent evolutionary tracks recovers the same selection criteria that I originally identified for post-starburst galaxies. Also I find that the main source of contamination is from very dusty starburst galaxies with strong nebular emission lines (and not lower redshift early type galaxies).

### 3.3.2 Simulations

In order to assess the robustness of our color selection criteria I generated a WFC3  $H_{160}$ -band selected mock catalog. The simulated catalog resembles the GOODS-S field as closely as possible. It has the same filters with the same wavelength, coverage area and photometric depth. I use the observed luminosity functions from Dahlen et al., 2007 and randomly extracted galaxies with different absolute magnitudes from the luminosity function and randomly assign redshifts to each extracted galaxy. I then assigned spectral types to the simulated galaxies in the three main categories of early types, late types and starbursts. I then randomly assign photometric errors to the simulated galaxies and I add extinction spanning the range  $E_{B-V} = 0 - 0.9$ , based on the galaxies assigned spectral types.

The simulated catalog contains sources to a detection limit of  $3\sigma$  in F160W. I used the observed Coleman, Wu and Weedman (CWW) spectral templates (Coleman et al., 1980) to calculate the K-correction. Using the assigned redshift to calculate the distance modulus, I measured the apparent magnitude in each of the filters for the simulated galaxies. The

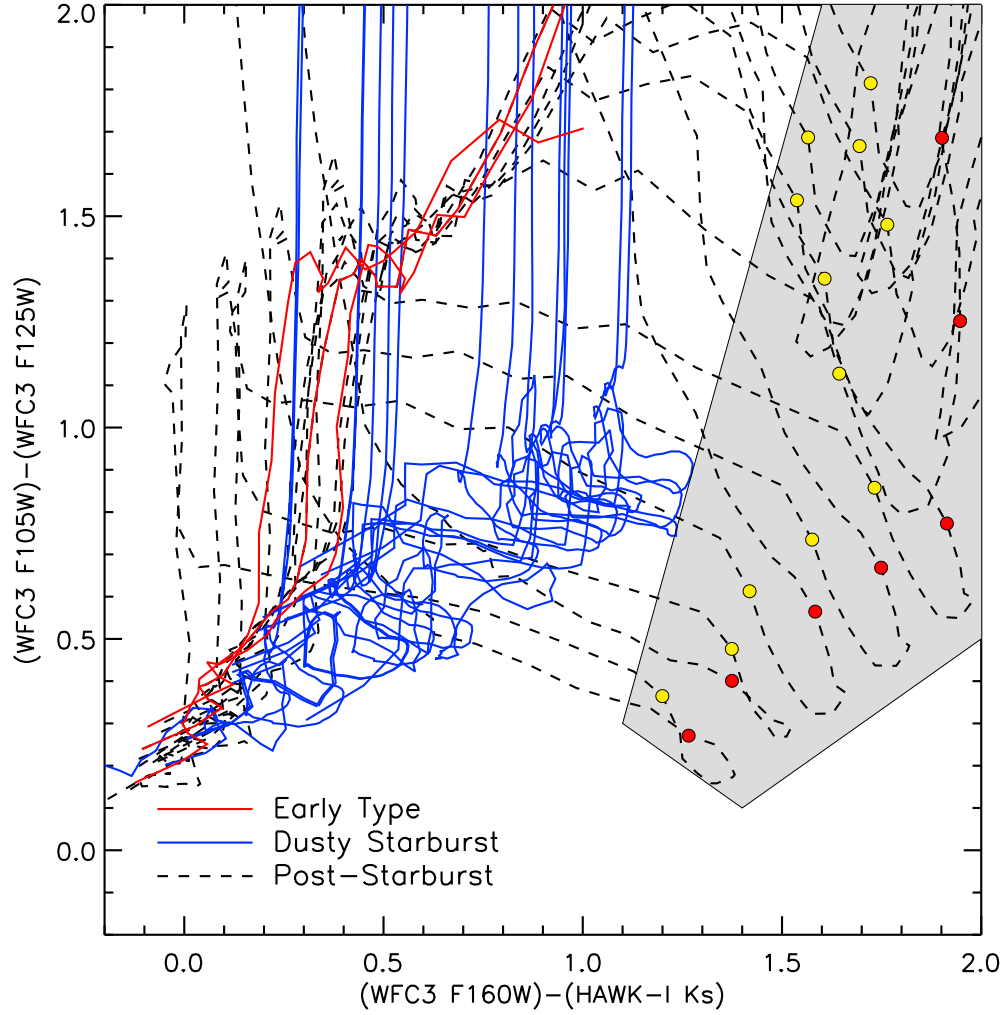


**Figure 3.2:**  $(Y - J)$  versus  $(H - K_s)$  (left) and  $(J - H)$  versus  $(H - K_s)$  (right) evolutionary tracks from BC03 models. In both plots solid red, solid blue and dashed black evolutionary tracks represent elliptical, dusty starburst and post starburst galaxies respectively. The parameters used to generate the model tracks are listed in Table 3.1. The yellow and red circles on the post-starburst galaxy tracks correspond to redshifts 3.0 and 4.5 respectively. The BBG selection criteria is identified by the grey shaded area on the plots.

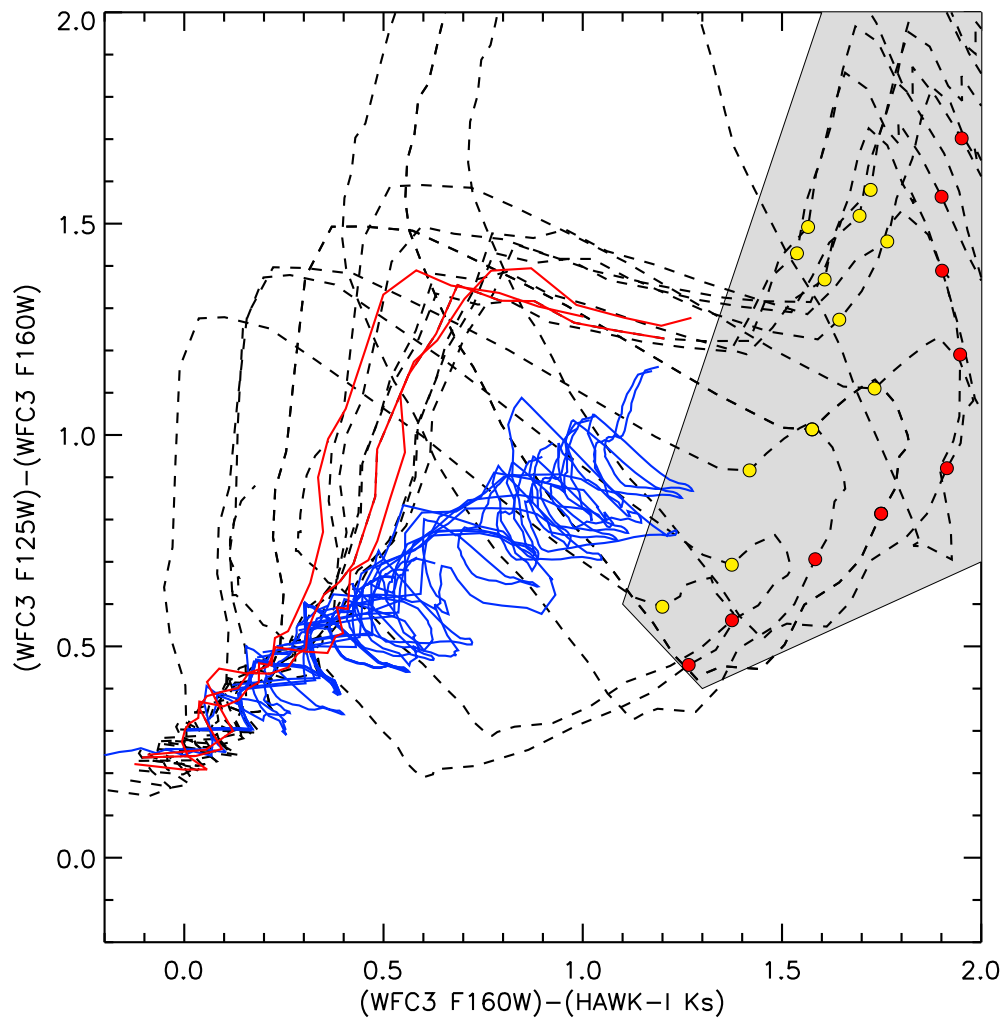


Figure 3.2: Continued.

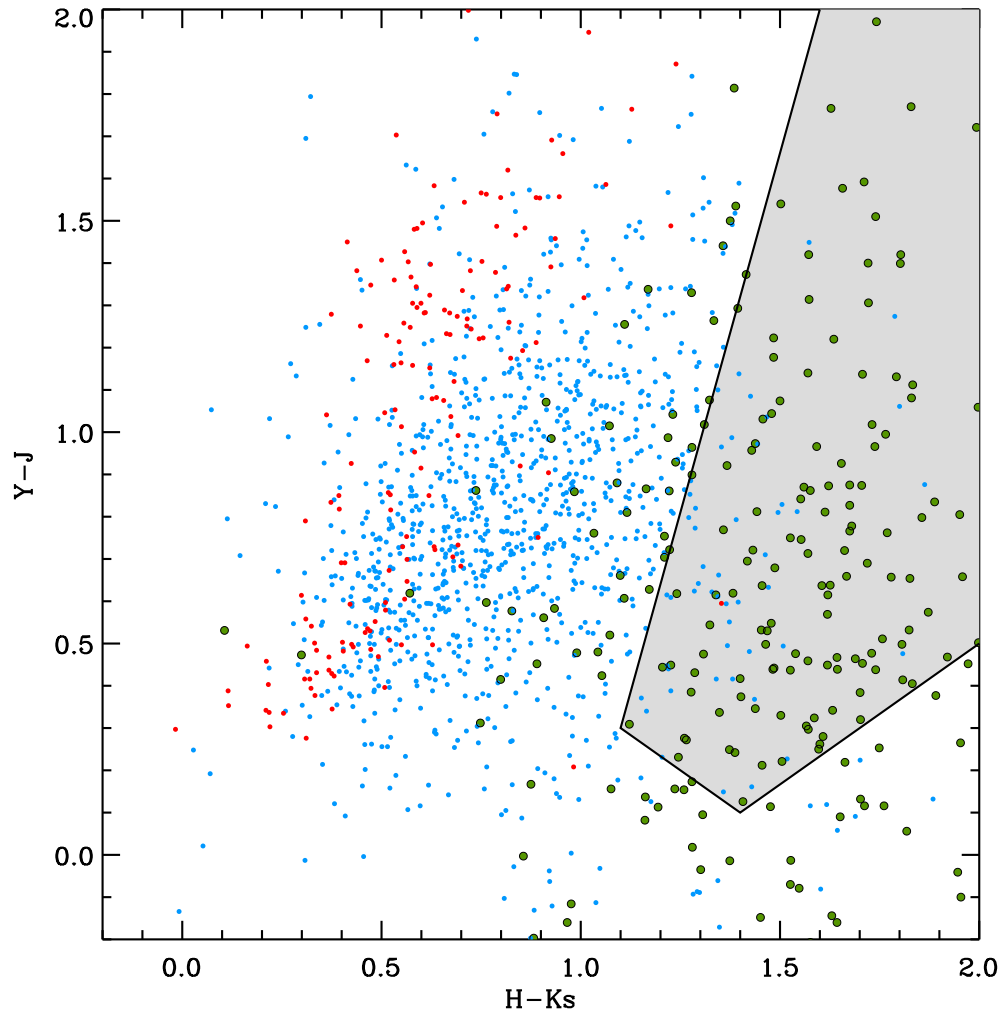
result is a mock galaxy catalog with apparent magnitudes in the same filters as in the GOODS-S, redshifts, spectral types and extinction values.

Figure 3.3 shows the simulated color-color plots overlaid on the BBG selection criteria developed in Section 3.1. The green points represent the post-starburst galaxy population in the mock catalog that are in the redshift range  $z \simeq 3-4.5$ . I also show the simulated data for the early type and dusty starburst galaxies as red and blue points respectively. The simulations show that there is very little contamination from the elliptical galaxies while the dusty starburst galaxies still contaminate the BBG sample. I will address this issue later in Section 4 when I fit the spectral energy distribution of the BBG selected candidates to galaxy models.

### 3.3.3 Candidate Identification from the color-color Criteria

I applied the BBG selection criteria derived in Section 3.1 to the deep WFC3  $H$ -band selected TFIT catalog, setting a  $10\sigma$  detection requirement in the WFC3  $H$ -band for the catalog. I apply the  $(Y_{105} - J_{125})$  vs  $(H_{160} - K_s)$  and  $(J_{125} - H_{160})$  vs  $(H_{160} - K_s)$  criteria on the WFC3  $H$ -band selected catalog. I find a total of 24 sources in the combined two selection criteria identified as BBG candidates. Figure 3.4 shows the color selection criteria as the shaded region along with data from the  $H$ -band selected TFIT catalog. Sources that are within the shaded region but did not satisfy the U and/or B bands non-detection conditions were not included. The SEDs of all the identified candidates show pronounced Balmer breaks between the WFC3 H and HAWK-I  $K_s$  bands, as expected from the color selection.

One widely used selection criteria for distinguishing quiescent galaxies from star forming systems is by using the rest-frame U, V and J in a (U-V) vs. (V-J) color plot (the so called UVJ selection; Labbé et al., 2005; Wuyts et al., 2007; Williams et al., 2009). The bimodality between dusty star forming and quiescent galaxies in the UVJ selection becomes less prominent at  $z > 2$  mostly because of photometric redshift uncertainties and weaker fluxes (Williams et al., 2009). Figure 3.5 shows the distribution of the near infrared BBG



**Figure 3.3:** Simulation color-color diagrams. The blue, red and green data points correspond to elliptical, dusty starburst and post starburst galaxies from our simulation respectively with the BBG selection shown as grey shaded area. Although we get very little contamination from the lower redshift early type galaxies (red points), the dusty star-forming systems could still contaminate the sample (blue points).

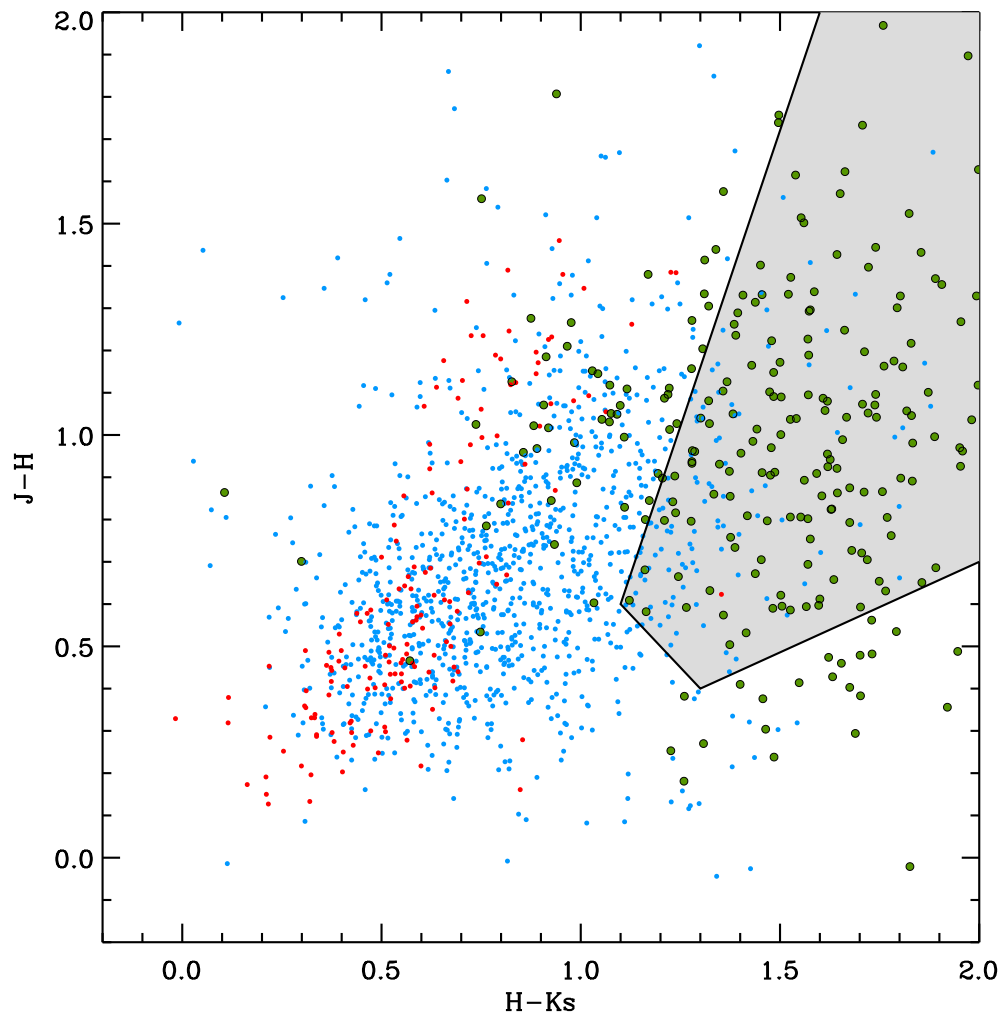
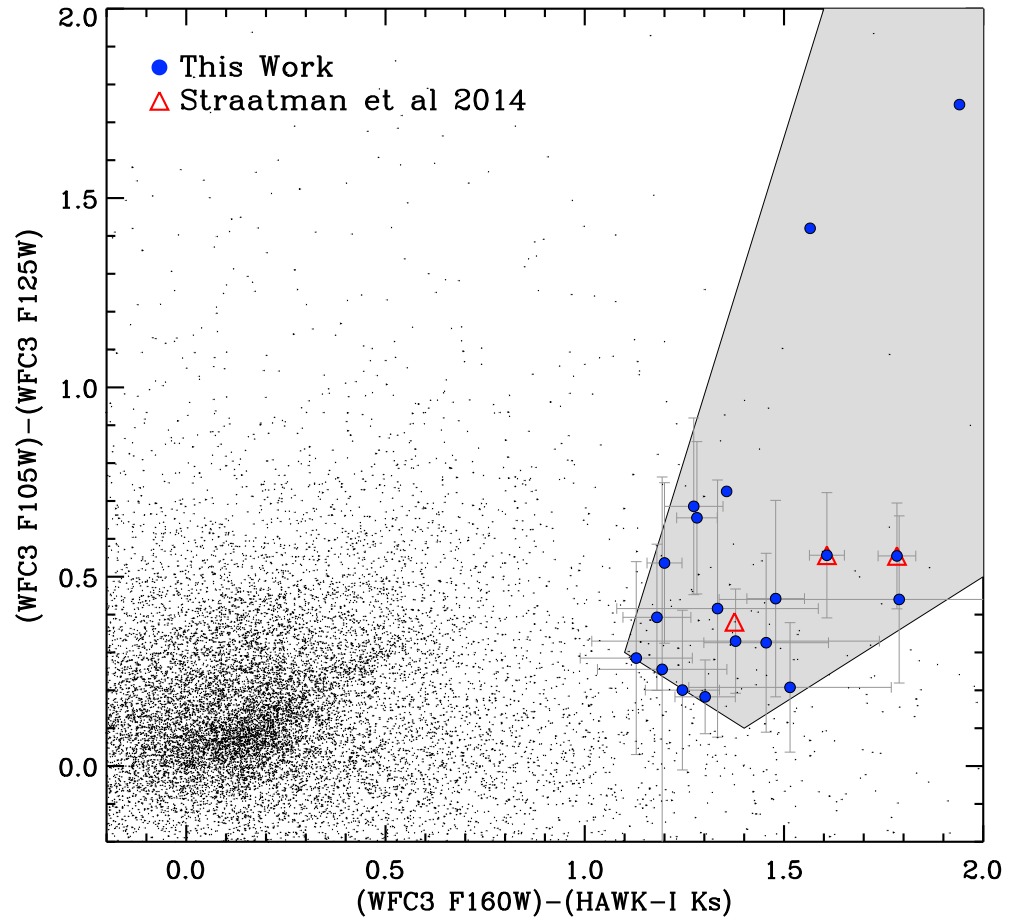


Figure 3.3: Continued.



**Figure 3.4:** Left: The  $(Y - J)$  vs  $(H - K_s)$  selection criteria (Eq. 1) applied to the CANDELS WFC3  $H$ -band selected TFIT data (black data points). Right: Plot of  $(J - H)$  vs  $(H - K_s)$  (Eq. 2). Blue circles correspond to the selected candidates that lie within the selection criteria and are not detected in the U and B bands (i.e., are at  $z \sim 3$  and  $z \sim 4$ ). The red triangles are the UVJ selected passive systems by Straatman et al., 2014. The final candidates are from the two combined color-color plots.

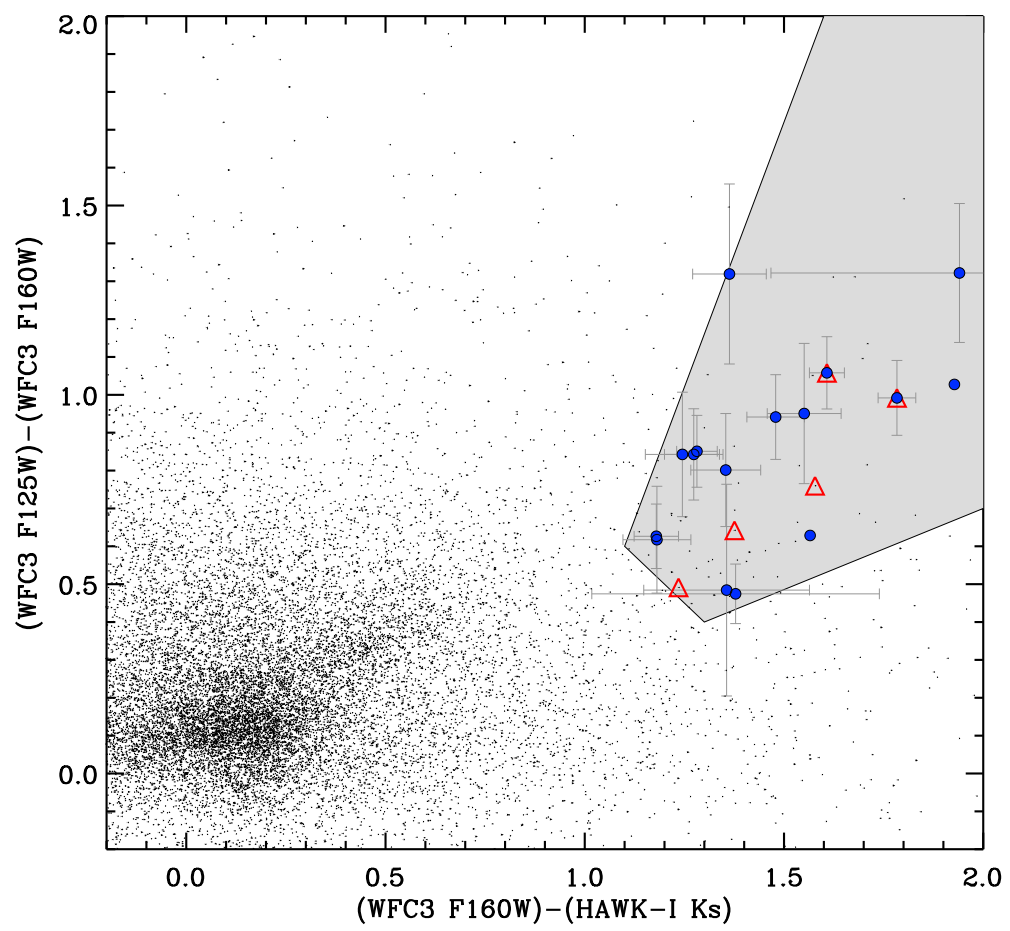


Figure 3.4: Continued.

selected sources on a UVJ color-color plot. I see from the Figure that many of the candidates are at the boundary of dusty star-forming and quiescent criteria or will be identified as dusty galaxies by this selection.

Recently Straatman et al., 2014; Spitler et al., 2014 extended the UVJ selection of passive galaxies to  $z \sim 3 - 4$  using medium band data. The UVJ selected quiescent candidates by Straatman et al., 2014 are plotted along with the BBG selected candidates in Figure 3.4. All the UVJ selected quiescent candidates fall on the BBG color selection criteria while not all of them are selected as BBG candidates because of the additional criteria imposed on the U and  $B_{435}$  bands.

Additionally the high redshift massive galaxies could be selected based on the information contained in their full SEDs. This method is based on a selection from the photometric redshift and mass derived from the SED fittings to look for high redshift massive galaxies. Although this method could potentially recover the BBG sources identified here, it is difficult to model the behavior of these systems from simulations the same way that we performed this for the color-color selected sources.

### 3.3.4 Effect of Nebular Emission on the BBG Selection

The nebular emission lines can play a significant role in both the selection and SED fitting of the BBG candidates. The sensitivity of the final estimated parameters on the nebular emission will be discussed in Section 4 while, here I examine the effect of nebular emission on colors and hence on selection of the BBGs.

I account for the effect of nebular emission (both continuum and emission lines) following Schaerer and de Barros, 2009 and Schaerer and de Barros, 2010. The strength of nebular emission depends mainly on the number of Lyman continuum photons, which is computed from stellar population synthesis models. Relative line intensities are taken from Anders and Fritze-v. Alvensleben, 2003 and Storey and Hummer, 1995, for a typical ISM ( $n_e = 100 \text{ cm}^3$ ,  $T = 10^4 \text{ K}$ ). I assume that the Lyman escape fraction is equal to zero, which means that our models produce the maximum theoretical strength for nebular emission (under

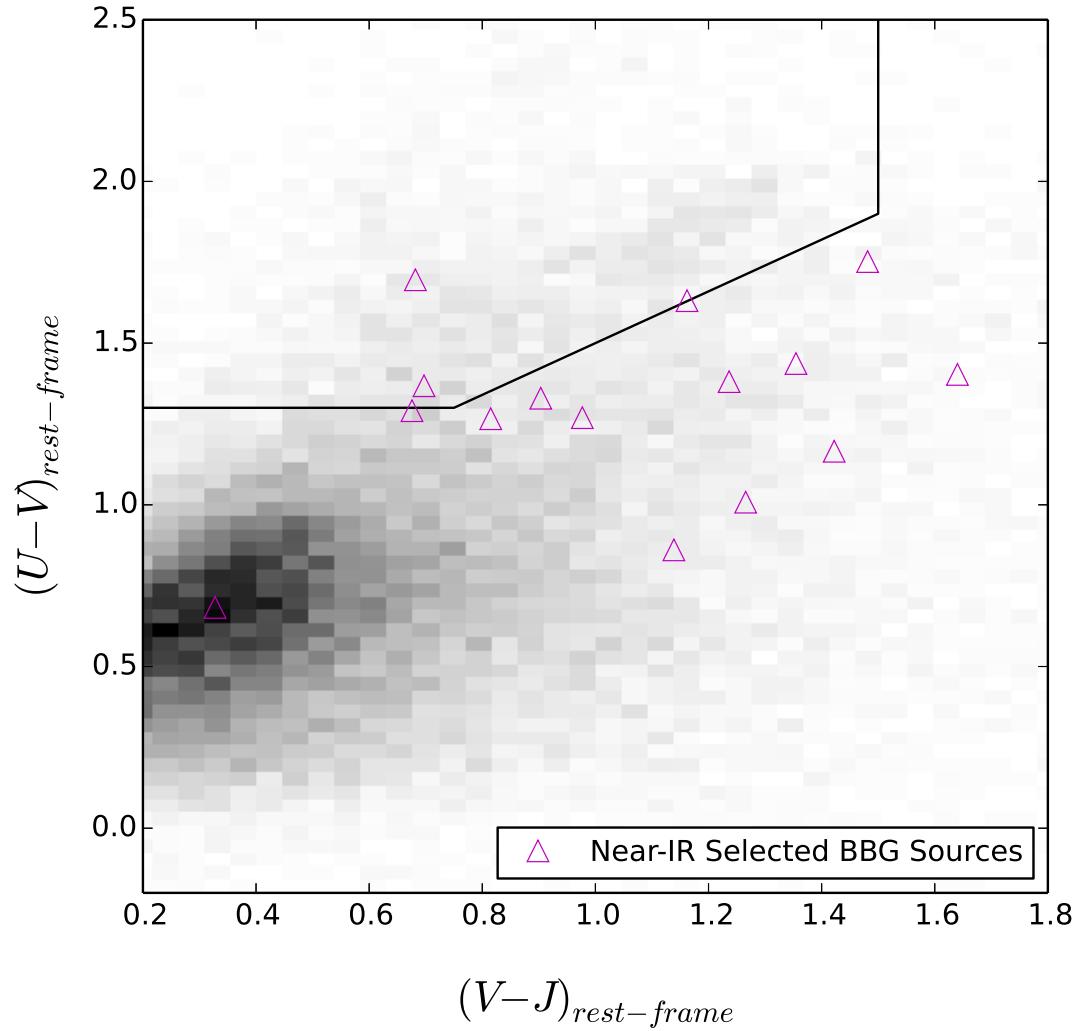


**Figure 3.5:** Distribution of the near infrared color selected BBG sources on the rest-frame UVJ color selection criteria (Williams et al., 2009). The area on the plot shows the UVJ predicted location for quiescent galaxies. The BBG selected sources fall close to the boundary of dusty star forming and quiescent candidates.

our assumptions about the ISM). Additionally, I also apply the same attenuation between nebular and stellar emission.

Figure 3.6 shows an example of the observed photometry for one of our BBG candidates at  $z = 3.6$ , along with fitted template SEDs without nebular emission (green), showing the Balmer break at  $\sim 2\mu\text{m}$ , and with nebular emission (blue). This reveals how redshifted nebular emission could disguise itself as a Balmer break feature. The infrared broadband photometry of the candidates could also be affected by the nebular emission lines. In particular, in the redshift range covered in this study, the  $\text{H}\alpha$  line at rest-frame  $6563\text{\AA}$  could potentially contaminate the IRAC  $3.6\mu\text{m}$  flux at  $z \sim 3.8$ . In order to further study the effect of nebular emission lines on the SED fit for our candidate galaxies, I measured the IRAC ( $m_{3.6} - m_{4.5}$ ) color of BBG sample as the presence of the  $\text{H}\alpha$  line is only expected to affect the  $3.6\mu\text{m}$  band as it shifts to this band at  $z \sim 3.8$ . For our BBG sample, there are four galaxies that have both IRAC  $3.6\mu\text{m}$  and  $4.5\mu\text{m}$  detections at the redshift range affected by this emission. Figure 3.7 shows the IRAC colors of the four BBG candidates for which  $\text{H}\alpha$  emission lines shift to the IRAC  $3.6\mu\text{m}$ . For three of these candidates, it is clear that the observed infrared colors are better represented by model SEDs that include nebular emission in the fit, accounting for the  $\text{H}\alpha$  contribution. Post-starburst galaxies are relatively old systems and I do not expect to see strong  $\text{H}\alpha$  emission in their spectra. The candidates that are affected by this feature are relatively younger. Figure 3.7 implies that the absence of correction for nebular emission in the redshift range of interest here would lead to redder ( $m_{3.6} - m_{4.5}$ ) colors, which would mimic the Balmer break and hence, overestimate their stellar mass.

In order to better quantify the effect of nebular emissions, I also generated color evolutionary tracks for the post-starburst galaxies including contribution from nebular emission and recovered the same color selection criteria as for the model tracks in Figure 3.2, where no nebular emissions were incorporated. The effect of nebular emission on evolutionary tracks is most noticeable for dusty star-forming galaxies. For the highly dusty star-forming systems, inclusion of nebular emission would further shift them into the BBG selection do-

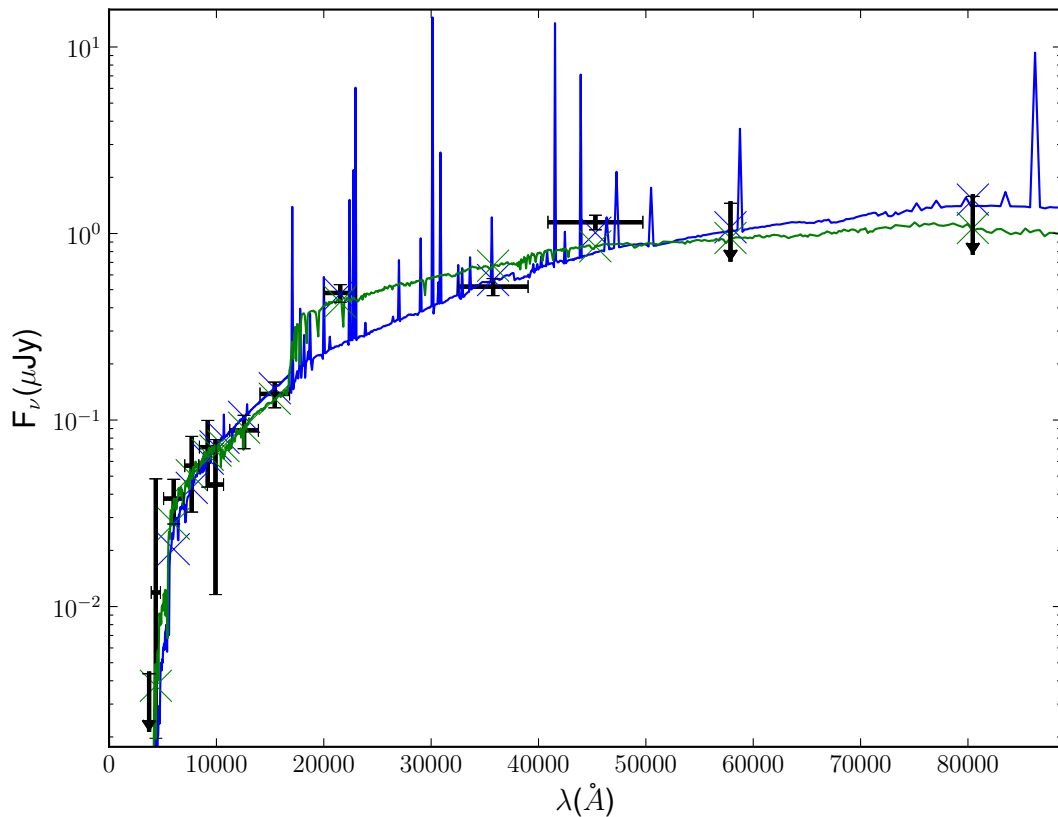


**Figure 3.6:** Example of an SED fit to a BBG candidate at  $z=3.60$  without nebular emission (green) and with nebular emission (blue). This shows the extent to which nebular emission could mimic the Balmer break feature shifted to near IR.

main, further contaminating the sample. Most of the contamination in the sample comes from this heavily dust obscured, young and star-forming population.

### 3.4 Measurements of the Observable Parameters

In this Section I study the nature of the BBG candidates by measuring their physical properties (i.e. stellar mass, age etc.). I use this to examine if the candidates fit the expected requirements for the BBGs. The photometric redshifts and physical parameters

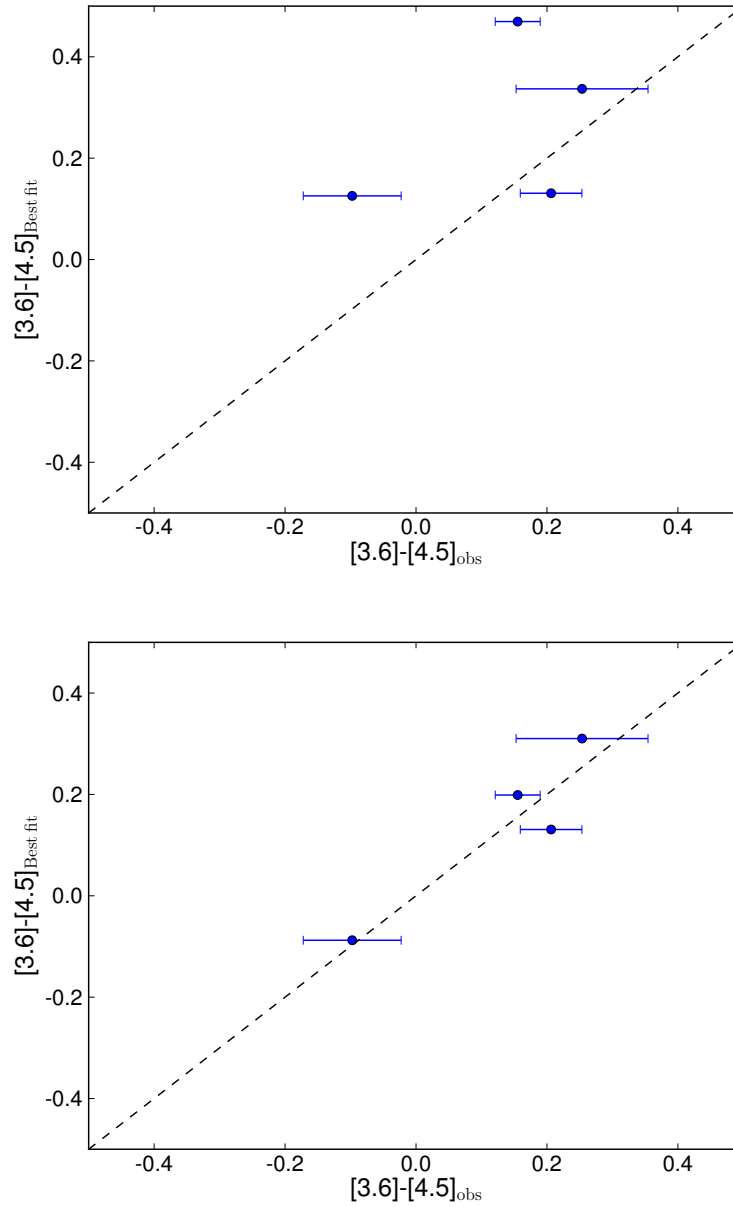


**Figure 3.7:** Top: The observed IRAC colors of the 4 BBG candidates with strong contribution from the  $\text{H}\alpha$  shifted to the infrared pass-bands are plotted against the best fit model color with no nebular emission contributions incorporated in the fit. Bottom: Same as the left plot but with nebular emission added to the fit.

of the BBG candidates, selected from the criteria in Section 3.1, are inferred from fitting the observed SEDs with a BC03 generated template library using a modified version of the SED fitting code HyperZ (Bolzonella et al., 2000). In the SED fitting code, the redshift is a free parameter that is allowed to vary from  $z=0$  to  $z=9$  for fits with and without nebular emission. I consider solar metallicity and allow the extinction to vary from  $0 < A_v < 3$ . In the following I will discuss the SED fitting results of BBG selected sample.

### 3.4.1 Effect of Nebular Emission on Parameter Estimation

Adding nebular emission to the SED fitting is expected to lower the age and stellar mass estimate for the candidates that are affected by these emissions as it would reduce the mass to light ratio of these systems.

Figure 3.8 compares the stellar mass estimates for the BBG sample with and without nebular emission. Here, the blue filled circles correspond to the BBG candidates for which the SED fit, after adding nebular emission, gives a lower age estimate (by more than 0.5 dex). There is excellent agreement between the stellar mass estimates for the BBG candidates for which the difference in age estimate is small ( $\Delta \log(\text{age}) < 0.5$ ). Figure 3.9 shows the age distribution of the color-selected BBG candidates that are affected by the nebular emission (blue filled circles in Figure 3.8). Here, including nebular emission in the fit significantly affects their parameter estimation as seen from the distributions. Out of the 24 BBG candidates selected from color-color plots, 8 show strong nebular emission effect in their SED fit and were removed from the BBG sample as this causes false identification. The three candidates mentioned in Section 3.4 as having strong  $H\alpha$  contamination are among these 8 galaxies. The strong nebular emission line galaxies are identified based on having a better  $\chi^2$  fit with nebular emission. Figure 3.10 shows the postage stamp images of the final 16 BBG candidates in the multi-waveband. I see from this Figure that many of the BBG selected sources are relatively compact. This is in agreement with recent studies indicating that the first galaxies to become passive in the Universe are the massive compact systems (Cassata et al., 2013; Williams et al., 2014a).

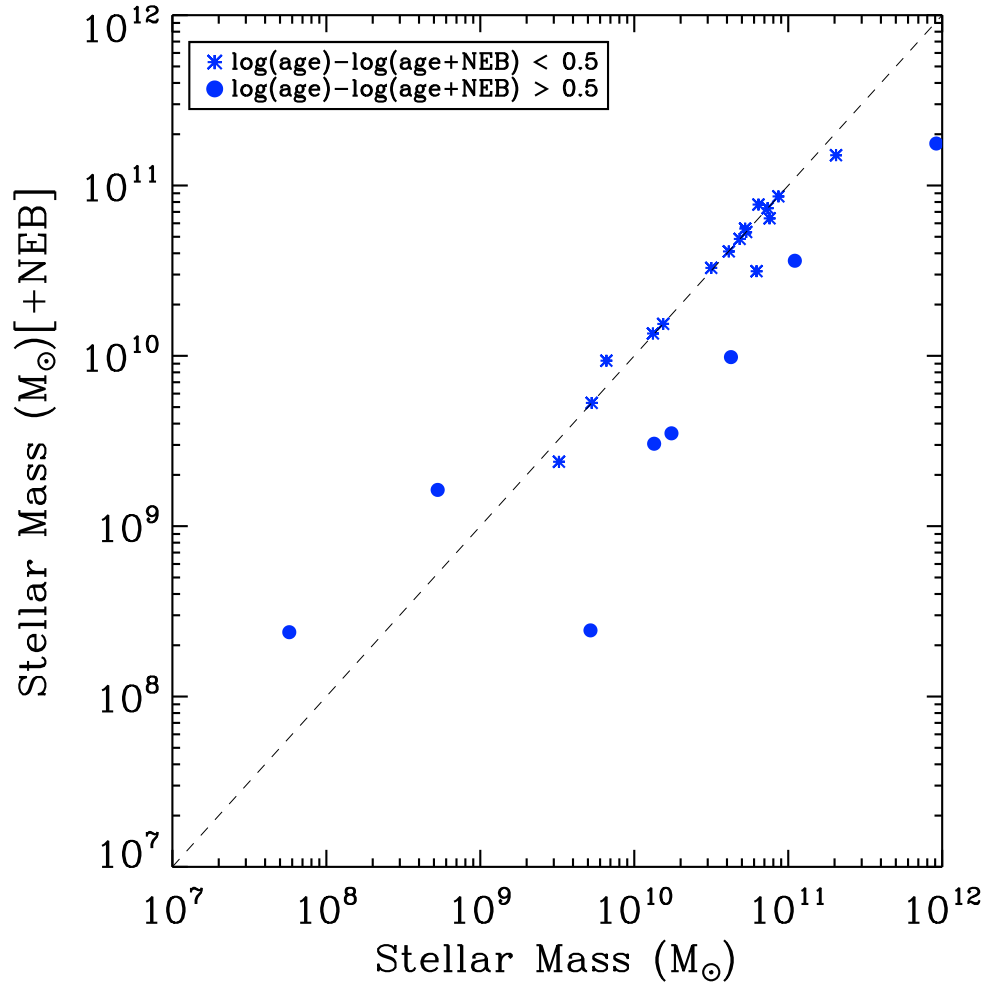


**Figure 3.8:** Comparison of the stellar mass values for BCGs estimated with and without including nebular emission contribution. The blue filled circles correspond to sources with an age estimate difference of larger than 0.5 dex in fits with and without nebular emission.

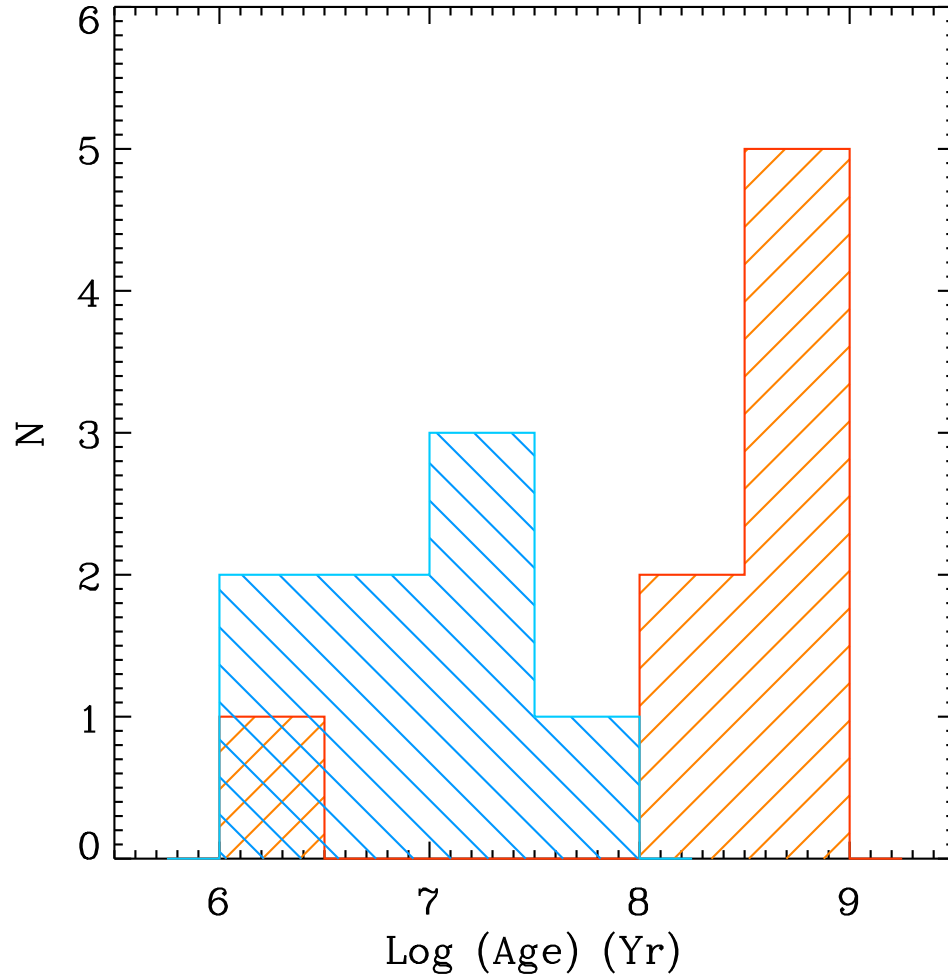


**Figure 3.9:** The age distribution of BGGs shown with filled symbols in Figure 3.8. The red histogram shows the age distribution of these sources without nebular emission added to the SED fit and the blue histogram is the age distribution with the nebular emission effect added to the fit. These are the galaxies for which both their age and stellar masses are sensitive to the inclusion of nebular emission lines. Clearly including nebular emission lines leads to younger ages and lower stellar mass estimates.

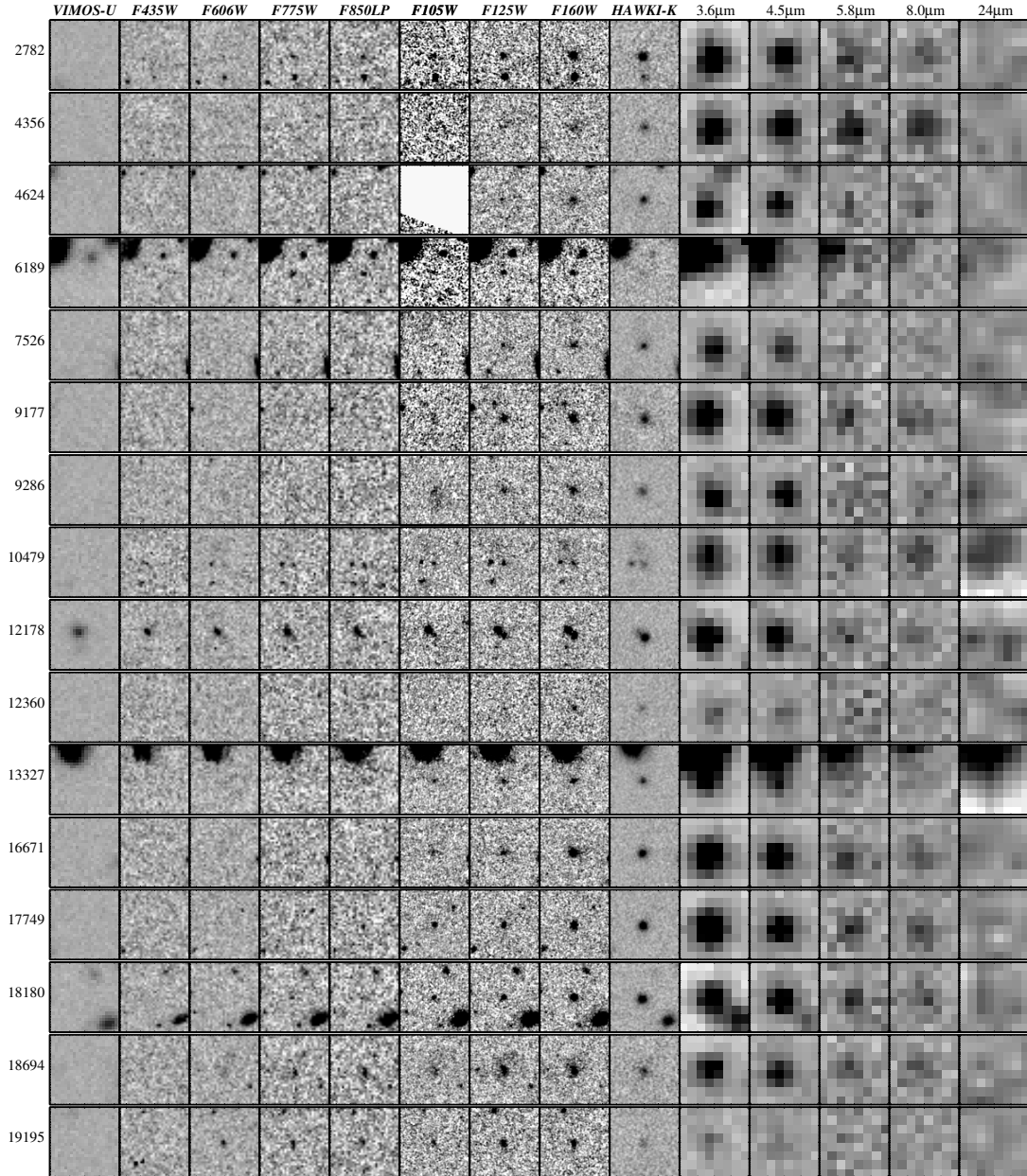


**Figure 3.10:** Postage stamp images of the BBG candidates. From left to right, the VLT/VIMOS U band, ACS optical, WFC3 near-IR, VLT/HAWKI  $K_s$ , Spitzer IRAC and MIPS 24 micron bands. The candidates are very faint in the bluer bands and get brighter in the redder bands. Three of the candidates are marginally detected in the MIPS 24  $\mu$ m. The cutouts are  $5'' \times 5''$  in size.

### 3.4.2 Photometric Redshift

By fitting the SED for individual BBGs, I estimated the photometric redshifts for each of our candidates selected from the color criteria. The relatively quiescent galaxy candidates at  $z \sim 3 - 4$  currently lack spectroscopic confirmation due to the absence of prominent emission features because of their passive nature which would not allow us to further check the robustness of the estimated photometric redshifts. Figure 3.11 shows the distribution of the photometric redshifts for the color selected BBG candidates. As expected, the BBG population has a redshift distribution that peaks between  $3.0 < z < 4.5$ .

### 3.4.3 Mass Measurement

The stellar masses for the BBG candidates were measured by fitting their SEDs to templates generated from the population synthesis models. In Figure 3.11 I plot the distribution of their stellar masses. The distribution has a median at  $\log(M/M_{\odot}) \sim 10.6$ . Mid-infrared observations by the Spitzer Space Telescope provide a direct measure of the stellar mass at the redshift range considered here (Papovich et al., 2006; Yan et al., 2006). Massive galaxies are brightest in the rest frame near-IR band and at the redshift range considered here, that roughly corresponds to the observed IRAC 4.5  $\mu\text{m}$ . The accuracy of the selection criteria and the estimated parameters are therefore directly affected by the depth and quality of the IRAC data. Therefore, the very deep IRAC data at 3.6  $\mu\text{m}$  and 4.5  $\mu\text{m}$  are essential for the present study as they are probing red-ward of the Balmer break. As discussed in Section 2.4, the depth achieved in the SEDS data (Ashby et al., 2013) gives a unique opportunity to constrain the SEDs of the most massive galaxies and to accurately measure the mass.

### 3.4.4 Extinction

I derive the extinction of the BBGs from SED fitting. The extinction is added to the templates used for the SED fitting in the range of  $0 < A_v < 3$ . Figure 3.11 shows the extinction distribution for the color selected BBGs. From our classification in Table 3.1 we see that the post starburst population has modest extinction values. Figure 3.11 shows

that the majority of the BBGs have low to moderate extinction values. There are four color selected candidates that have relatively large derived extinctions of  $E(B - V) > 0.3$ . These galaxies have relatively large SED inferred SFRs indicating that they could be part of the dusty galaxy population that contaminate the sample by replicating near IR colors of the BBGs. I will further discuss this population in Section 5.

### 3.4.5 Age

The ages of the BBG sample are plotted in Figure 3.11. Age is perhaps the most loosely constrained parameter in the SED fit. It is also the parameter that affects the near infrared colors of the post-starburst evolutionary tracks the most. The BBGs are evolved population due to their strong Balmer breaks (Table 3.1) and have relatively old ages ( $\sim 10^9$  yrs). Also as I discussed earlier, this is the parameter that is most significantly affected (along with the stellar mass) by the presence of nebular emission lines in the SEDs of the galaxies (Figures 3.8 and 3.9). Adding nebular emission to the SED fit of few of systems requires extremely low ages (high SFR) which is at the order of the dynamical time scale for these systems.

## 3.5 MIPS detected BBGs

I now study the properties of our candidate BBGs as a function of MIPS detection at  $24 \mu\text{m}$ . The detection in the Spitzer MIPS at the redshift of interest here can be interpreted as due to dust. At this redshift, the MIPS (at  $24 \mu\text{m}$ ) probes rest-frame 5-6  $\mu\text{m}$  which can result from PAH feature i.e., star formation. I crossed-matched our BBG candidates selected from the color-color plots with the MIPS catalog for the GOODS-S (Magnelli et al., 2011), using a matching radius of 1.5 arcseconds. The matching radius is chosen to identify the MIPS sources while avoiding contamination from the neighbors. Out of 16 candidates identified as BBGs, 3 have a MIPS source associated with them. The bluest strong PAH band is at  $6.2 \mu\text{m}$  and for the BBG candidates to be bright enough to be detected by MIPS  $24 \mu\text{m}$  band (assuming that the photometric redshifts are correct) this would mean that the

detection is likely to come from hot dust continuum, most likely from an AGN. One of the sources is detected in both X-ray and MIPS, which indicates the presence of an obscured AGN. I find that the three candidate galaxies that are detected in the MIPS 24 micron have moderate to high extinctions, with the candidate that is selected in both the MIPS and the X-ray having SED measured color excess ( $E(B - V)$ ) of 0.6, indicating heavy dust obscuration. The candidates with MIPS and/or X-ray detections are listed in Table 3.2.

### 3.6 Comparison between the sources selected by the LBG and BBG techniques

I now compare photometric properties of the candidates selected by the LBG and BBG criteria. For consistency, I apply these techniques to the same parent sample of GOODS-S galaxies with the same photometry to minimize systematic effects. This approach helps us in better understanding the differences (or similarities) between the two populations of galaxies, color selected in different ways.

The LBG selection mostly targets star forming galaxies with the pronounced Lyman break at rest-frame  $912\text{\AA}$  while the Balmer break selection targets relatively quiescent systems with Balmer break feature at rest-frame  $3648\text{\AA}$ . In principle, the BBG selection is expected to complement the LBG selection by identifying galaxies with older stellar populations, missed from the LBG selection.

In order to directly compare the BBG and LBG populations, I use the LBG selection criteria to identify galaxies over the same redshift range and area as the BBG sample in this study ( $3.0 < z < 4.5$ ), using the same photometric data. This reduces sources of bias, providing a direct comparison between the two populations and selection methods. I use B-dropout selection criteria developed in Stark et al., 2009 as the criteria for LBG selection. Using the same photometric catalog and library of model galaxies to generate template SEDs, I fitted the SED of the LBG candidates and estimated their Phot- $z$ , stellar mass, age and extinction. Figure 3.12 compares the distribution of these values for the BBG and

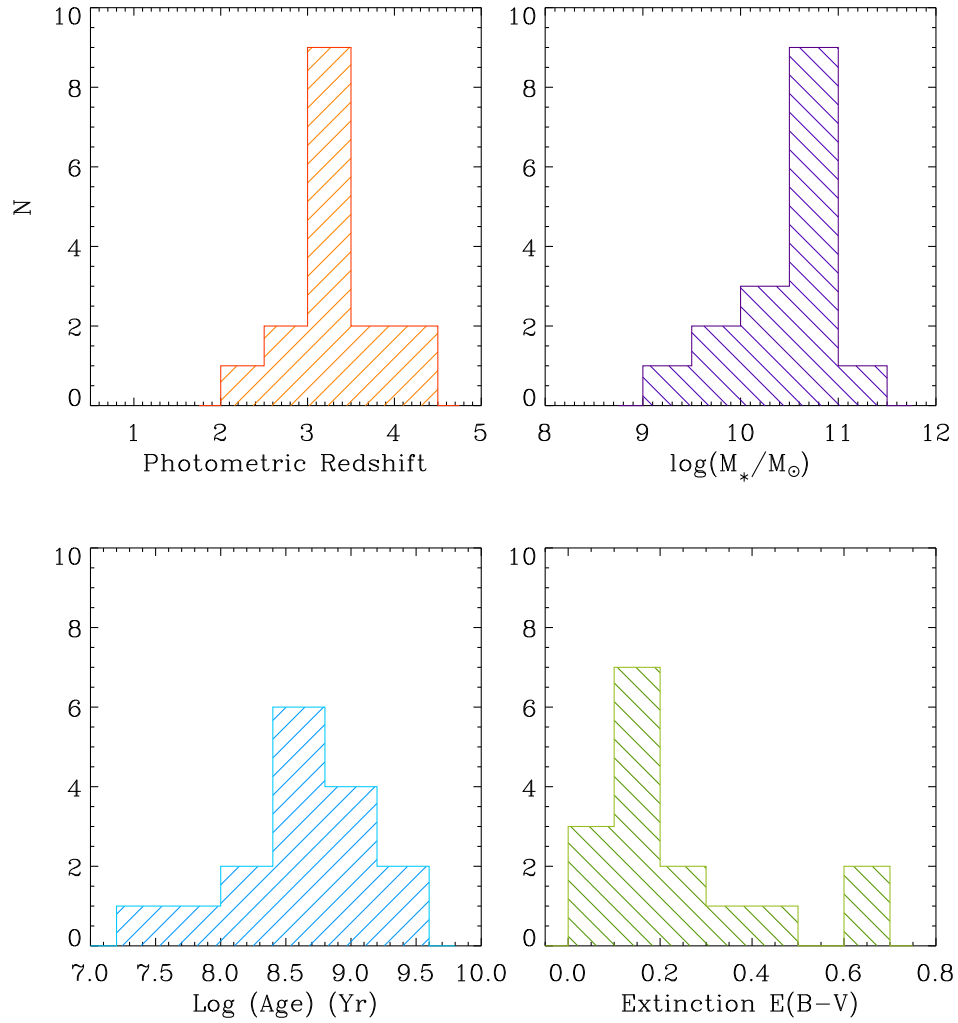


**Figure 3.11:** Properties of the BGG candidates selected from the color-color criteria. From left to right: Photometric redshift distribution showing that most of the color selected BGGs has Phot-z distributions that are consistent with the redshift range of interest here. Mass distribution showing that the BGG selection is targeting the more massive galaxy population. Age distribution indicating that our selection targets evolved systems. Extinction distribution showing the range of reddening values.

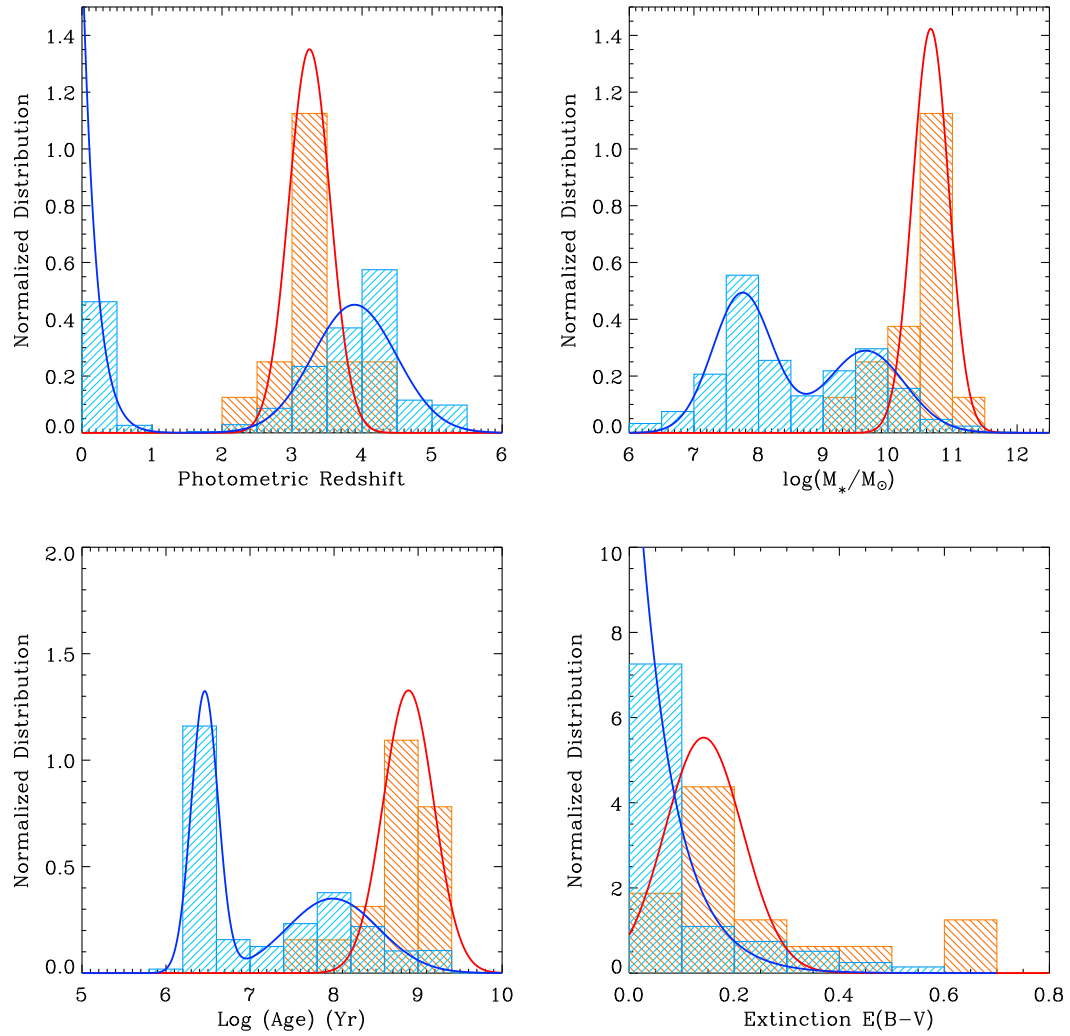


**Figure 3.12:** Distribution of the properties for the LBGs (blue) and BBGs (red) in the GOODS-S from the same photometric catalog. The distributions had been normalized. Both populations are selected in the same redshift range. From the distribution, we see that the BBG selection is targeting a more evolved and massive population than the LBG selection.

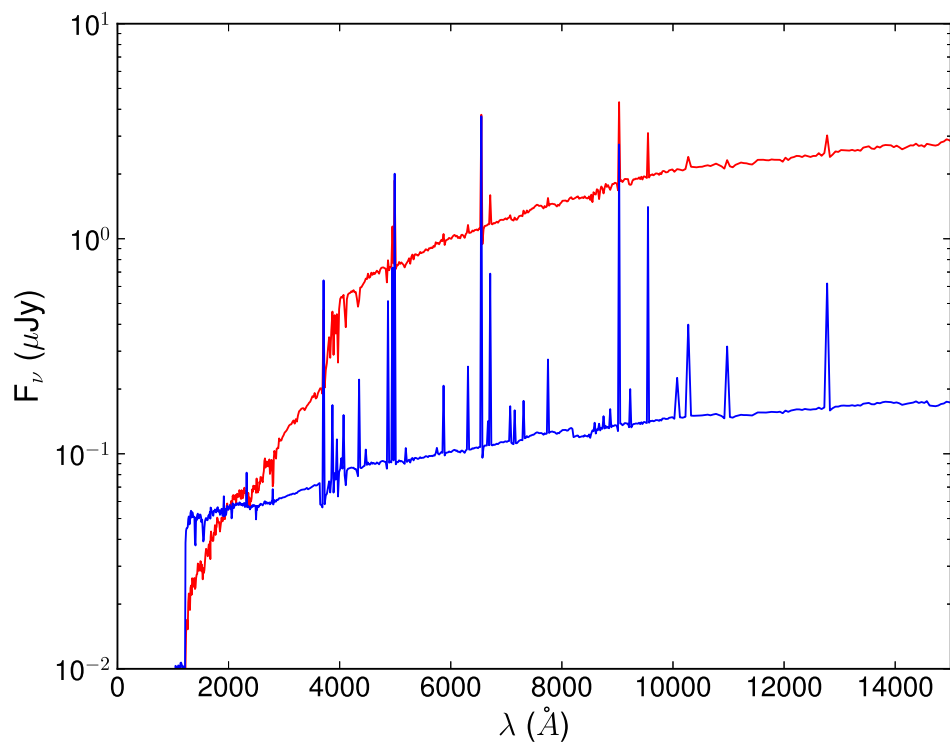


**Figure 3.13:** The stacked best-fit template SED of the BBG candidates (red) and the LBGs (blue) both normalized to the flux at 2000 Å. The LBGs are distinguishable from BBGs by having bright rest-frame UV and strong nebular emission lines.

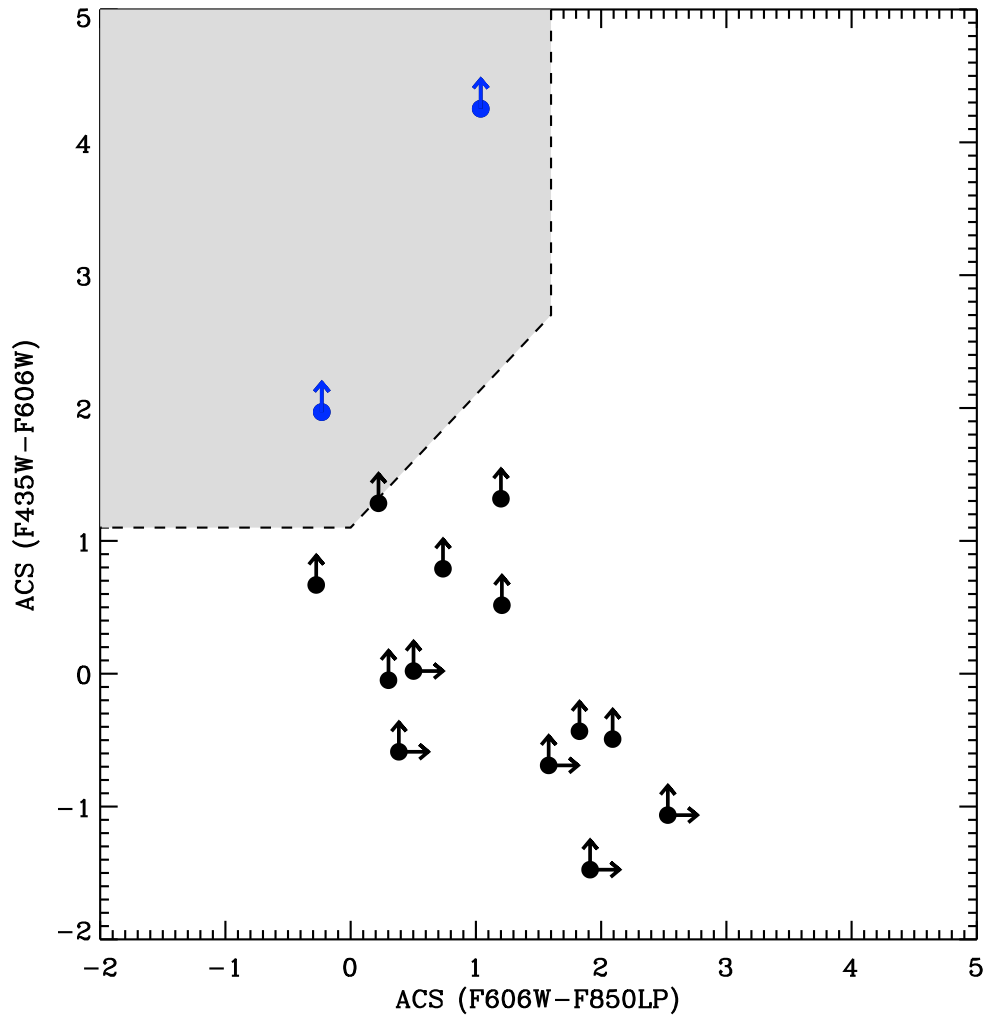


**Figure 3.14:** Optical color-color plot of LBG B drop out selection. The color selected BBG sources are plotted as black points and the color selected BBG sources that are also identified as an LBG are plotted as blue. The arrows represent  $2\sigma$  upper limits on the ACS bands for the optically faint BBGs. The B drop out selection criteria is identified as the shaded area.

LBG populations. The BBG selected galaxies have average mass of  $5 \times 10^{10} M_{\odot}$  and average age of  $\sim 800$  Myr (from the Gaussian fits to the distribution). The LBG selected galaxies on the other hand are less massive and have much younger ages. Kolmogorov–Smirnov test confirms that the LBG and BBG selected galaxies are drawn from statistically different populations with high confidence. This shows that the BBG selection criteria target more massive and evolved systems than the LBG selection. Using the SED inferred photometric redshifts to shift SEDs to the rest-frame, I stacked the best-fit SEDs of the BBG and LBG selected sources. Figure 3.13 shows the stacked rest-frame best fitted template SED of the BBG and LBG sources. The LBG selected star forming systems are bright in the rest-frame UV and are characterized by the prominent Lyman break and strong emission lines while the BBG selected quiescing systems are relatively faint in the UV and are distinguished by the break at  $\sim 4000\text{\AA}$  as we see from Figure 3.13.

Figure 3.14 shows the distribution of the BBGs on the color-color diagram used to identify LBGs (from Stark et al., 2009). Also shown is the LBG locus as the grey region. Two of our color selected BBGs also satisfy LBG selection criteria (the blue filled circles in Figure 3.14). The two BBG selected sources that are also selected as an LBG have high estimated star formation rates and extinction suggesting that these are the dusty star-forming galaxies and likely contaminants. One of these sources (ID #9286) has a MIPS counterpart indicative of a dusty galaxy and the other (ID #18694) has an X-ray source associated with it, which could be an AGN. The overlap with the LBG selection is mainly due to the fact that post-starburst galaxies are in the phase of passive evolution but they still can have residual star formation present, resulting in the dual selection. The quiescent galaxies are relatively faint in the rest-frame UV (observed optical U and B bands in the redshift of interest here) as their stellar population is dominated by cooler and older stars. The BBG candidates were selected to be faint (non-detected) in the VLT/VIMOS U and HST/ACS F435W (Section 3). Candidates that have less than  $2\sigma$  detections in the optical bands are shown with upper limit arrows in Figure 3.14.

### 3.7 Discussion

Two of the widely used methods for identifying high redshift galaxies are narrow-band selection technique where line emitting galaxies at given redshift slices are selected and the LBG selection which primarily selects UV bright objects. Both techniques select actively star-forming systems and are biased against old and quiescent galaxies at high redshifts. The BBG selection technique is developed to allow for selection of these galaxies, which are missed by other techniques. Study of the nature of the BBGs would constrain star formation efficiency and mass assembly at high redshifts.

In this study I developed the criteria to identify BBGs at  $3 < z < 4.5$ . Several recent studies (Bell et al., 2004; Brammer et al., 2011; Ilbert et al., 2013) have confirmed that the red sequence had already been in place by  $z \sim 1$ , that there is a significant fraction of high mass quiescent galaxies at  $z \sim 2 - 3$  (Kriek et al., 2008; Brammer et al., 2011; Marchesini et al., 2010; Whitaker et al., 2010) and support the presence of passively evolving galaxies at  $z \sim 3 - 4$  (Muzzin et al., 2013; Stefanon et al., 2013). Furthermore, using medium band observations from ZFOURGE<sup>2</sup>, Straatman et al., 2014 and Spitler et al., 2014 identified populations of optically faint, massive and quiescent galaxies at  $z \sim 4$ . These studies show that although there are relatively fewer of these systems compared to the star forming galaxies at the same redshift, they still make significant contribution to the global stellar mass density of the Universe.

The most massive BBGs ( $> 10^{10} M_{\odot}$ ) in our sample have an observed number density of  $\sim 3.2 \times 10^{-5} \text{ Mpc}^{-3}$  corresponding to a stellar mass density of  $\sim 2.0 \times 10^6 M_{\odot}/\text{Mpc}^3$  at  $3.0 < z < 4.5$  compared to the BBGs with no MIPS 24 micron detection which show an observed number density and mass density of  $\sim 2.5 \times 10^{-5} \text{ Mpc}^{-3}$  and  $10^6 M_{\odot}/\text{Mpc}^3$  respectively, consistent with ZFOURGE study. The BBG selection is specifically developed to minimize the contamination from dusty star forming galaxies. As discussed in Section 3.1, all the UVJ selected sources at  $z \sim 4$  by Straatman et al., 2014 fall in the BBG selection criteria although not all of them are selected as BBG candidates because of the additional

---

<sup>2</sup><http://zfourge.tamu.edu>

non-detection condition in the observed U and  $B_{435}$  bands (which probe the rest-frame UV at these redshifts). On the other hand most of the BBG selected sources at  $z \sim 3 - 4$  fall close to the dusty star forming and quiescent boundary condition in the UVJ diagram further confirming the complications involved in distinguishing the two populations on the UVJ plane with broad band photometry at  $z > 3$ .

The high redshift star forming galaxies are mostly selected through the LBG selection (Madau et al., 1996; Steidel et al., 1999, 2003; Stark et al., 2009) and the narrow band selection targeting the Ly- $\alpha$  line (Kunth et al., 1998; Shapley et al., 2006; Gronwall et al., 2007). Given the passive nature of the quiescent systems, they lack the strong emission to be targeted by the narrow band selection and they lack the strong UV continuum to be targeted by LBG selection. Using rest-frame UV luminosity function (Reddy et al., 2008; Reddy and Steidel, 2009; Bouwens et al., 2007, 2014), I estimated an observed number density of  $\sim 4 - 5 \times 10^{-3} \text{ Mpc}^{-3}$  for the star forming galaxies at  $z \sim 3 - 4$  (down to  $L_{lim} = 0.04 L_{z=3}^*$ ), indicating that the relatively passive galaxies at  $z \sim 3 - 4$  (identified from BBG selections) are less than 10% as numerous as the star forming systems at similar redshifts.

The mass function of galaxies has been studied extensively over the past few years out to  $z \sim 4 - 5$ , for both the star forming and quiescent galaxies (Dickinson et al., 2003; Fontana et al., 2006; Rudnick et al., 2006; Elsner et al., 2008; Pérez-González et al., 2008; Ilbert et al., 2013; Muzzin et al., 2013). Using a Spitzer IRAC selected sample Pérez-González et al., 2008 estimated the stellar mass function of galaxies and calculated the global stellar mass density of  $\sim 2.7 \times 10^7 M_{\odot}/\text{Mpc}^3$  at  $3.0 < z < 3.5$ . In more recent studies, Marchesini et al., 2010 and Muzzin et al., 2013 estimated the stellar mass function of galaxies out to  $z \sim 4$ , using near infrared selected sample of galaxies. These studies estimate a stellar mass density of  $\sim 4 \times 10^6 M_{\odot}/\text{Mpc}^3$  in  $3.0 < z < 4.0$  for the most massive ( $> 10^{10} M_{\odot}$ ) systems. Given the uncertainties inherent in the global stellar mass functions and corresponding mass densities at these redshifts, the BBG selected passive candidates could contribute as much as 10-40% to the stellar mass density of the Universe at  $z \sim 3 - 4$ .

With an average age of  $\sim 800$  Myr, the BBGs are expected to have formed the bulk of their mass in a burst of star formation at much higher redshifts and have been living a relatively quiescent life ever since ( $z \sim 6$ ; Mobasher et al., 2005; Wiklind et al., 2008; Straatman et al., 2014; Toft et al., 2014). Assuming a constant star formation history, these massive galaxies must have assembled their mass with star formation rates  $\sim 50 - 100 M_{\odot} yr^{-1}$ . With a bursty star formation history, which is more favored for these systems as supported by the strength of the Balmer break and the passive evolution, the progenitors of these systems must be forming stars well in excess of  $100 M_{\odot} yr^{-1}$ . Recent works indicate young and highly star forming Lyman- $\alpha$  emitting systems at  $z \sim 6 - 7$  identified through narrow band detections with star formation rates as high as few hundred  $M_{\odot}/yr$  (Shimasaku et al., 2006; Ouchi et al., 2010; Mallery et al., 2012; Ono et al., 2012). Although these systems could potentially be the progenitors of the quenching systems that I identify at  $z \sim 4$ , their predicted number density is very small (Straatman et al., 2014). Recent studies have indicated the presence of very highly star forming galaxies at high redshift identified as dusty star forming galaxies detected in the far infrared and sub-millimeter wavelengths (Younger et al., 2007, 2009; Magnelli et al., 2012; Karim et al., 2013). These sub-millimeter galaxies (SMGs) are among the most star forming systems with SFRs  $\gtrsim 1000 M_{\odot} Yr^{-1}$  (Capak et al., 2008; Fu et al., 2013). The intense star formation is believed to be the result of gas rich major mergers (Tacconi et al., 2008; Ivison et al., 2012; Fu et al., 2013). Based on a  $870 \mu m$  selected sample of sub-millimeter selected galaxies, Toft et al., 2014 showed that these systems could be the progenitors of the quiescent galaxies found at  $z \sim 2$ . By studying the number density of quiescent systems at  $z \sim 4$ , Straatman et al., 2014 showed that the high redshift SMGs might have the right number density to be the progenitors of these systems. Given the similar number densities for the BBGs in the same redshift range and assuming a relatively short formation time scale for these systems ( $\sim 200$  Myr, as supported by the bursty models; Straatman et al., 2014) I see that the BBG selected passive systems could be the descendants of the intensely star forming sub-millimeter galaxies at  $z \gtrsim 5 - 6$ .

At  $z \sim 3$ , the most massive BBG candidates ( $M_\star > 10^{10} M_\odot$ ) will be residing in host Dark Matter Halos (DMHs) of  $M_h \sim 10^{12} M_\odot$  ( $M_\star/M_h \sim 0.01$ ) according to semi analytic models (Behroozi et al., 2013). These systems could potentially constrain the hierarchical galaxy formation scenarios (the  $\Lambda$ -CDM models), if their number density exceeds the DMH number density required to host them at their redshifts (Wiklind et al., 2008). The observed number density of the BBGs is approximately 2 dex smaller than the predicted DMHs at these redshifts ( $\sim 3 \times 10^{-3} Mpc^{-3}$ ; Mo and White, 2002; Behroozi et al., 2013). This indicates that the formation of these systems is acceptable within the hierarchical scenarios of galaxy formation although the exact mechanism of rapid mass growth is still controversial. Whether these galaxies formed their mass monolithically in these very massive halos at high redshift through constant gas accretion or through sequential merging, the physical process of this assembly is still controversial. A test of this would be to search for BBGs at higher redshifts (Wiklind et al., 2008). A large number density for the BBGs at  $z \sim 5-7$  favors the monolithic collapse hypothesis as galaxies at those redshifts ( $\sim 1$  Gyr after the Big Bang) have not had enough time to go through the mergers process and to consume all their gas making stars (Mobasher et al., 2005; Wiklind et al., 2008).

**Table 3.2:** List of the color-selected BBG candidates in the CANDELS GOODS-S.

ID <sup>a</sup>	RA	DEC	Phot-Z	log(Mass) ( $M_{\odot}$ )	E(B-V)	log(Age) (Gyr)	SFR ( $M_{\odot}Yr^{-1}$ )	F160W	(H-K <sub>s</sub> )	MIPS	X-ray
2782	53.0835712	-27.8875292	3.28	10.8	0.19	8.70	0.8	24.9	1.47	N	N
4356	53.1465968	-27.8709872	3.88	11.1	0.69	8.86	261.2	26.3	1.56	Y	Y
4624	53.1379933	-27.8682475	3.10	10.7	0.29	8.71	5.6	25.4	1.36	N	Y
6189	53.2057581	-27.8521496	4.00	9.72	0.00	8.26	0.0	26.3	1.33	N	N
7526	53.0786782	-27.8395462	4.48	10.6	0.04	8.71	0.5	25.9	1.55	N	N
9177	53.0383219	-27.8252681	2.42	10.4	0.69	8.71	75.8	25.2	1.27	N	N
9286	53.2243550	-27.8243357	3.27	10.7	0.39	9.23	31.8	25.6	1.24	Y	N
10479	53.1974865	-27.8140435	3.91	10.5	0.19	9.16	9.1	26.4	1.45	Y	N
12178	53.0392836	-27.7993085	3.22	10.6	0.04	9.16	1.8	25.1	1.28	N	N
12360	53.2194525	-27.7979791	2.93	10.1	0.14	9.16	0.5	26.4	1.19	N	N
13327	53.1304511	-27.7911228	3.38	10.1	0.19	8.26	2.7	25.6	1.18	N	Y
16671	53.1901828	-27.7691400	2.69	10.8	0.19	9.36	2.1	24.8	1.20	N	N
17749	53.1968943	-27.7604529	3.37	10.9	0.24	8.71	0.1	25.2	1.78	N	N
18180	53.1812226	-27.7564225	3.32	10.8	0.19	8.71	0.0	25.1	1.60	N	N
18694	53.0503542	-27.7521307	3.30	9.97	0.44	7.59	129.7	24.9	1.37	N	Y
19195	53.0643105	-27.7477684	3.20	9.37	0.19	7.96	4.8	26.0	1.78	N	N

<sup>a</sup>CANDELS GOODS-S TFIT WFC3  $H_{160}$  band selected catalog (Guo et al., 2013).

## Chapter 4

# Morphology of Passive Galaxies at

$$z > 3$$

### 4.1 Introduction

Understanding the evolution of galaxies with cosmic time is one of the most important questions in observational astronomy. According to the current evolutionary models, galaxies form in the most gas rich environments and grow in mass by gas accretion with the help of the gravitational potential of their host dark matter halos or sequential merging with other galaxies or both (White and Frenk, 1991; Lacey and Cole, 1993; Bundy et al., 2009; Fakhouri et al., 2010).

In the local Universe the most massive systems are the quenched elliptical galaxies (De Lucia and Blaizot, 2007). These are among the largest systems in size with nearly featureless morphologies with very little or no ongoing star formations. Galaxies become bluer as we go to higher redshifts with increasing star formation rates that match the increase in the cosmic star formation density (Madau et al., 1998; Hopkins and Beacom, 2006; Behroozi et al., 2013). These high redshift blue galaxies could turn into the very massive elliptical galaxies that we observe in the local Universe (Barro et al., 2013, 2014). There are several theories that explain the quenching of star formation in the young blue galaxies with the

supernova and AGN feedback from the death of the most massive stars and the central supermassive black hole playing the most important roles (Martig et al., 2009; Bell et al., 2012).

There are several studies that indicate the presence of massive evolved systems at high redshifts. Ilbert et al., 2013 showed that the red sequence of galaxies is already in place at  $z \sim 2$  and Mobasher et al., 2005; Wiklind et al., 2008 found evidence of the presence of these systems at  $z \gtrsim 3$ . Several recent studies show that the massive quiescent galaxies at  $z \sim 2$  are much smaller than their local counterparts with half light radii of only a few kpc (van Dokkum et al., 2008). These galaxies are usually classified as the Compact Quiescent Galaxies (CQGs) or red nuggets and are believed to be formed from quenching of star formation through feedback process by the compact star forming galaxies (Barro et al., 2013; Williams et al., 2014b). How these CQGs grow in size with constant mass to become the big elliptical galaxies in the local Universe is still poorly understood although minor mergers are believed to play an important role in the evolution (Newman et al., 2012).

In this work I use very deep observations by the HST/WFC3 in the near infrared to study the size evolution of different types of galaxies at high redshifts. The high resolution observations by the WFC3 at  $1.6 \mu\text{m}$  makes it possible to accurately measure the size of these systems. At  $z \sim 3 - 4$  the WFC3  $H_{160}$  probes the restframe optical bands of the galaxies which is more sensitive to the older general underlying stellar population of the galaxy and not the UV bright regions (blubs) caused by recent star formations, giving a better picture of the shape of the galaxy.

I use GALFIT(Peng et al., 2002) to fit a Sersic function to the light profile of star-forming and passive galaxies identified from deep HST/ACS and WFC3 observations by the CANDELS in the GOODS-S field at  $z \sim 3 - 4$ . From this fit I measure light profile and the half light radius of the galaxy as a measurement of size. The multi-waveband photometry in the field allows us to estimate the physical properties of the galaxy very accurately. I use the estimated photometric redshifts from the model fits to explore the size evolution for passive galaxies at  $z \gtrsim 3$ . Using the estimated stellar mass of the galaxies I

explore the mass-size relation for LBG and BBG selected galaxies and find that the star forming galaxies are on average 2-3 times larger than the corresponding passive galaxies.

In Section 2 I will discuss our sample and data used in this study. I will discuss our results of the size measurement of the star forming and quiescent galaxies in Section 3. Here I will present these results in the form of mass-size relation and the size evolution for the two populations of galaxies. I summarize our results in Section 4.

## 4.2 Sample and Data

The galaxies used in this study are star-forming and quiescent systems identified by the LBG and BBG selections as discussed in Chapter 2. In order to avoid a sample bias in the measurements, I selected the LBG sample using the same photometry as the BBGs by identifying bdrop-out galaxies in the GOODS-S Deep area.

I use CANDELS HST/WFC3 observations of the GOODS-S field, in particular the data in the F160W band (H-band), to measure galaxy sizes. At the redshift of study here the observed H-band corresponds to the restframe optical and is sensitive to the more evolved population of galaxies which form the galaxy. This would also help us to avoid the clumpy UV bright star-forming regions of the galaxy which could affect size measurement accuracy and which are more affected by dust.

The CANDELS WFC3 F160w observations of the GOODS-S cover an area of  $10' \times 16'$  in the Early Release Science (ERS), wide and deep sections (Grogin et al., 2011) with varying depth. In order to avoid any biases that might enter the size measurements due to depth variability of the H-band observations, I focus on the GOODS-S Deep area. This is also the region that was used to select the old and massive galaxies in Chapter 3. The GOODS-S deep region consists of a rectangular grid of  $3 \times 5$  tiles ( $\sim 6'.5 \times 10'.8$ ). The H-band observations has a pixel resolution scale of  $0.06''$  and a  $5\sigma$  magnitude depth of 28.16 in 1 FWHM aperture.

### 4.3 Size Measurements of Passive Galaxies

To measure the size I fitted the light profile of the galaxy with a Sersic function in the form:

$$\ln I(R) = \ln I_0 - kR^{1/n} \quad (4.1)$$

I use the GALFIT software package (Peng et al., 2002) to fit the above light profile to the quiescent galaxy candidates discovered in Chapter 3. GALFIT finds the best fit 2D model to the light profile of the galaxy. The fitted values of the model are reported as the Sersic number ( $n$ ) and half light radius ( $R_e$ ) of the galaxy.

GALFIT requires the following input parameters: I. high resolution image II. high resolution point spread function III. high resolution rms map IV. bad pixel mask V. initial guess of the input parameter. I use the CANDELS HST/WFC3 F160W mosaic for the high resolution image and rms maps. To facilitate faster processing I created cutout images of  $200 \times 200$  pixels in size centered at the position of the candidates for each object from these maps. The PSF is made by stacking the spectra of the most isolated stars in the field. For the initial guess of the input parameters for the GALFIT I use the values reported by the Source Extractor.

In all but one of the candidates (#12178) the sources were fairly isolated and I only fitted a single Sersic function to the given galaxy. For #12178 I fitted both galaxies simultaneously with two Sersic functions centered on the individual objects. Figure 4.1 shows the HST F160W image for each galaxy along with the fitted models and residual maps (model subtracted image of the galaxy). As we see from Figure 4.1, the BBGs are relatively compact objects with most of the mass concentrated in a region a few kpc across. The BBG sample have median fitted Sersic parameter of  $n = 3.50$  from the fitted profile. This is consistent with a De Vaucouleur light profile ( $n=4$ ) found in the local early type galaxies. On the other hand the LBG sample has a median fitted Sersic parameter of  $n = 1.35$  consistent with a less concentrated light (or mass; considering a fix M/L ratio) profile. In this section I will discuss my results of the study of size evolution of quiescent galaxies.

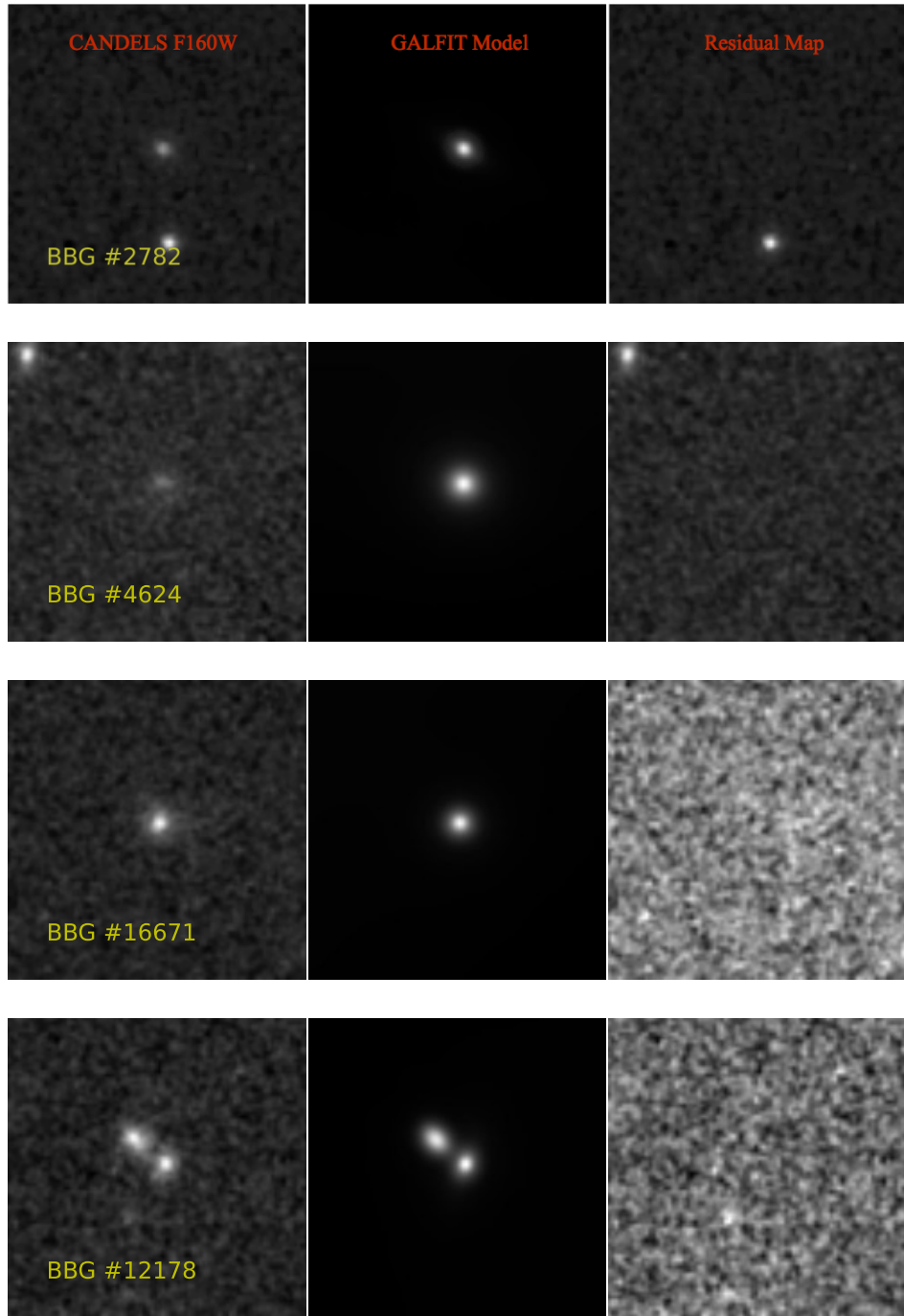


**Figure 4.1:** The CANDELS  $H_{F160}$  band cutouts of the BBGs (left), GALFIT models (middle) and residual maps (right). The models are generated by fitting a single Sersic function as described in section 5.3 (double Sersic for #12178). The residual maps are the model subtracted images of the galaxy. The galaxy cutouts are  $\sim 5'' \times 5''$  in size.

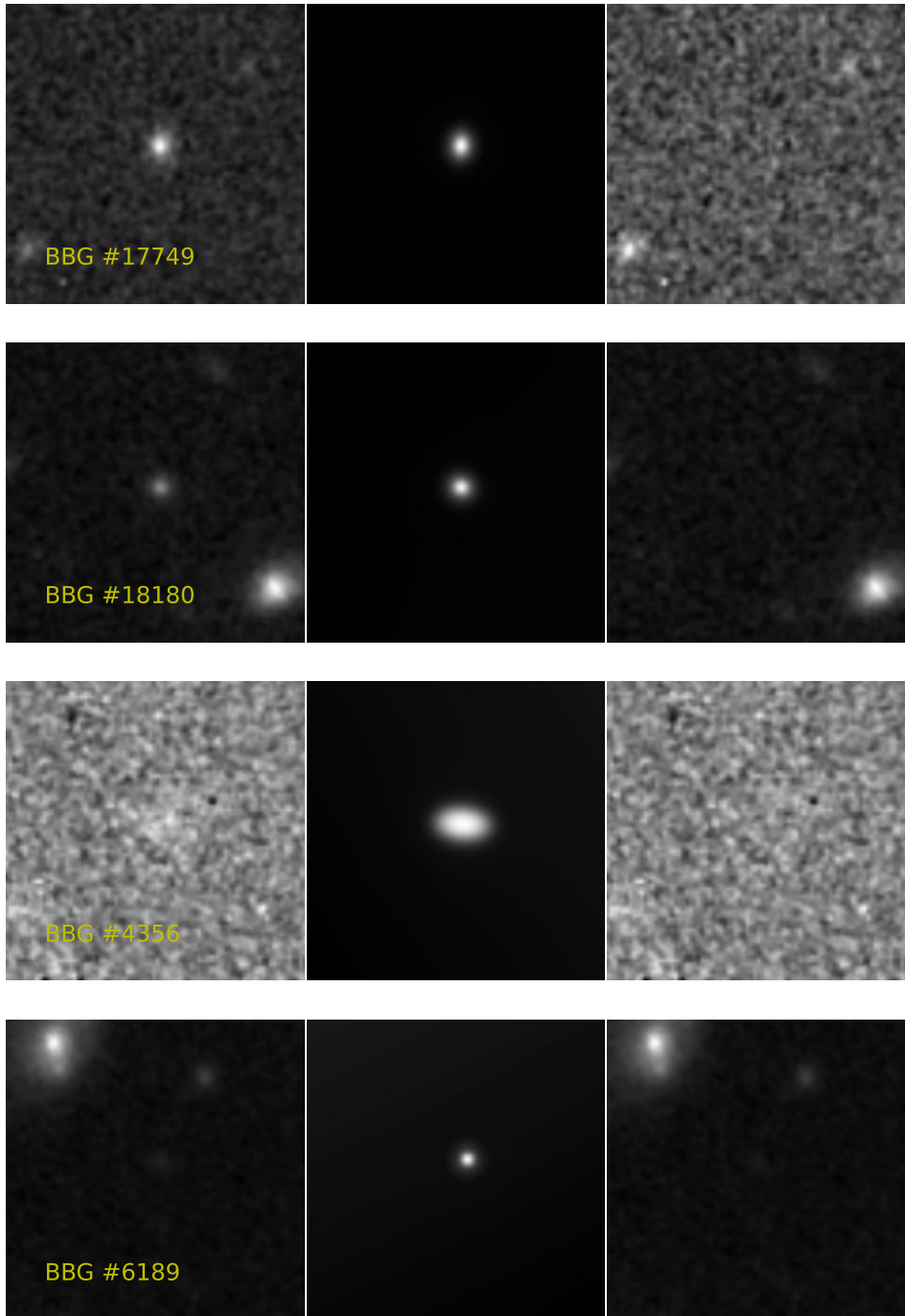


Figure 4.1: Continued.

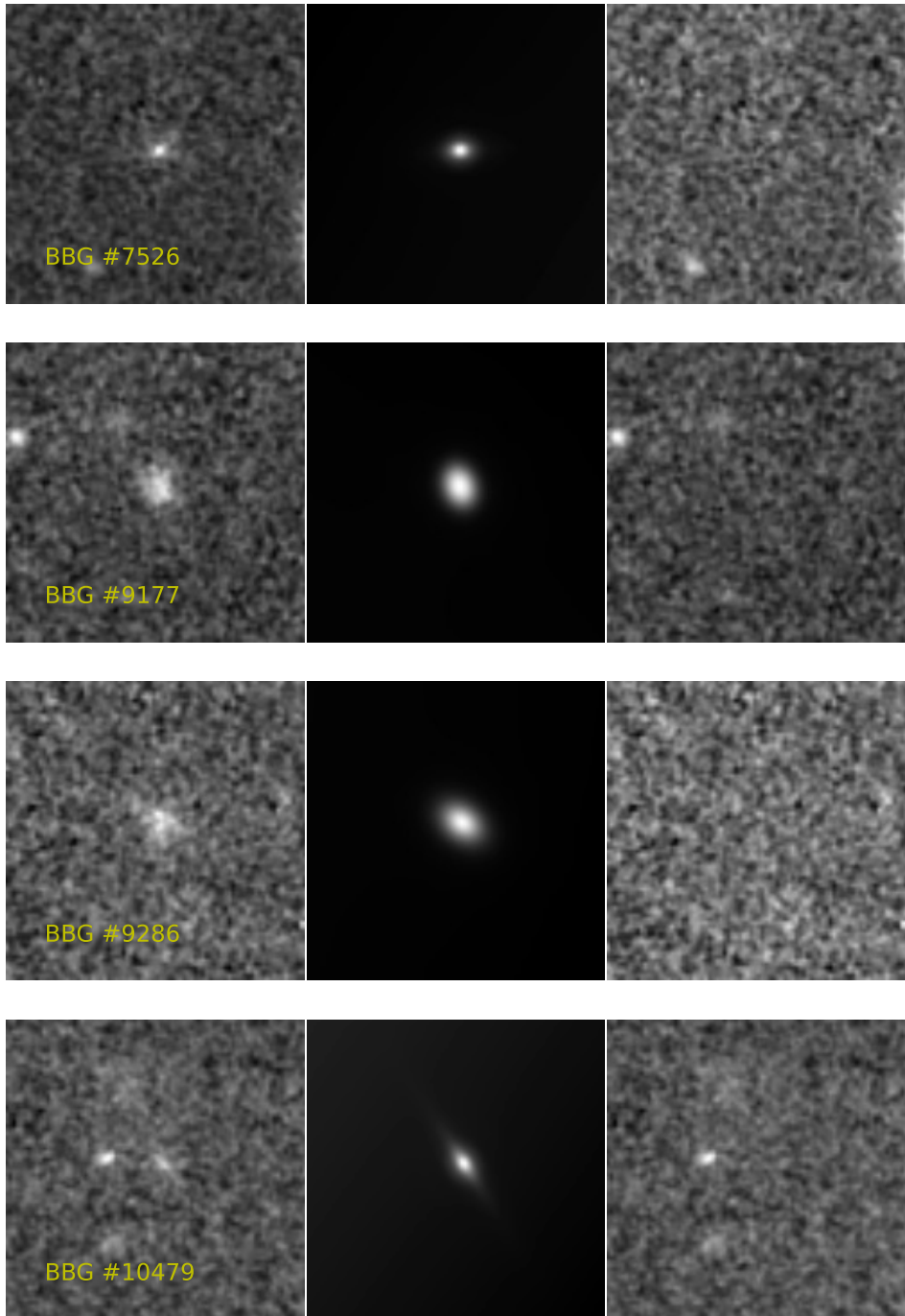


Figure 4.1: Continued.

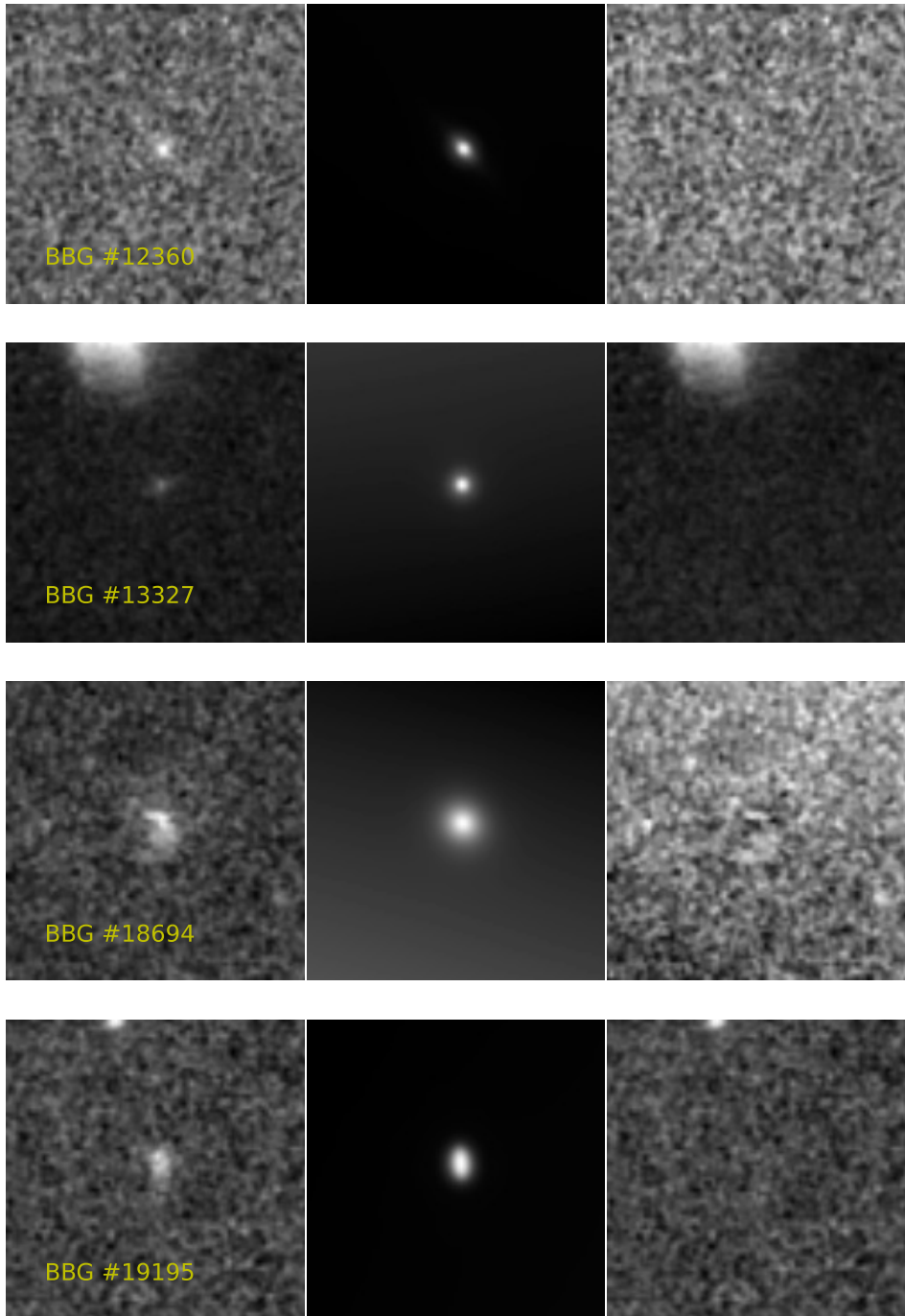


Figure 4.1: Continued.

**Table 4.1:** GALFIT best fit Sersic parameters for the BBGs.

Source ID	F160W (AB Mag)	$R_e$ (Pixel)	Physical Size (Kpc)	Sersic Index (best fit)	Axis Ratio	Position Angle (Degrees)
2782	24.94	0.0898	0.672	8.0	0.40	62.1
4356	26.39	0.396	2.789	0.7	0.73	-72.3
4624	25.43	0.345	2.637	2.7	0.99	70.7
6189	26.36	0.124	0.866	0.7	0.52	77.5
7526	25.98	0.115	0.765	5.2	0.31	-87.3
9177	25.24	0.225	1.835	0.5	0.69	19.5
9286	25.68	0.325	2.443	1.2	0.63	52.3
10479	26.47	0.086	0.605	3.5	0.98	50.2
12178	25.15	0.124	0.937	3.0	0.50	-16.5
12360	26.49	0.800	6.210	8.0	0.08	42.9
13327	25.61	5.519	40.918	8.0	0.62	-62.7
16671	24.87	0.418	3.323	7.3	0.82	82.3
17749	25.25	0.125	0.934	1.6	0.53	-5.3
18180	25.13	0.101	0.754	3.9	0.77	64.1
18694	24.93	2.321	17.353	4.9	0.75	5.3
19195	26.04	0.189	1.430	0.3	0.44	6.6

### 4.3.1 The Mass-Size Relation for Passive Galaxies

I use the GALFIT measured sizes to further study the mass-size relation in galaxies at  $z \gtrsim 3$ . Studies of local galaxies indicate that more massive galaxies are more extended. Using a large sample of late type star-forming and early type elliptical galaxies in the SDSS, Shen et al., 2003 explored their mass-size relation and showed that the size of both populations evolve as a function of the galaxy mass. The size evolution with mass is however different for star-forming from that of the quiescent galaxies with the latter having a steeper evolution with mass (Shen et al., 2003).

I converted the angular size to the physical size in Kilo parsec using the pixel scale of the HST F160W band and  $dr = d_L d\theta$  relation with  $d_L$  being the luminosity distance at the redshift of the galaxy. The mass measured for each galaxy is from fitting the observed photometry to a library of model SEDs as described in Chapter 3. Figure 4.2 shows the mass-size plot for star forming (LBG selected) and quiescent galaxies (BBG selected) in the CANDELS GOODS-S. The star forming galaxies are binned in mass and I report the

median values of the size and mass for the LBG sample in each bin. I show the local relation for elliptical galaxies from Shen et al., 2003 in Figure 4.2 as the dashed line. I see that the BBG selected passive systems (red points) are generally more compact than their local counterparts and fall below the local relation in the mass-size plot. This further confirms our original argument that the most massive and old systems at high redshift are also very compact with half light radii of only a few kpc. This is in agreement with recent studies at slightly lower redshifts (Barro et al., 2013; van der Wel et al., 2014). The mass-size relation in van der Wel et al., 2014 is reported as  $R_e/\text{kpc} = A(M_*/5 \times 10^{10} M_\odot)^\alpha$  where A and  $\alpha$  are simultaneously fitted to the data. Fitting the same function to the most massive BBGs ( $> 10^{10}$ ) in the size-mass plot I get a relation which is slightly steeper than the one reported by van der Wel et al., 2014 for quiescent galaxies at  $z \sim 2.75$ . This is in agreement with the general trend that we see in the slope evolution of the size-mass relation for early type galaxies from  $z = 0 - 3$  (van der Wel et al., 2014). Because of the limited number of sources used in the fit and the large error bars of some of these sources I do not report and plot these values as they are not to be trusted. As we see in Figure 4.2, the size of the blue star-forming galaxies show a flatter evolution with mass. This is in agreement with the general trend of the decrease in the slope of the relation for star-forming galaxies from measurements at slightly lower redshifts (van der Wel et al., 2014) as shown with the dashed-dotted line in Figure 4.2.

### 4.3.2 Size Evolution of Massive Galaxies with Redshift

I explore the size evolution of the massive and old galaxies measured from the deep HST/WFC3 observations. I study this evolution for the most massive ( $> 10^{10} M_\star$ ) MIPS non-detected BBGs in the CANDELS GOODS-S Deep area. As discussed in Chapter 3 the MIPS detection in the far infrared SED of the BBGs at this redshift could indicate the presence of dusty populations.

Figure 4.3 shows the size evolution of star-forming and quiescent galaxies out to  $z \gtrsim 3$ . The size evolution for the star-forming systems is from a spectroscopic sample of UV bright

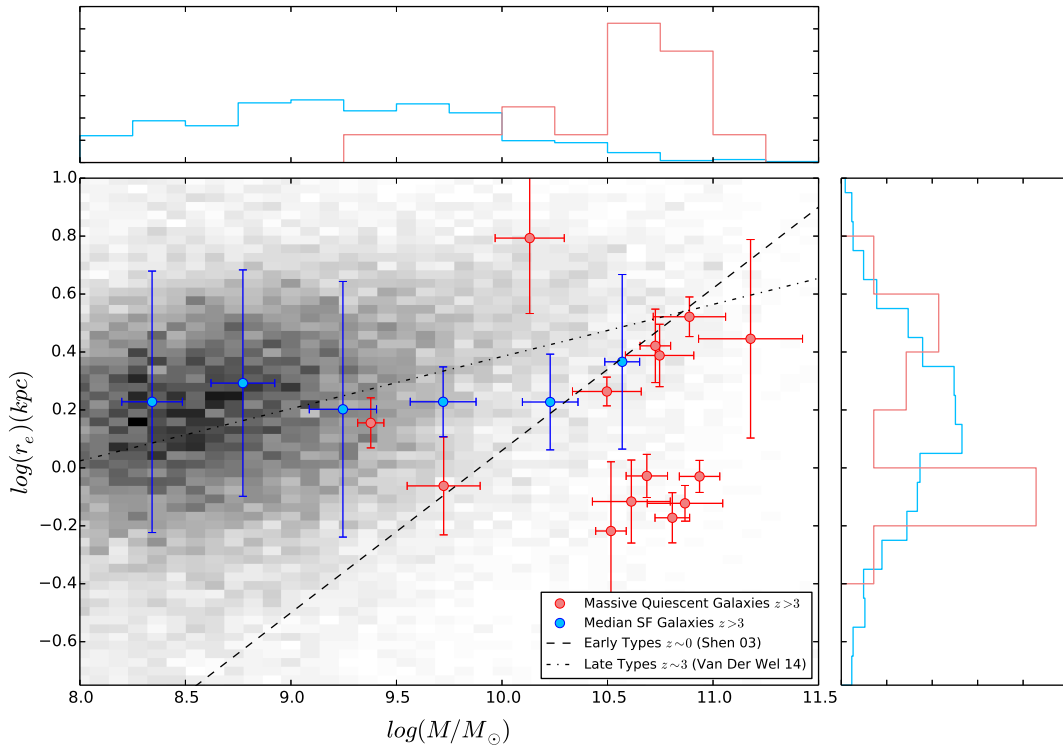
galaxies by Mosleh et al., 2011. The measurements for quiescent galaxies at  $z \sim 2.2$  is from work by van Dokkum et al., 2008. For the quiescent sample I report the median values of the redshift and physical size of the galaxy. The reported error bar is the standard deviation of the sample. I fit a function in the form of  $R_e = \alpha(1+z)^{-\beta}$  to the quiescent galaxy data taking into account the errors. This yields  $\alpha = 5.68$  and  $\beta = 1.48$  for the size evolution relation for the quiescent galaxies out to  $z \gtrsim 3$ .

Figure 4.3 shows that the size of the early type galaxies decrease as a function of redshift and they become more compact at  $z \gtrsim 3$ . This is in agreement with recent works by Newman2012, Vanderwel2014 that show similar trends in the size evolution of quiescent galaxies out to  $z \sim 2.5$ . Looking at the size evolution of star-forming and quiescent systems in Figure 4.3 I note that at any given redshift on average the quiescent galaxies are 2-3 times more compact than the LBG selected star-forming galaxies.

## 4.4 Discussion

The size evolution of different populations of galaxies had been studied extensively over the past few years (van Dokkum et al., 2008; Mosleh et al., 2011; Newman et al., 2012; van der Wel et al., 2014). The size of the galaxies have been shown to not only depend on their mass and type but also on the redshift observed (van der Wel et al., 2014). Populations of star-forming and quiescent galaxies get more compact at higher redshifts (van der Wel et al., 2014) and this has been shown by recent studies to be an intrinsic property of the observed galaxies and is not associated with systematic errors in modeling (Davari et al., 2014). I use GALFIT (Peng et al., 2002) to fit a single Sersic function to the light profile of galaxies and to measure the size. This has been shown in recent simulations of high redshift massive and compact galaxies to accurately measure the size of these systems over a wide range of signal to noise without bias (Davari et al., 2014).

In this work I used a sample of old and massive galaxies at  $z \gtrsim 3$ , selected from deep HST near-IR observations, to study the mass-size relation and size evolution of galaxies at



**Figure 4.2:** The size-mass evolution of star-forming and quiescent galaxies in the CANDELS GOODS-S at  $z \gtrsim 3$ . The old and massive BBG sources are shown in red and the star-forming LBG sources are plotted in blue. The LBGs are binned in mass and each point represents the median in each bin. The dashed line corresponds to the size-mass relation for local early type galaxies in the SDSS by (Shen et al., 2003). I see that the BBGs are generally more compact than the local relation. The dashed-dotted line shows the size-mass relation for the late type star-forming galaxies by (van der Wel et al., 2014) at  $z \sim 2.5$ . The subplots show the distribution of mass and size for the two populations.

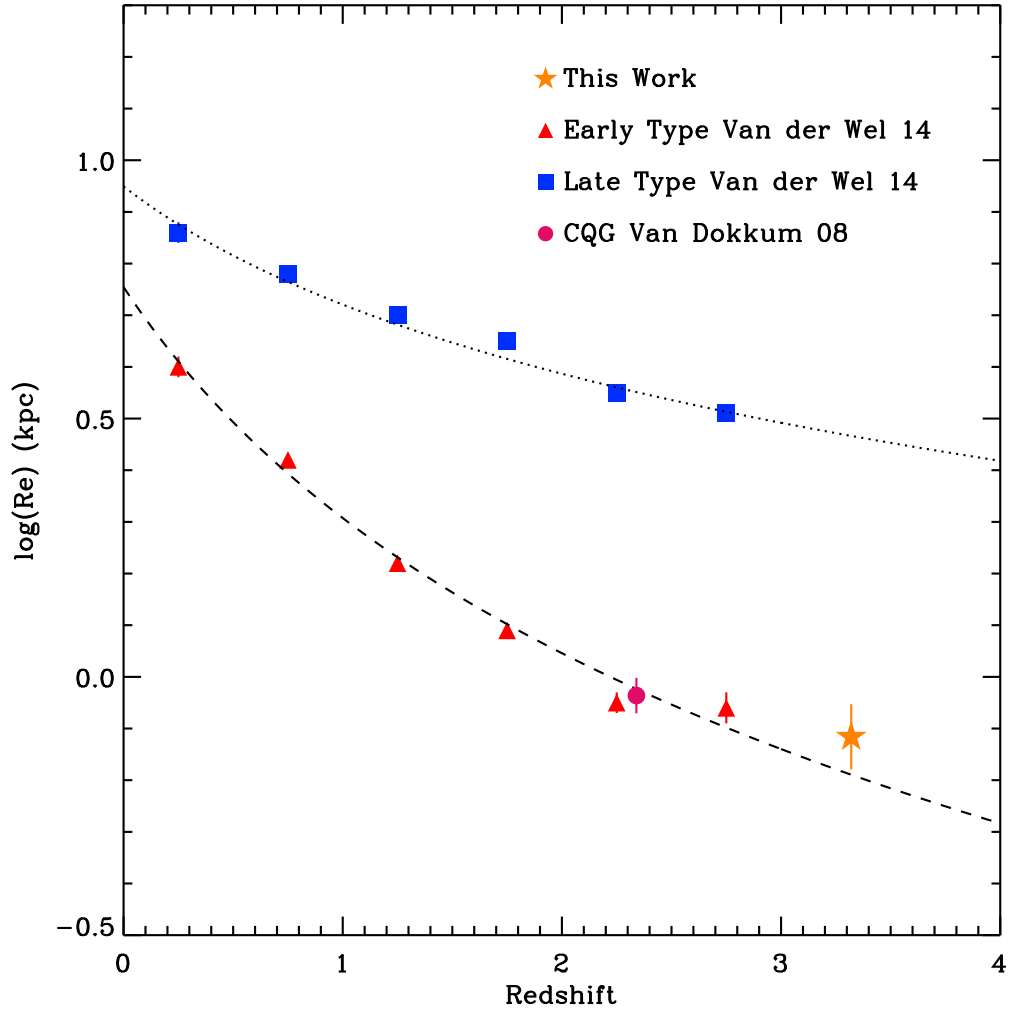


**Figure 4.3:** The size evolution relation for passive (red triangle) and star-forming galaxies (blue square). The star-forming galaxies LBG and GALEX selected UV bright systems (Mosleh et al., 2011) and the low redshift quiescent galaxies is a from a sample by van Dokkum et al., 2008. The quiescent galaxy size is reported as the median size of the most massive non-MIPS detected BBG galaxies at the median redshift of the sample and is shown by the yellow star. The size-redshift relation for the quiescent galaxies is given by  $R_e \propto (1+z)^{-1.48}$  and is shown by the dashed line.

high redshifts. I find that the most massive old galaxies at  $z \gtrsim 3$  are much more compact than early type galaxies of similar mass in the local Universe. Recent studies show that the physical size of the quiescent galaxies has a much steeper evolution with mass than the star-forming galaxies at the same redshift (Newman et al., 2012; van der Wel et al., 2014). Using CANDELS and 3D-HST data van der Wel et al., 2014 studied the size-mass relation for star-forming and quiescent galaxies and found  $R_{eff} \propto M_{\star}^{0.22}$  and  $R_{eff} \propto M_{\star}^{0.75}$  respectively for the two populations. Using the high redshift sample of quiescent galaxies, I demonstrated that there is a rapid evolution in size for massive quiescent galaxies to high redshift. The mass-size relation seems to have a steeper evolution for quiescent galaxies compared to the early type relations at lower redshift as demonstrated in Figure 4.2. I also see in this plot that the physical size of the LBG selected star-forming galaxies in the GOODS-S have a flatter dependence on mass at  $z \gtrsim 3$ . These are in agreement with the trends seen in van der Wel et al., 2014 for the star-forming and quiescent populations at  $z \lesssim 3$ . The small sample size of the high redshift quiescent galaxies, however, does not allow us to quantify these results any further.

Recent attempts in studying the size evolution of quiescent galaxies out to  $z \sim 2.75$  have confirmed the rapid decrease in size as a function of redshift (van der Wel et al., 2014). These studies estimate that the most massive quiescent galaxies ( $M_{\star} > 5 \times 10^{10}$ ) have physical sizes of 0.87 kpc at  $z \sim 2.75$  (van der Wel et al., 2014). In particular van Dokkum et al., 2008 used HST images to look at a population of quiescent galaxies and found that these massive systems have estimated sizes of  $\sim 0.9$  kpc on average. The most massive MIPS non-detected BBGs in the GOODS-S have estimated median effective radius of  $R_e = 0.8$  kpc at  $z \sim 3.5$ . This is in agreement with the rapid decrease in size with redshift trend seen for the massive quiescent galaxies. From Figure 4.3 we notice that the change in size for the quiescent galaxies seems to be plateauing at  $z \gtrsim 2.5$ . I see that galaxy size drop very moderately beyond this redshift although a quantitative statement cannot be made given the small sample size and the errors involved in physical size measurements for these high redshift galaxies. Adding the measured size value for the BBGs at  $z \sim 3.5$

to the size evolution and fitting this as a function of the scale factor, we would arrive at  $R_e = 5.68(1 + z)^{-1.48}$  which is similar to the relation reported by van der Wel et al., 2014.

## Chapter 5

# Spectroscopic Study of Passive Galaxies at $z > 3$

### 5.1 Introduction

According to the standard picture of galaxy formation (the cold dark matter scenarios, ie.  $\Lambda$ -CDM models), baryonic matter is gravitationally accreted in Dark Matter Halos (DMHs) providing the seed for galaxy formation (Navarro et al., 1996; Sheth et al., 2001; Reed et al., 2003). In these scenarios galaxies become ever more massive through a sequential merging process in more recent time such that most of the local stellar mass density of the Universe is locked in these very massive early type galaxies (Ilbert et al., 2013).

Many studies indicate the presence of a population of passively evolving systems at redshifts as high as  $z \sim 2 - 3$  (Labbé et al., 2005; Kriek et al., 2008). These systems lack the bright rest-frame UV continuum characteristic of star forming galaxies and are usually identified by their near-IR and infrared colors through very deep observations by the largest ground-based telescopes combined with HST and Spitzer observations. Due to their passive nature, these systems usually lack the characteristic strong emission features that are used to identify the star forming systems at high redshift. Using extremely long integration times with the Gemini near-IR spectrograph Kriek et al., 2009 spectroscopically confirmed

a quiescent galaxy at  $z=2.2$ . There they showed that the object is characterized by the optical absorption features that represent passively evolving galaxies and they measured SED inferred SFRs that were consistent with being a quiescent system. In a recent study Belli et al., 2014b used KECK/MOSFIRE rest-frame optical spectroscopy of a sample of massive galaxies at  $2 < z < 3$  and showed that their spectral and SED inferred properties are consistent with being passively evolving systems at these redshifts.

Recently there has been several studies that point to the existence of relatively quiescent systems at higher redshifts (Mobasher et al., 2005; Wiklind et al., 2008; Straatman et al., 2014; Spitler et al., 2014). These studies use very deep infrared observations by the HST/WFC3 and other ground-based observatories to look for quenching galaxies. From these I see that there is growing evidence of the presence of massive and evolved galaxies at  $z \sim 3 - 4$  that are hypothesized to be the descendants of the most star forming galaxies found at  $z > 5$  by far infrared and sub millimeter surveys (Toft et al., 2014; Straatman et al., 2014). These rest-frame UV faint infrared selected relatively quiescent systems usually lack the bright emission features that are characteristic of star forming systems.

In this work I use very deep Keck/DEIMOS observations of a sample of quiescent and star forming galaxies at high redshifts. The candidates are selected from the deepest optical, near infrared HST/WFC3 and ground based observations in these fields along with very deep Spitzer observations in the infrared. I look at the spectroscopic properties of the two populations and in particular try to explore the interstellar medium of these systems by looking at absorption (and/or emission) features in the observed stacked spectra of these systems. The most widely accepted picture for star forming galaxies at high redshift predict that the restframe UV spectra of these systems generally exhibit signatures of outflowing material of different velocities. These outflow velocities have been shown to be correlated with the SFR and mass of the galaxies in general. In this Chapter I aim to further study these trends and more specifically to compare it with the spectroscopic properties of relatively quiescent systems.

This Chapter is structured as follows. In Section 2 I discuss the spectroscopic data

and the candidates used for the spectroscopic observations. I discuss the spectroscopic data reduction, redshift assignment and analysis in Section 3. I report our results of the measurements of the spectroscopic properties of star forming and quiescent galaxies in 4 and discuss our results in Section 5.

## 5.2 Spectroscopic Candidates and Data

The candidates targeted for spectroscopy are from samples of star forming and passively evolving systems at  $z > 3$ . The star forming candidates are Lyman- $\alpha$  emitting systems (Lyman Alpha Emitters or LAEs) identified from narrow band imaging or Lyman Break Galaxies (LBGs) identified from the drop-out technique. The quiescent massive systems are identified from their near infrared colors and Spitzer IRAC detection based on the criteria developed in Chapter 2. In this section I will discuss the sample in more detail.

### 5.2.1 Passive Candidates

The relatively quiescent systems are selected based on the strength of their Balmer break as Balmer Break Galaxies (BBGs) according to the criteria developed in Chapter 2 (BBG selection). As discussed in Chapter 2, the break is observed in the near infrared colors of post-starburst galaxies in deep HST/WFC3 observations in the GOODS fields. As discussed earlier, the SED inferred properties of these systems are consistent with being old and massive with average ages of  $\sim 0.8$  Gyr and average stellar masses of  $5 \times 10^{10}$  at  $z \gtrsim 3 - 4$ .

### 5.2.2 Star forming Candidates

The star forming candidates are selected as Lyman Break Galaxies (LBGs; Madau et al., 1996; Steidel et al., 1996, 1999, 2003; Giavalisco et al., 2004a; Bouwens et al., 2007; Beckwith et al., 2006) as bdrop and vdrop candidates based on the criteria developed in Stark et al., 2009 at  $z \sim 3 - 5$ . This technique is based on the change in the broadband color of distant

galaxies as the rest-frame UV light short-ward of the Lyman limit (at  $912\text{\AA}$ ) emitted by these systems is absorbed by the neutral Hydrogen.

The second sample of star forming galaxies are selected as Lyman Alpha Emitting (LAE) systems. These objects are highly star forming systems that are identified through narrow band observations targeting the Lyman- $\alpha$  emission at  $1216\text{\AA}$  (Mallery et al., 2012). Our sample of narrow band selected galaxies are from narrowband observations selecting these systems at  $z \sim 4 - 5$ .

I use spectroscopic data from the W.M. Keck Observatory along with photometric data from Hubble Space Telescope, Spitzer and other ground based observatories for this study. In this section I will present the data in more detail.

### 5.2.3 Spectroscopic Data

The spectroscopic data for this study are from observations by the Deep Extragalactic Imaging Multi-Object Spectrograph <sup>1</sup> (DEIMOS; Faber et al., 2003) on Keck telescope. DEIMOS is an optical multi-object spectrograph, with wavelength coverage of  $4100-11000\text{\AA}$ , mounted on a Nasmyth platform on the Keck II 10m telescope. It has a field of view of  $3.6' \times 3.6'$  over one guider with typical alignment accuracy of  $0.1''$ . In its low resolution mode DEIMOS can reach a predicted S/N=5 on an object with  $V=24.0$  in only one hour <sup>2</sup>.

In this study, the observations are from a series of runs from March 2011 to January 2014. In all the runs I used 600 and 830 lines/mm gratings with wavelength ranges of  $5300\text{\AA}$  and  $3840\text{\AA}$  respectively. The 830 grating would give a better spectral resolution than the 600 grating ( $2.5\text{\AA}$  vs.  $3.5\text{\AA}$ ) but it has a shorter wavelength coverage. The central wavelength in each run is chosen to maximize the number of candidates on each mask given the photometric redshifts. The DEIMOS observations are summarized in Table 5.1.

---

<sup>1</sup><http://www2.keck.hawaii.edu/inst/deimos>

<sup>2</sup><http://www2.keck.hawaii.edu/inst/deimos/specs.html>

#### 5.2.4 Photometric Data

The photometric data for this study is from observations by the Cosmic Assembly Near-infrared Deep Extragalactic Legacy Survey (CANDELS: PI. S. Faber and H. Ferguson; see Grogin et al., 2011 and Koekemoer et al., 2011) in the GOODS fields. The GOODS fields also have very deep observations by the Spitzer Space Telescope IRAC instrument (Fazio et al., 2004) in the 3.6  $\mu\text{m}$ , 4.5  $\mu\text{m}$ , 5.8  $\mu\text{m}$  and 8.0  $\mu\text{m}$  bands. The photometric data used in this study are further described in Chapter 1.

### 5.3 Analyzing the Spectroscopic Data

The spectra of both the quiescent and star forming galaxies were analyzed in the same way with the same raw data handling procedure and analysis. In this section I will describe the Keck DEIMOS spectroscopic data analysis.

#### 5.3.1 Spectroscopic Data Reduction

The raw spectroscopic data acquired from the telescope are reduced using the DEIMOS pipeline (in IDL) developed by the DEEP2 team <sup>3</sup>. The pipeline uses the flat field images acquired during the calibration phase of the observing to create a flat field subtracted image. The Kr, Ne and Ar arc lamp data is used by the pipeline to calculate a wavelength solution used to wavelength calibrate the spectra. The pipeline combines the different exposures of a single mask and provide 2D spectra for the whole mask and for individual objects. The procedure *extract1d* is then used to extract the 1D spectra from the 2D data using both boxcar and optimal extraction according to Horne, 1986.

In this work I use a modified version of the reduction pipeline which is changed to handle dithering of the spectra. When using the 830G grating I dither by  $\sim 2''$  along the slit to get a better sky subtraction. The dithered pipeline uses the shift on the bright stars in

---

<sup>3</sup><http://deep.ps.uci.edu/spec2d>

the mask to automatically determine the dithering pattern and to combine the different exposures correctly. Figure 5.1 shows example 1D and 2D reduced DEIMOS spectra.

### 5.3.2 Spectroscopic Redshift Assignments

The spectroscopic redshift of the candidates are assigned based on several prominent emission and/or absorption features. At the redshifts of interest here we are looking at the rest-frame UV of the galaxies. The most important features that we look at are the Ly $\alpha$  resonance line at 1216 Å and the low and high ionization metal lines such as SiII (1260 Å), OI (1302 Å), CII (1334 Å) SiIV (1393 Å and 1402 Å) and CIV (1548 Å and 1550 Å).

The redshift is assigned by a combination of the these lines. In most cases the star forming galaxies are identified through a combination of the Lyman- $\alpha$  feature and the strong and/or weak metal absorption lines. These absorption lines are absent in some of the star forming galaxies in which we rely on the Lyman- $\alpha$  line alone to assign the redshift. The spectroscopic redshifts for the BBGs are assigned mostly from the metal absorption lines (due to lack of emission features) and in a few cases by the combination of absorption and Lyman- $\alpha$  emission feature.

The spectroscopic redshifts were assigned based on a scheme of 0-4 in the confidence level with 4 being the most confident and 0 the least confident spectroscopic redshifts. A confidence level 0 is assigned when we basically cannot infer a redshift. This happens when no distinct emission and/or absorption feature is identified in the 1D and 2D spectra. A 1 or 2 is given if I can identify very faint emission/absorption features (usually at  $\sim 2-3\sigma$  level) in the spectra. A confidence level 3 is assigned when I confirm several spectroscopic features in the 1D spectra that sometime do not have 2D counterparts (which mostly happens for the faint continuum absorption features). Finally I assign a confidence 4 spectroscopic redshift to an object for which I could clearly see prominent emission and/or absorption features in the 1D and 2D spectra.

The spectroscopic redshifts assigned in this way may be different from the true redshift of the galaxies. It has been shown by several studies that the high redshift systems could

spec1d.zd-1.040.pz-755119.fits :  $z = 4.75306$

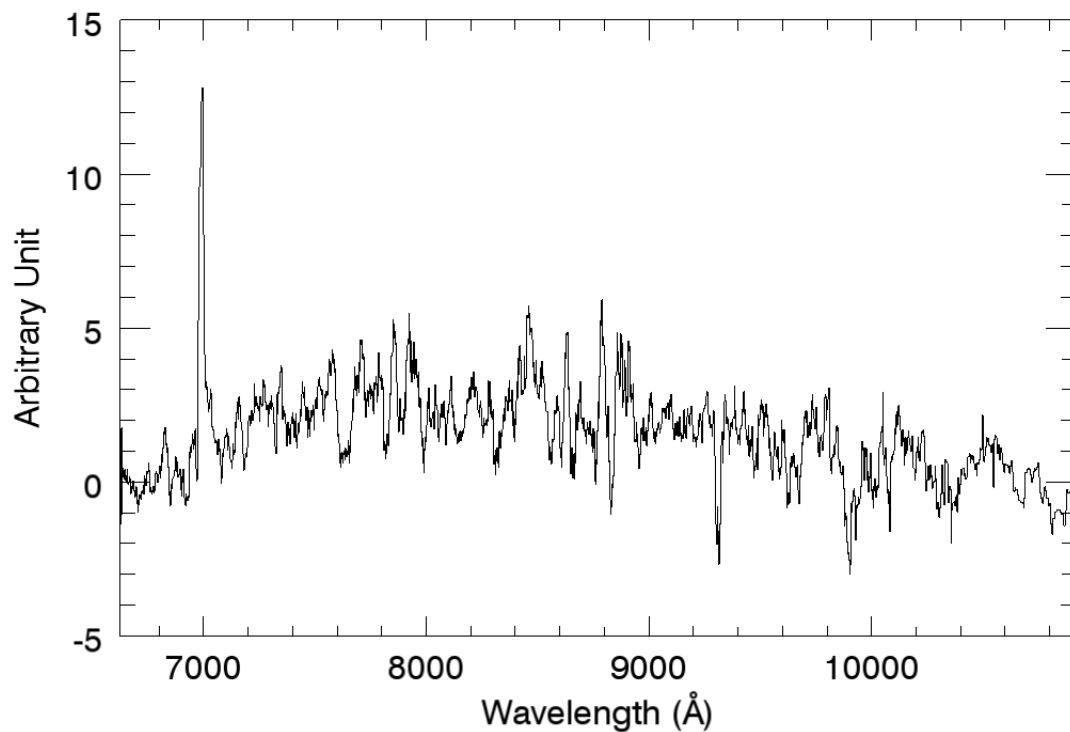


**Figure 5.1:** Reduced DEIMOS 1D and 2D spectra of a sample galaxy at  $z \sim 4.5$ . The Ly $\alpha$  emission at 6994  $\text{\AA}$  is visible in both spectra.

potentially host strong outflows (or inflows) and winds that would reflect itself in the rest-frame UV spectra by producing a redshift in the Ly- $\alpha$  feature and blueshift in several of the absorption features (Shapley et al., 2003). The true systemic redshift of the galaxies could technically be determined from the stellar photospheric features such as CIII (1176 Å) and OIV (1343 Å) or from nebular emission lines (such as H $\alpha$  or H $\beta$ ) which are usually produced at rest with respect to stars in the galaxy. In reality, however, the photospheric features are far too weak to be detected in individual spectra of star forming and passive galaxies. The detection of nebular emission lines usually require near-infrared and infrared observations of these high redshift systems which might not exist for large samples of high redshift systems. In order to address this one could derive recipes for calculating the systemic redshift from UV spectral features for galaxies for which I already have observed nebular emission lines from near infrared spectroscopy. Using a large sample of high redshift galaxies Adelberger et al., 2005 derived the following relations for systemic redshift measurements from UV spectra:

$$z_{sys} = z_{Ly\alpha} - 0.0033 - 0.0050(z_{Ly\alpha} - 2.7) \quad (5.1)$$

for galaxies for which I only use the Ly $\alpha$  to assign redshifts,

$$z_{sys} = z_{ISM} + 0.0022 + 0.0015(z_{ISM} - 2.7) \quad (5.2)$$

for redshifts that use interstellar absorption features and

$$z_{sys} = \bar{z} + 0.07\Delta z - 0.0017 - 0.0010(\bar{z} - 2.7) \quad (5.3)$$

In this work I will use the equations by Adelberger et al., 2005 (discussed above) to derive the systemic redshift of the star forming and passive galaxies. I will further discuss the implications of this choice for the star forming and passive galaxies in the last section.

### 5.3.3 Comparing the Photometric and Spectroscopic Redshifts

I measured the photometric redshift for our sample of LBG, LAE and BBG selected galaxies using the multi-waveband photometry available in the GOODS fields. This is done by fitting the observed spectral energy distribution of the candidates with a template library of model galaxy SEDs (SED fitting) and minimizing the  $\chi^2$  in the fit. The SED fitting method is further described in Dahlen et al., 2013.

Figure 5.2 shows the comparison of the photometric redshifts and spectroscopic redshifts for our passive and star forming samples. To quantify the scatter in the redshifts, I estimate the ratio  $\Delta z/(1 + z_{spec})$ , where  $\Delta z = z_{spec} - z_{phot}$ . I define catastrophic redshift outliers as objects with  $|\Delta z|/(1 + z_{spec}) > 0.3$ . Comparing with the spectroscopic sample with the highest confidence levels, the difference between the photometric and spectroscopic redshifts has a standard deviation of 0.21 and there are approximately 10% of the sources with the catastrophic photometric redshifts as defined above.

### 5.3.4 Stacking the Spectra

The individual spectra of galaxies are shifted to the rest-frame using the inferred spectroscopic redshifts and are coadded by an inverse variance weighting:

$$f_{stack} = \frac{ivar_1 \times f_1 + \dots + ivar_n \times f_n}{ivar_1 + \dots + ivar_n}, \quad f_1, \dots, f_n : \text{Individual Spectra} \quad (5.4)$$

The individual spectra are obtained under different conditions, with different wavelength coverage and gratings of different resolutions. In order to take this into account during the stacking process, I defined a wavelength grid spanning the range of 1150 Å to 1650 Å with a wavelength resolution of 0.25 Å. The spectra are then transferred to this grid for the stacking. The individual spectra are normalized to the strength of the Lyman- $\alpha$  emission at 1216 Å. This normalization does not affect our later inferred results of velocity offset equivalent width measurements as I have already wavelength calibrated the spectra and I will also be dealing with relative ratios of the fluxes and not the absolute values in each

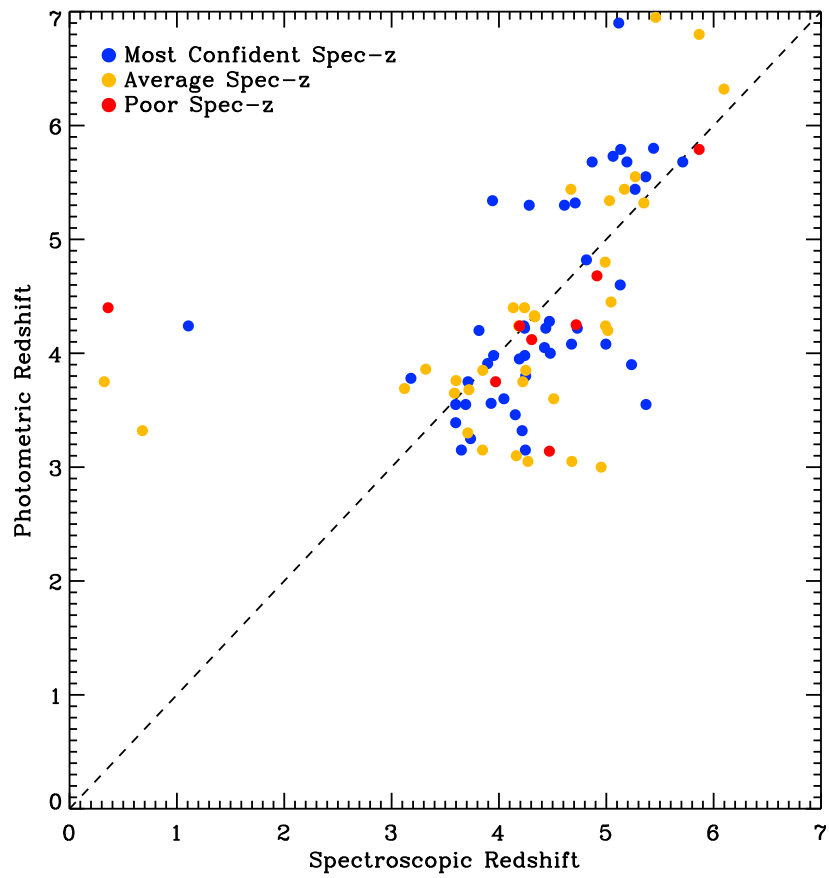


**Figure 5.2:** The photometric and spectroscopic redshift comparison for the passive galaxy candidates. The plot is color coded in terms of the assigned spectroscopic redshift confidence.

band. Figure 5.3 shows the stacked spectra of the BBG, LBG and LAE selected systems and Tables 5.2-5.5 list the spectroscopic objects used for the BBG, LBG and LAE stacks.

## 5.4 Spectroscopic Properties of the Passive and Star Forming Systems

The bimodality in the galaxy population is evident in the local Universe with the clear separation of the star forming galaxies from the early type elliptical galaxies (Williams et al., 2009). These differences are visible in the spectroscopic properties of the high redshift LBG and BBG selected sample. The two most important measureable features of our stacked spectra of star forming and passive galaxies are I. the strength of the emission and absorption features and II. the relative velocity offsets between the absorption and emission features. The strength are measure from the corresponding equivalent width of the lines and I measure the velocity offsets from the estimated spectroscopic redshifts for each of the wavelength calibrated features. In this section I will discuss these in more detail.

### 5.4.1 Equivalent Width Measurements and Velocity Offsets

The equivalent width is an estimate of the strength of an emission or absorption feature in the spectra of galaxies with respect to the underlying continuum. I measure the equivalent width of the prominent Lyman- $\alpha$ , low ionization and high ionization features in the stacked spectra of the BBG, LBG and LAE selected samples using the following equation:

$$dW_{\lambda}^{EW} = (1 - F_{\lambda}/F_{cont})d\lambda \quad (5.5)$$

For each of the spectral features I fitted a Gaussian according to the following equation to determine the line center and FWHM:

$$F(\lambda) = Ae^{-(\lambda-\lambda_{center})/2\sigma^2} + \lambda^{\beta} \quad (5.6)$$

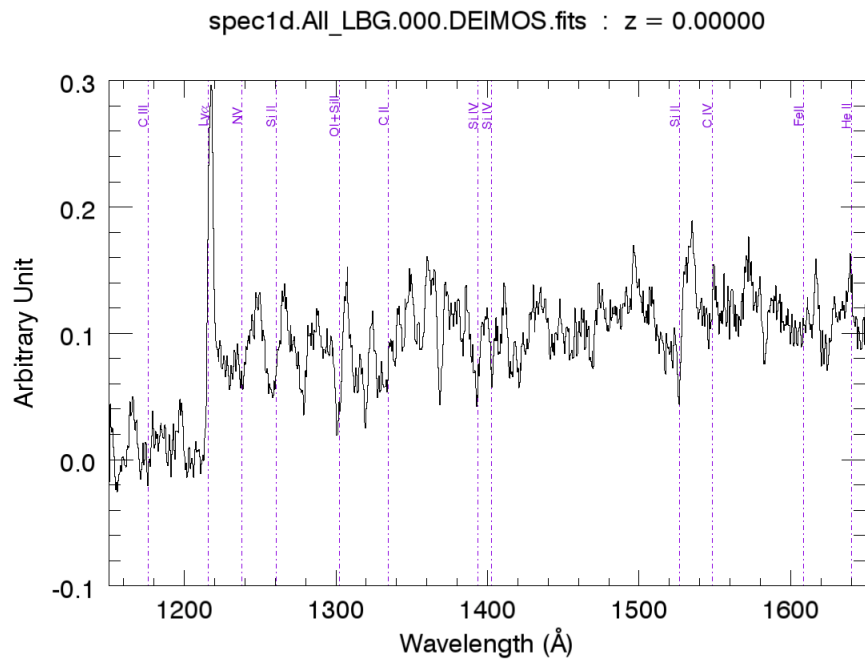
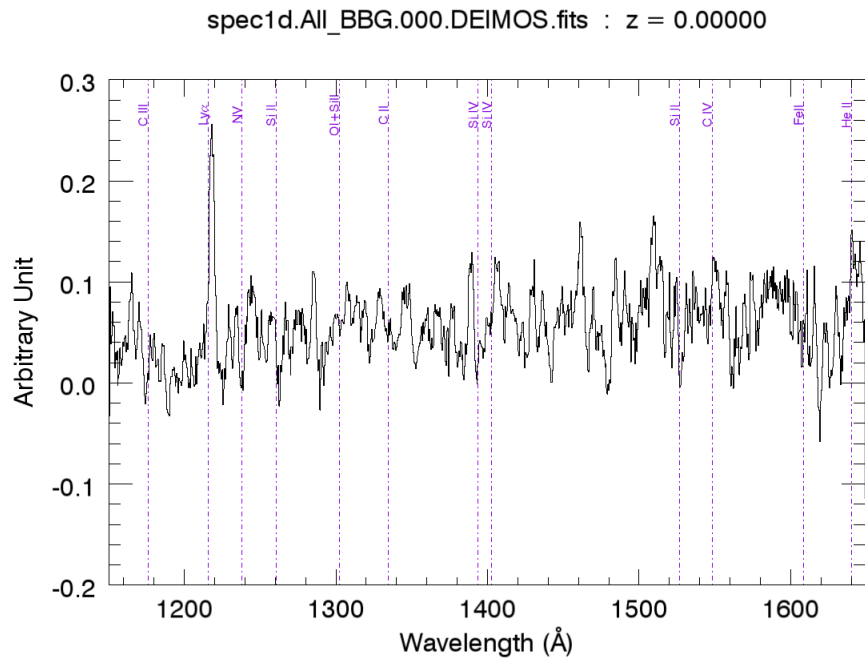


**Figure 5.3:** The stacked spectra of quiescent (BBG selected) and star forming (LBG and LAE) galaxies at  $z > 3$ .

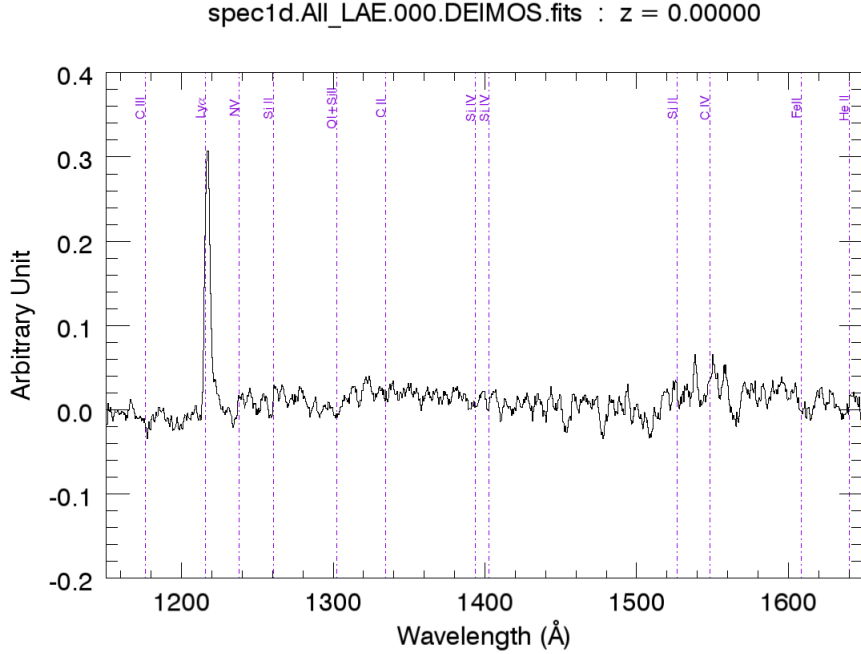
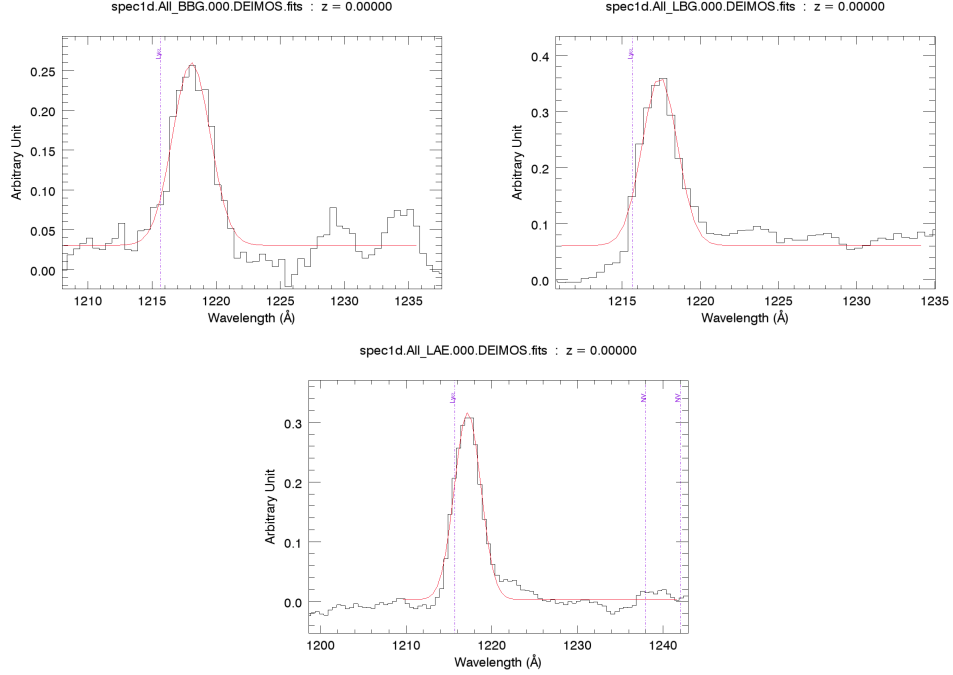


Figure 5.3: Continued.

where  $\lambda_{center}$  is the wavelength that I report for the feature. The underlying continuum is determined by simultaneously fitting a  $f(\lambda) = \lambda^\beta$  to the Gaussian function. The equivalent width is measured by integrating equation 4.1 across the feature using the values measure from the Gaussian fit and is reported as a negative number for the absorption features and a positive number for the emission features.

The Lyman- $\alpha$  EW is largest in the stacked LAE and BBG spectra. The estimated continuum is also much fainter in the LAE and BBG spectra compared to the LBG sample. Figure 5.4 shows the Ly- $\alpha$  feature for the BBG, LBG and LAE spectra with the fitted skewed Gaussian functions.

The strength of the detected low ionization features in the BBG and LBG spectra are comparable within the error. The high ionization SiIV (1393.8 Å and 1402.8 Å) absorption is marginally more prominent in the BBG spectra compares to the LBG spectra and it is marginally detected in the LAE spectra. Figure 5.5 and 5.6 show the high ionization and low ionization absorption features in the BBG and LBG stacked spectra with the corresponding



**Figure 5.4:** The Lyman- $\alpha$  emission in the stacked spectra of BBG, LBG and LAE galaxies. We see that Ly $\alpha$  is shifted with respect to the systemic redshift of the galaxy.

Gaussian fits used for EW measurement.

I measure the velocity associated with the redshift (in Minkowski space) using the following redshift-radial velocity relation:

$$(1 + z) = \sqrt{\frac{1 + \gamma}{1 - \gamma}}, \quad \gamma = v/c \quad (5.7)$$

such that the velocity offsets between two lines would be given by:

$$\Delta v_{em-abs} = c \frac{(1 + z_{em})^2 - 1}{(1 + z_{abs})^2 + 1} \quad (5.8)$$

where  $z_{em}$  is the redshift associated with the emission feature (mostly Ly- $\alpha$  and  $z_{abs}$  is the redshift associated with the low and high ionization metal absorption features. The CIII absorption feature (in the stacked spectra at 1176Å) should be tracing the systemic redshift of the galaxies. From the stacked BBG, LBG and LAE spectra I see that the CIII absorption is very close to the systemic redshift of the galaxy predicted by (Adelberger

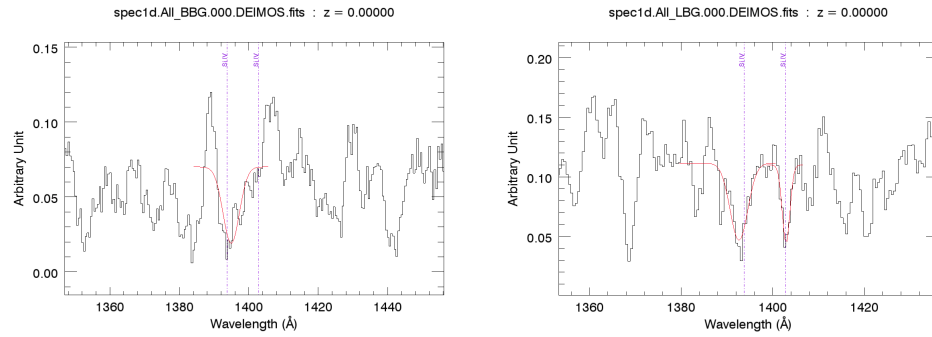


Figure 5.5: The high ionization absorption in the stacked spectra of BBG, LBG and LAE galaxies.

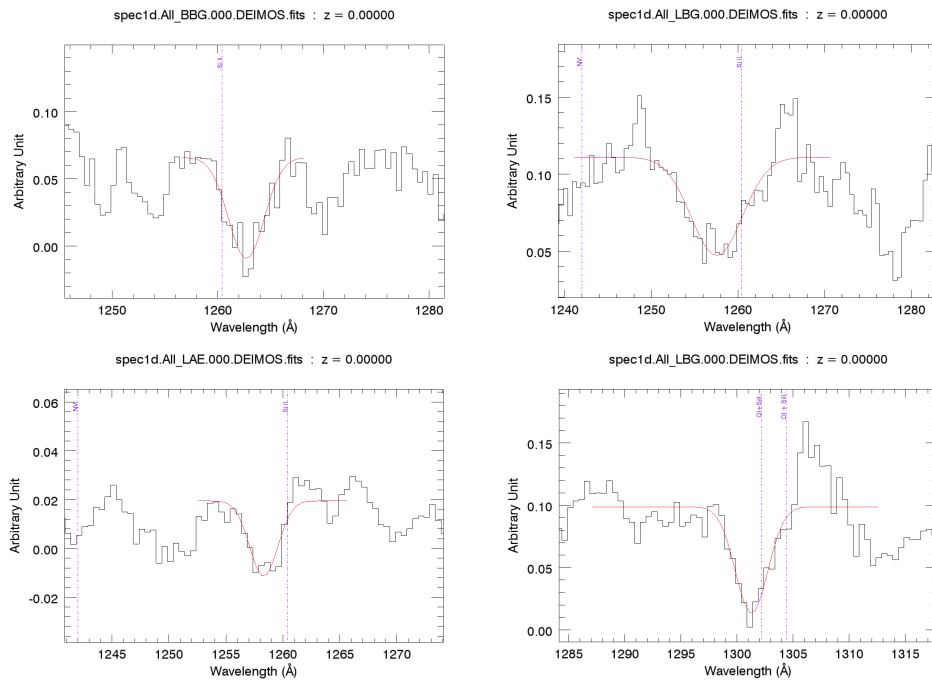


Figure 5.6: The low ionization absorption in the stacked spectra of BBG, LBG and LAE galaxies.

et al., 2005). The agreement is relatively good for the stacked LBG and LAE spectra (to *lsim* 100 km/s) while the BBG stacked spectra show small offsets of  $\sim 180$  km/s. This seems to indicate that the recipe used to derive systemic redshift of star forming galaxies from their UV spectra (based on near infrared nebular line observations) might not be very accurate for the relatively passive BBGs. I will return to this point further in the discussion.

The Ly $\alpha$  shows redshifted emission with the respect to the systemic redshift in the stacked spectra. The velocity offsets for the LBG and LAE sample are  $\sim 280$   $kms^{-1}$ . For the BBG stacked spectra I get a Ly $\alpha$  velocity offset (with respect to the systemic redshift) of  $\sim 550$   $kms^{-1}$ . The low ionization absorption features in the LBG spectra have blueshifted velocity offsets of  $\sim 200 - 300$   $kms^{-1}$ . These would produce velocity offsets of  $\Delta v_{em-abs} = 500 - 600$   $kms^{-1}$  between the emission and absorption features for the LBGs consistent with recent studies (Shapley et al., 2003; Steidel et al., 2010). The stacked BBG spectra show low ionization absorption features that are at rest or slightly redshifted with respect to the systemic redshift of the galaxy. I will get back to these results further in the discussion.

#### 5.4.2 Error Estimation For the Stacked Spectra

The DEIMOS reduction pipeline gives the inverse variance of the extracted 1D spectra as a function of wavelength. This inverse variance was used to generate the stacked spectrum for the LBG and BBGs. The wavelength dependent inverse variance can also be used to estimate the wavelength dependent standard deviation for the stacked spectra. I used this estimated error to assess the authenticity of a given feature based on the estimated signal-to-noise. This becomes particularly important for the absorption features in the stacked spectra as we discuss further in the next section. Using the measured error, the stacked BBG spectrum of the sources that have UV continuum in the individual spectra shows a 3  $\sigma$  detection in the SiIII line at 1260 Å. The error gets larger for the red part of the spectrum and the signal-to-noise is lower for the absorption features at the red side. Figure 5.7 shows the stacked BBG spectrum with the standard deviation shown in green.

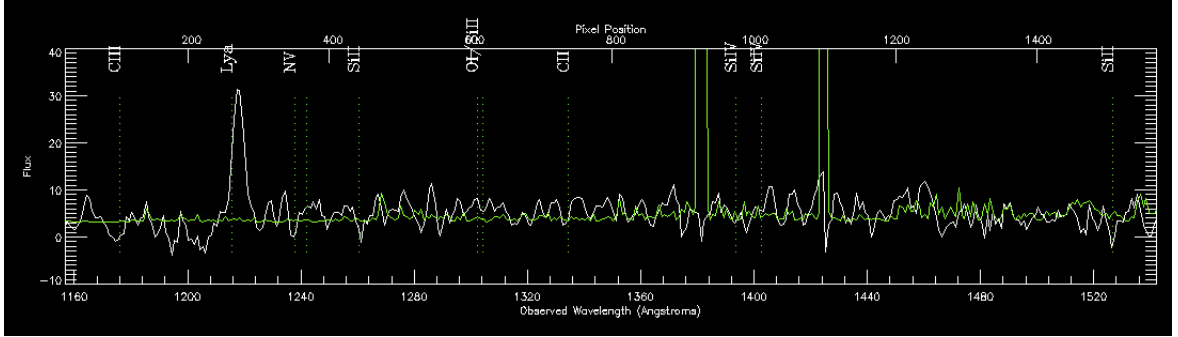


**Figure 5.7:** The stacked BBG spectrum with the standard deviation shown in green. The SiII absorption (1260 Å) is detected with  $\sim 3\sigma$ .

### 5.4.3 Caveats

The BBGs at  $z \sim 3$  are relatively faint in the optical bands (rest-frame UV) by selection and get bright in the near infrared and infrared bands. These systems usually lack the very strong UV continuum characteristic of star forming galaxies. This would make UV spectroscopic observations of these systems particularly challenging. However, the BBGs are selected as post-starburst galaxies which, as discussed in Chapter 3, could still have residual star formation that could produce Ly- $\alpha$  emission to be targeted for spectroscopy. In absence of bright continuum, it is always relatively easier to pick emission lines than absorption features and as such our most confident BBGs are identified from emission features (in particular Ly- $\alpha$ ).

We do not detect a UV continuum in the individual BBG spectra listed in Table 5.2 but three of them. The lower confidence BBGs are in fact the sources that did not have a detectable continuum *and* did not have any pronounced emission features. This lack of UV emission in the spectra of these systems (although promising as it would further confirm the passive evolution) makes both feature identification and quantitative feature measurements (at outlined above) more uncertain. This gets particularly problematic for the UV features that fall towards the red-side of the DEIMOS wavelength coverage (such as CIV, AIII and FeII) as we would get dominated by sky line emissions at the redder end of the spectra.

One additional source of uncertainty, particularly in the analysis of the velocity offsets of the different low and high ionization ISM features, is the assumption that we made

to derive the systemic redshifts for the BBGs. The recipe used in Equations 5.1-5.3 are originally developed from UV and optical observations of star forming galaxies with known velocity offsets from systemic from optical nebular line observations. Given that our BBGs showed distinct photometrically derived properties (in particular mass and age from SED fits; Chapter3) these relations might not necessarily hold for systemic redshift measurements for our sample. One way to address is to perform deep near infrared (rest-frame optical) observations of these systems. We will get back to this later in this work.

## 5.5 Discussion

The prominent observed spectral properties of LBG selected star forming galaxies is understood to some extent for some time (Steidel et al., 1999; Shapley et al., 2003). These works usually involve studying the spectroscopic properties of a stack of large number of star forming galaxies at different redshifts. Using a very large sample of LBG selected star forming galaxies Shapley et al., 2003 discussed that the spectra of star forming galaxies show strong evidence of outflowing cold and neutral and hot and ionized gas at velocities of a few hundred  $km/s$ . These outflows of cold neutral matter could sometimes extent for a few hundred kpc out of the galaxy and into the circumgalactic medium as suggested by galaxy pair studies (Steidel et al., 2010). The studies also indicate that there is a relation between the strength of the  $Ly\alpha$  emission and the strength of the neutral ISM absorption features such that star forming galaxies with the strongest  $Ly\alpha$  emission have weaker absorption features and bluer UV continuum.

The high confidence BBG spectra are mostly identified through  $ly\alpha$  emission as it is much easier to identify emission line than absorption features in faint spectra. The stacked BBG spectra shows stronger  $Ly\alpha$  emission compared to the stacked LBG spectra. This could be attributed to the intrinsic faintness of the BBGs in the restframe UV and the fact that the most confident BBGs might be biased against sources with weaker  $Ly\alpha$  emission.

In the stacked LBG spectra the velocity offsets of the low ionization absorption features

(from the systemic) and the offsets between the emission and absorption features ( $\Delta v_{em-abs}$ ) is consistent in general with recent studies of star forming galaxies at similar redshifts (Shapley et al., 2003). These velocity offsets usually indicate cold matter outflows in star forming galaxies. The similarities in the outflow velocities of the reddest and bluest parts of the Ly $\alpha$  emission and absorption features also seem to suggest a relatively symmetric distribution of outflowing cold gas around these systems as discussed in previous studies (Steidel et al., 2010).

Another notable difference in the spectra of BBGs is the strength of the metal absorption features. Comparing the measured EW of the most prominent absorption features in the stacked BBG spectra to that of the LBG selected star forming systems seem to be slightly stronger than the same absorption features in the LBG stacked spectra although I could not draw strong conclusions from this given the uncertainties that exist in the continuum estimation for these UV faint galaxies. One interesting feature detected in the stacked spectra of the BBGs is the iron absorption (FeII). This absorption feature has an EW of  $\sim 2\text{\AA}$  in the stacked BBG and is absent in our LBG spectra. Although this absence is most likely due to our limited sample LBG size, the fact that I do not see the feature with this strength in the stacked LBG sample of Shapley et al., 2003 ( $EW_{FeII} = -0.9$ ) seems to indicate that the ISM of these systems might be more enriched with heavier metals. Larger samples of high redshift relatively quiescent systems is needed in the restframe UV and optical (with near infrared spectrographs) to study any existing trends in more detail.

Table 5.1: The Keck/DEIMOS Observations Summary.

Mask ID	Field	Observing Date	Central Wavelength (Å)	Filter	Grating (1/mm)	Exposure Time (Sec.)
hdf11a	GOODS-N	2011 Mar 31-Apr 2	7500	GG455	600	21600
hdf11b	GOODS-N	2011 Mar 31-Apr 2	7500	GG455	600	21600
hdf11c	GOODS-N	2011 Mar 31-Apr 1	7500	GG455	600	14600
hdf11d	GOODS-N	2011 Apr 2	8100	OG550	830	7200
cdf11a	GOODS-S	2011 Nov 26	7500	GG455	600	7200
hzc-1	COSMOS	2011 Nov 26	7900	OG550	830	4200
uds11a	UDS	2011 Nov 24	8350	OG550	830	2700
zd1	COSMOS	2011 Nov 24 & 26	8350	OG550	830	14400
C5N1a	COSMOS	2012 Feb 26	7500	GG455	600	14400
C5N2	COSMOS	2012 Feb 24	8000	OG550	830	12600
hdf12b	GOODS-N	2012 Feb 24 & 25	8350 & 8500	OG550	830	34068
hdf321	GOODS-N	2012 Mar 22 & 23	8500	OG550	830	21600
gn+40	GOODS-N	2012 Dec 16 & 17	7350	GG495	600	16500
gs-30	GOODS-S	2012 Dec 17-19	8100	OG550	830	21600
gs+10	GOODS-S	2012 Dec 17-19	8100	OG550	830	12600
c-mosf	COSMOS	2013 Dec 25 & 2014 Jan 2	7500	GG455	600	18600
f-cos1	COSMOS	2014 Jan 2	7500	GG455	600	7200

**Table 5.2:** List of the high confidence BBG selected old and massive systems.

Source ID	RA	DEC	Mask	Spec-z (Ly- $\alpha$ )	Spec-z (Metal Absorption)	Spec-z (Systemic)
BBG_16090	03:32:28.00	-27:50:23.1	cdf11a	4.7182	-99.00	4.7048
BBG_20426	03:32:31.82	-27:45:8.5	cdf11a	3.9738	3.9675	3.9681
BBG-81185	09:58:40.85	+01:48:46.9	hzc-1	5.0298	5.0212	5.0220
bbg_08076	02:17:15.55	-27:13:48.3	uds11a	5.4112	5.4113	5.4068
BBG_22520	12:37:1.63	+62:19:20.5	hdf12b	4.9109	-99.00	4.8966
BBG_15119	12:36:42.86	+62:07:58.2	hdf12b	5.8686	5.8526	5.8569
1643_BBG	12:35:57.44	+62:14:8.8	gn+40	4.1944	-99.00	4.1836
7692_BBG	12:36:22.13	+62:15:58.7	gn+40	4.4763	-99.00	4.4641
26001_BBG	12:37:11.48	+62:20:21.0	gn+40	4.3025	4.3025	4.2991

**Table 5.3:** List of lower confidence BBGs.

Source ID	RA	DEC	Mask	Spec-z (Ly- $\alpha$ )	Spec-z (Metal Absorption)	Spec-z (Systemic)
BBGlz10046	12:36:29.25	+62:11:35.7	hdf11a hdf11b hdf11c hdf11d	4.1832	4.1917	4.1836
BBG_4057	03:32:16.56	-27:48:25.8	cdf11a	4.9882	4.9882	4.9842
HZBBG_10245	03:32:16.28	-27:43:43.2	cdf11a	5.8654	5.8654	5.8605
BBG-1010033	10:00:18.33	+02:11:10.0	CSN1a	-99.00	4.4548	4.4596
20168_BBG	03:32:23.15	-27:45:25.5	gs-30	4.9606	4.9483	4.9513
6357_BBG	03:32:41.00	-27:46:31.5	gs+10	-99.00	4.6592	4.6643
10968_BBG	03:32:39.37	-27:43:12.4	gs+10	5.0195	5.0074	5.0103
5678	03:32:35.55	-27:47:3.9	gs+10	4.2672	4.2672	4.2639
4827	03:32:33.07	-27:47:44.0	gs+10	-99.00	4.2468	4.2513
BBGlz15382	12:36:43.63	+62:17:9.6	hdf11b	3.7100	3.7100	3.7072
BBG_24737	12:37:7.74	+62:15:37.5	hdf321	-99.00	4.6700	4.6751
BBG_26913	12:37:13.85	+62:20:12.5	hdf321	-99.00	4.9912	4.9968
BBG-69943	09:58:38.32	+01:45:43.0	hzc-1	-99.00	3.7600	3.7637
BBG_14862	12:36:42.18	+62:11:12.1	hdf12b	4.6199	4.6110	4.6124

**Table 5.4:** List of the star forming LBG selected galaxies.

Source ID	RA	DEC	Mask	Spec-z (Ly- $\alpha$ )	Spec-z (Metal Absorption)	Spec-z (Systemic)
BD_22668	12:37:1.97	+62:12:25.3	hdf11a	3.4100	3.4057	3.4057
BD_21454	12:36:59.10	+62:12:23.7	hdf11a	4.0578	4.0517	4.0521
PROBZ_BD_37352	12:37:49.76	+62:19:5.1	hdf11a	4.1266	4.1230	4.1219
VD2_04842	12:36:12.63	+62:09:40.2	hdf11a	5.0575	5.0400	5.0459
VDbr_16946	12:36:47.94	+62:10:20.3	hdf11b	5.6500	5.6104	5.6283
PROBZ_VD_04648	12:36:11.91	+62:14:38.5	hdf11c	5.4496	5.4404	5.4412
PROBZ_VD_20706	12:36:57.16	+62:08:13.2	hdf11c	4.7071	-99.00	4.6938
VD_11502	12:36:33.44	+62:06:40.5	hdf11c	5.05966	5.0497	5.0513
PROBZ_VD_04648	12:36:11.91	+62:14:38.5	hdf11d	5.4613	5.43800	5.4468
cl-1448860	10:00:39.12	+02:34:55.0	cc-1	5.3026	-99.00	5.2863
cl-1448863	10:00:44.65	+02:34:52.7	cc-1	5.9174	-99.00	5.8980
Finkz45_18171	03:32:30.98	-27:46:2.5	cdf11a	4.7444	4.7444	4.7406
Finkz45_16131	03:32:28.45	-27:55:11.2	cdf11a	4.2579	4.2402	4.2470
Finkz45_19001	03:32:32.07	-27:53:50.5	cdf11a	4.7154	4.7154	4.7116
COSMOS	09:58:46.83	+01:47:38.6	hzc-1	4.1101	-99.00	4.0997
Rd-754226	10:00:59.14	+02:02:8.0	zd-1	4.6229	4.6130	4.6150
Vdlz-749753	10:01:9.85	+02:04:30.1	zd-1	4.2307	-99.00	4.2198
Vdlz-763283	10:01:1.96	+01:58:20.0	zd-1	4.6299	4.6179	4.6211
m45-527720	10:01:4.11	+01:54:5.1	zd-1	4.5464	4.5266	4.5343
pz-755119	10:01:1.60	+02:01:56.6	zd-1	4.7485	4.7187	4.7319
ID_11848	12:36:34.39	+62:10:47.5	hdf12b	5.6542	-99.00	5.6361
D13162_16192	12:36:45.90	+62:11:58.2	hdf12b	5.6037	5.5839	5.5906
f192130	10:00:46.74	+02:18:42.7	c-b0B	4.8046	-99.00	4.7907
VD_01784	10:00:26.62	+02:12:6.0	cos0	4.5273	-99.00	4.5149
VD_16760	10:00:17.80	+02:22:46.8	cos0	4.7984	4.7885	4.7904
VD_18412	10:00:23.13	+02:24:2.3	cos0	4.5139	4.5139	4.5104
VD_20189	10:00:27.15	+02:25:19.5	cos0	4.6494	-99.00	4.6363
VD_21605	10:00:32.17	+02:26:29.7	cos0	4.6896	4.6797	4.6816
VD_06013	03:32:39.77	-27:51:14.9	gs-30	4.4114	-99.00	4.3995

**Table 5.5:** List of the Ly $\alpha$  emitters.

Source ID	RA	DEC	Mask	Spec-z (Ly- $\alpha$ )	Spec-z (Metal Absorption)	Spec-z (Systemic)
LAE065042_12277	12:36:35.52	+62:13:12.9	hdf11a	4.087	-99.00	4.0814
LAE042807_12621	12:36:36.45	+62:07:24.8	hdf11b	4.142	-99.00	4.1364
LAE072712_16378	12:36:46.38	+62:15:13.4	hdf11b	4.064	-99.00	4.0584
LAE090482_16247	12:36:46.04	+62:19:57.1	hdf11b	4.073	-99.00	4.0674
LAE042807_12621	12:36:36.45	+62:07:24.8	hdf11c	4.142	-99.00	4.1364
LAE077759	12:35:53.38	+62:16:31.8	hdf11c	4.024	-99.00	4.0184
LAE077759	12:35:53.38	+62:16:31.8	hdf11d	4.027	-99.00	4.0214
N8bb-44-27108	09:58:31.94	+01:49:20.2	hzc-1	5.680	-99.00	5.6743
N8bb-40-15090	10:01:7.37	+01:52:22.8	zd-1	5.670	-99.00	5.6643
N7ib-64-20263	10:00:55.43	+02:13:9.2	CSN2	4.873	-99.00	4.8673
N8ib-65-12966	10:00:48.77	+02:13:40.2	CSN2	5.710	-99.00	5.7042
N8jp-65-54	10:00:33.02	+02:15:34.9	CSN2	5.676	-99.00	5.6703

## Chapter 6

# Conclusions

### Summary

- We select relatively quiescent galaxy candidates based on their observed near infrared colors in the HST/WFC3 filters using the age dependent Balmer break in post-starburst systems to develop the BBG selection criteria. We identify 16 candidates in the GOODS-S Deep area at  $z \sim 3 - 4$ .
- The nebular emission lines play a significant role in estimating the SED inferred parameters of the BBG candidates as they could alter mass and age measurements of the potential candidates.
- There is an overlap between the BBG selection and an LBG selection in the same redshift range of study. The BBG sample which is also selected as an LBG happens to have very high SED inferred star formation rates. Also we see that the BBG selection is picking a more massive and more evolved population compared to the LBG selection.
- The most massive ( $M_{\star} > 10^{10} M_{\odot}$ ) BBG selected candidates have observed number densities of  $3.2 \times 10^{-5} Mpc^{-3}$  ( $2.5 \times 10^{-5} Mpc^{-3}$  for the MIPS non-detected sample) and observed mass densities of  $2.0 \times 10^6 M_{\odot}/Mpc^3$  ( $10^6 M_{\odot}/Mpc^3$  for the MIPS non-

detected sample) at  $z \sim 3 - 4$ . The massive quiescent candidates are less than 10% as numerous as star forming galaxies at similar redshifts and could contribute as much as 10%-40% to the mass budget of the Universe at the redshift of the survey.

- The BBG candidates have estimated average ages of  $\sim 800$  Myr. These systems must have had a passive evolution after the initial burst of star formation, which would indicate a high redshift of formation for these systems. The quiescent massive BBG candidates at  $z \sim 3 - 4$  could be the descendants of the very highly star forming galaxies found at higher redshifts.
- We spectroscopically confirm a sample of old and massive systems at  $z \gtrsim 3$  (identified through the BBG selection) using deep observations with the Keck/DEIMOS optical spectrograph.
- The BBGs individual spectra on average have very few emission lines and are usually characterized by metal low and high ionization absorption features compared to the individual LBG star forming spectra.
- The stacked BBG spectra have metal absorption features with relatively higher equivalent widths compared to the star forming LBG selected galaxies.
- The low and high ionization absorption features have blueshifted velocity offsets in the stacked LBG and are relatively at rest (with respect to systemic) in the stacked BBG signifying the role of outflows.
- We use GALFIT to measure the physical size of the old and massive galaxies by fitting single Sersic functions to the light profile of these systems.
- We study the mass-size relation for BBGs and compare that with the star forming LBG selected systems. We conclude that the size dependence on mass is much steeper for BBGs than that of the star forming systems. We also claim that this relation is steeper than that of the quiescent galaxies at lower redshifts.

- We look at the size evolution of the BBGs as a function of redshift. We see that for these systems the physical size of the galaxy gets smaller with redshift as  $R_e \propto (1+z)^{-1.48}$ . Comparing this with size measurements of star forming galaxies we find that the quiescent galaxies are 2-3 times smaller on average than the star forming galaxies at the same redshifts.

## Future Works

In this final section I will outline a few important (mostly still open) questions that I wish to explore in my future research and discuss the approach that I intend to take to answer it.

- In this study we focused on the identification of the old and massive systems in the GOODS-S field. This was mainly to take full advantage of the deepest near infrared observations available. Although this enabled us to study the properties of these systems in detail, it limited the number of sources that we could study dictated by the small area of the field. I propose to extend this study to all the rest of the CANDELS fields allowing for inherent biases present in sample selection. This provides a statistically large sample of old and massive galaxies at high redshift. I will use this to study the space density and luminosity function of these galaxies at  $z \sim 4$ . Fitting the observed SEDs of the BBGs with model templates, I will compute their stellar mass and will use that to construct the mass function. I will measure the total mass density of high redshift passively evolving galaxies from the estimated mass function. Comparing the luminosity and mass functions of the BBGs with those from the star-forming Lyman Break Galaxies (LBGs) and Lyman Alpha Emitters (LAEs) provides clues towards understanding the nature of these different populations of galaxies and in particular the contribution of each population to the total mass budget of the universe at high redshifts.

- As I discussed in Chapter 2, there seems to be a growing evidence of the presence of massive and old galaxies at even higher redshifts. I will extend the current massive and old galaxy selection technique, to higher redshifts ( $z > 6$ ) using the now available very deep data in the near and mid-infrared (WFC3 and deep IRAC SEDS). The aim here is to estimate the contribution from this population to the high redshift galaxies and extend the study of the evolution of their LF and MF to  $z \sim 7$ . The expectation is that at the highest redshifts, we find the youngest and the most star-forming galaxies. The presence of an old population, not detected through conventional techniques, at high redshifts can raise several questions in terms of our understanding of the process of galaxy evolution at the cosmic dawn (as discussed in Chapter 2).
- The massive and old BBGs currently lack near infrared (restframe optical) spectroscopic observations and as discussed in Chapter 4, this did not allow us to determine the systemic redshifts of these systems through observations of the nebular emission lines. I plan to carry out near-IR spectroscopic observations of the passively evolving galaxies observed with DEIMOS using near-IR spectrograph (Keck MOSFIRE). Studying the spectra of these galaxies at redder bands (rest-frame optical) brings a unique opportunity to explore the stellar population and physical conditions in these systems. More specifically I will be modeling the nebular emission lines and their contribution to the photometric data in galaxies and their effect on the estimated parameters (stellar mass, extinction etc). In particular comparing the UV star formation rate indicators with that of nebular emission lines gives insight into the star formation history of these galaxies at high redshifts.
- I plan to study and compare the different selection techniques used to identify the star-forming and passive galaxies at high redshift. One of the questions that I am seeking to answer is the difference between the BBG selection and old and massive candidates selected from other methods (such as the BzK). Equally interesting is the comparison of the different populations of star-forming galaxies identified by the dropout Lyman

Break techniques and the narrow band selections of Lyman Alpha Emitters. With the availability of multi wavelength photometry of high redshift galaxies, one can also use the full SED of galaxies to select the high redshift candidates (the so called photometric redshift selection). I plan to understand the differences (and similarities) of these high redshift galaxy selections using deep photometry and spectroscopy available for the populations.

# References

- Adelberger, K. L., Shapley, A. E., Steidel, C. C., Pettini, M., Erb, D. K., and Reddy, N. A.: 2005, *ApJ* **629**, 636
- Anders, P. and Fritze-v. Alvensleben, U.: 2003, *Astronomy and Astrophysics* **401**, 1063
- Ashby, M. L. N., Willner, S. P., Fazio, G. G., Huang, J.-S., Arendt, R., Barmby, P., Barro, G., Bell, E. F., Bouwens, R., Cattaneo, A., Croton, D., Davé, R., Dunlop, J. S., Egami, E., Faber, S., Finlator, K., Grogin, N. A., Guhathakurta, P., Hernquist, L., Hora, J. L., Illingworth, G., Kashlinsky, A., Koekemoer, A. M., Koo, D. C., Labbé, I., Li, Y., Lin, L., Moseley, H., Nandra, K., Newman, J., Noeske, K., Ouchi, M., Peth, M., Rigopoulou, D., Robertson, B., Sarajedini, V., Simard, L., Smith, H. A., Wang, Z., Wechsler, R., Weiner, B., Wilson, G., Wuyts, S., Yamada, T., and Yan, H.: 2013, *ApJ* **769**, 80
- Barden, M., Häußler, B., Peng, C. Y., McIntosh, D. H., and Guo, Y.: 2012, *MNRAS* **422**, 449
- Barro, G., Faber, S. M., Pérez-González, P. G., Koo, D. C., Williams, C. C., Kocevski, D. D., Trump, J. R., Mozena, M., McGrath, E., van der Wel, A., Wuyts, S., Bell, E. F., Croton, D. J., Ceverino, D., Dekel, A., Ashby, M. L. N., Cheung, E., Ferguson, H. C., Fontana, A., Fang, J., Giavalisco, M., Grogin, N. A., Guo, Y., Hathi, N. P., Hopkins, P. F., Huang, K.-H., Koekemoer, A. M., Kartaltepe, J. S., Lee, K.-S., Newman, J. A., Porter, L. A., Primack, J. R., Ryan, R. E., Rosario, D., Somerville, R. S., Salvato, M., and Hsu, L.-T.: 2013, *ApJ* **765**, 104
- Barro, G., Trump, J. R., Koo, D. C., Dekel, A., Kassin, S. A., Kocevski, D. D., Faber, S. M., van der Wel, A., Guo, Y., Perez-Gonzalez, P. G., Toloba, E., Fang, J. J., Pacifici, C., Simons, R., Campbell, R., Ceverino, D., Finkelstein, S. L., Goodrich, B., Kassis, M., Koekemoer, A. M., Konidaris, N. P., Livermore, R. C., Lyke, J. E., Mobasher, B., Nayyeri, H., Peth, M., Primack, J. R., Rizzi, L., Somerville, R. S., Wirth, G. D., and Zolotov, A.: 2014, *ArXiv e-prints*
- Beckwith, S. V. W., Stiavelli, M., Koekemoer, A. M., Caldwell, J. A. R., Ferguson, H. C.,

- Hook, R., Lucas, R. A., Bergeron, L. E., Corbin, M., Jogee, S., Panagia, N., Robberto, M., Royle, P., Somerville, R. S., and Sosey, M.: 2006, *The Astronomical Journal* **132**, 1729
- Behroozi, P. S., Wechsler, R. H., and Conroy, C.: 2013, *ApJ* **770**, 57
- Bell, E. F., van der Wel, A., Papovich, C., Kocevski, D., Lotz, J., McIntosh, D. H., Kartaltepe, J., Faber, S. M., Ferguson, H., Koekemoer, A., Grogin, N., Wuyts, S., Cheung, E., Conselice, C. J., Dekel, A., Dunlop, J. S., Giavalisco, M., Herrington, J., Koo, D. C., McGrath, E. J., de Mello, D., Rix, H.-W., Robaina, A. R., and Williams, C. C.: 2012, *ApJ* **753**, 167
- Bell, E. F., Wolf, C., Meisenheimer, K., Rix, H.-W., Borch, A., Dye, S., Kleinheinrich, M., Wisotzki, L., and McIntosh, D. H.: 2004, *ApJ* **608**, 752
- Belli, S., Newman, A. B., and Ellis, R. S.: 2014a, *ApJ* **783**, 117
- Belli, S., Newman, A. B., Ellis, R. S., and Konidaris, N. P.: 2014b, *ArXiv e-prints*
- Bertin, E.: 2010, *SWarp: Resampling and Co-adding FITS Images Together*, Astrophysics Source Code Library
- Bertin, E. and Arnouts, S.: 1996, **117**, 393
- Bezanson, R., van Dokkum, P. G., Tal, T., Marchesini, D., Kriek, M., Franx, M., and Coppi, P.: 2009, *ApJ* **697**, 1290
- Bolzonella, M., Miralles, J.-M., and Pelló, R.: 2000, *Astronomy and Astrophysics* **363**, 476
- Bouwens, R. J., Illingworth, G. D., Franx, M., and Ford, H.: 2007, *ApJ* **670**, 928
- Bouwens, R. J., Illingworth, G. D., Oesch, P. A., Trenti, M., Labbé, I., Bradley, L., Carollo, M., van Dokkum, P. G., Gonzalez, V., Holwerda, B., Franx, M., Spitler, L., Smit, R., and Magee, D.: 2014, *ArXiv e-prints*
- Brammer, G. B., Whitaker, K. E., van Dokkum, P. G., Marchesini, D., Franx, M., Kriek, M., Labbé, I., Lee, K.-S., Muzzin, A., Quadri, R. F., Rudnick, G., and Williams, R.: 2011, *ApJ* **739**, 24

- Bruzual, G. and Charlot, S.: 2003, *MNRAS* **344**, 1000
- Bundy, K., Fukugita, M., Ellis, R. S., Targett, T. A., Belli, S., and Kodama, T.: 2009, *ApJ* **697**, 1369
- Calzetti, D., Armus, L., Bohlin, R. C., Kinney, A. L., Koornneef, J., and Storchi-Bergmann, T.: 2000, *ApJ* **533**, 682
- Capak, P., Carilli, C. L., Lee, N., Aldcroft, T., Aussel, H., Schinnerer, E., Wilson, G. W., Yun, M. S., Blain, A., Giavalisco, M., Ilbert, O., Kartaltepe, J., Lee, K.-S., McCracken, H., Mobasher, B., Salvato, M., Sasaki, S., Scott, K. S., Sheth, K., Shioya, Y., Thompson, D., Elvis, M., Sanders, D. B., Scoville, N. Z., and Tanaguchi, Y.: 2008, *ApJl* **681**, L53
- Caputi, K. I., Dunlop, J. S., McLure, R. J., Huang, J.-S., Fazio, G. G., Ashby, M. L. N., Castellano, M., Fontana, A., Cirasuolo, M., Almaini, O., Bell, E. F., Dickinson, M., Donley, J. L., Faber, S. M., Ferguson, H. C., Giavalisco, M., Grogin, N. A., Kocevski, D. D., Koekemoer, A. M., Koo, D. C., Lai, K., Newman, J. A., and Somerville, R. S.: 2012, *ApJl* **750**, L20
- Cassata, P., Giavalisco, M., Williams, C. C., Guo, Y., Lee, B., Renzini, A., Ferguson, H., Faber, S. F., Barro, G., McIntosh, D. H., Lu, Y., Bell, E. F., Koo, D. C., Papovich, C. J., Ryan, R. E., Conselice, C. J., Grogin, N., Koekemoer, A., and Hathi, N. P.: 2013, *ApJ* **775**, 106
- Coleman, G. D., Wu, C.-C., and Weedman, D. W.: 1980, *ApJl Supp.* **43**, 393
- Daddi, E., Cimatti, A., Renzini, A., Fontana, A., Mignoli, M., Pozzetti, L., Tozzi, P., and Zamorani, G.: 2004, *ApJ* **617**, 746
- Dahlen, T., Mobasher, B., Dickinson, M., Ferguson, H. C., Giavalisco, M., Kretchmer, C., and Ravindranath, S.: 2007, *ApJ* **654**, 172
- Dahlen, T., Mobasher, B., Faber, S. M., Ferguson, H. C., Barro, G., Finkelstein, S. L., Finlator, K., Fontana, A., Gruetzbauch, R., Johnson, S., Pforr, J., Salvato, M., Wiklind, T., Wuyts, S., Acquaviva, V., Dickinson, M. E., Guo, Y., Huang, J., Huang, K.-H., Newman, J. A., Bell, E. F., Conselice, C. J., Galametz, A., Gawiser, E., Giavalisco, M., Grogin, N. A., Hathi, N., Kocevski, D., Koekemoer, A. M., Koo, D. C., Lee, K.-S., McGrath, E. J., Papovich, C., Peth, M., Ryan, R., Somerville, R., Weiner, B., and Wilson, G.: 2013, *ApJ* **775**, 93

- Davari, R., Ho, L. C., Peng, C. Y., and Huang, S.: 2014, *ApJ* **787**, 69
- De Lucia, G. and Blaizot, J.: 2007, *MNRAS* **375**, 2
- Dickinson, M., Bergeron, J., Casertano, S., Cesarsky, C., Chary, R.-R., Cristiani, S., Eisenhardt, P., Elbaz, D., Fall, M., Ferguson, H., Fosbury, R., Giacconi, R., Giavalisco, M., Grogin, N., Hanisch, R., Hauser, M., Hook, R., Jorgensen, I., Koekemoer, A., Ledlow, M., Livio, M., Mobasher, B., Padovani, P., Papovich, C., Reach, W., Renzini, A., Rieke, M., Rosati, P., Roth, K., Roy, J.-R., Schreier, E., Stern, D., Stiavelli, M., Takamiya, M., Tollestrup, E., Urry, M., Williams, R., Winge, C., and Wright, E.: 2004, *Great Observatories Origins Deep Survey (GOODS)*, Spitzer Proposal
- Dickinson, M., Papovich, C., Ferguson, H. C., and Budavári, T.: 2003, *ApJ* **587**, 25
- Elsner, F., Feulner, G., and Hopp, U.: 2008, *Astronomy and Astrophysics* **477**, 503
- Faber, S. M., Phillips, A. C., Kibrick, R. I., Alcott, B., Allen, S. L., Burrous, J., Cantrall, T., Clarke, D., Coil, A. L., Cowley, D. J., Davis, M., Deich, W. T. S., Dietsch, K., Gilmore, D. K., Harper, C. A., Hilyard, D. F., Lewis, J. P., McVeigh, M., Newman, J., Osborne, J., Schiavon, R., Stover, R. J., Tucker, D., Wallace, V., Wei, M., Wirth, G., and Wright, C. A.: 2003, in M. Iye and A. F. M. Moorwood (eds.), *Instrument Design and Performance for Optical/Infrared Ground-based Telescopes*, Vol. 4841 of *Society of Photo-Optical Instrumentation Engineers (SPIE) Conference Series*, pp 1657–1669
- Fakhouri, O., Ma, C.-P., and Boylan-Kolchin, M.: 2010, *MNRAS* **406**, 2267
- Fazio, G. G., Hora, J. L., Allen, L. E., Ashby, M. L. N., Barmby, P., Deutsch, L. K., Huang, J.-S., Kleiner, S., Marengo, M., Megeath, S. T., Melnick, G. J., Pahre, M. A., Patten, B. M., Polizotti, J., Smith, H. A., Taylor, R. S., Wang, Z., Willner, S. P., Hoffmann, W. F., Pipher, J. L., Forrest, W. J., McMurty, C. W., McCreight, C. R., McKelvey, M. E., McMurray, R. E., Koch, D. G., Moseley, S. H., Arendt, R. G., Mentzell, J. E., Marx, C. T., Losch, P., Mayman, P., Eichhorn, W., Krebs, D., Jhabvala, M., Gezari, D. Y., Fixsen, D. J., Flores, J., Shakoorzadeh, K., Jungo, R., Hakun, C., Workman, L., Karpati, G., Kichak, R., Whitley, R., Mann, S., Tollestrup, E. V., Eisenhardt, P., Stern, D., Gorjian, V., Bhattacharya, B., Carey, S., Nelson, B. O., Glaccum, W. J., Lacy, M., Lowrance, P. J., Laine, S., Reach, W. T., Stauffer, J. A., Surace, J. A., Wilson, G., Wright, E. L., Hoffman, A., Domingo, G., and Cohen, M.: 2004, *ApJl Supp.* **154**, 10
- Fontana, A., Salimbeni, S., Grazian, A., Giallongo, E., Pentericci, L., Nonino, M., Fontanot, F., Menci, N., Monaco, P., Cristiani, S., Vanzella, E., de Santis, C., and Gallozzi, S.: 2006, *Astronomy and Astrophysics* **459**, 745

- Fontana, A., Santini, P., Grazian, A., Pentericci, L., Fiore, F., Castellano, M., Giallongo, E., Menci, N., Salimbeni, S., Cristiani, S., Nonino, M., and Vanzella, E.: 2009, *Astronomy and Astrophysics* **501**, 15
- Franx, M., Labbé, I., Rudnick, G., van Dokkum, P. G., Daddi, E., Förster Schreiber, N. M., Moorwood, A., Rix, H.-W., Röttgering, H., van der Wel, A., van der Werf, P., and van Starkenburg, L.: 2003, *ApJl* **587**, L79
- Fu, H., Cooray, A., Feruglio, C., Ivison, R. J., Riechers, D. A., Gurwell, M., Bussmann, R. S., Harris, A. I., Altieri, B., Aussel, H., Baker, A. J., Bock, J., Boylan-Kolchin, M., Bridge, C., Calanog, J. A., Casey, C. M., Cava, A., Chapman, S. C., Clements, D. L., Conley, A., Cox, P., Farrah, D., Frayer, D., Hopwood, R., Jia, J., Magdis, G., Marsden, G., Martínez-Navajas, P., Negrello, M., Neri, R., Oliver, S. J., Omont, A., Page, M. J., Pérez-Fournon, I., Schulz, B., Scott, D., Smith, A., Vaccari, M., Valtchanov, I., Vieira, J. D., Viero, M., Wang, L., Wardlow, J. L., and Zemcov, M.: 2013, *Nature* **498**, 338
- Galametz, A., Grazian, A., Fontana, A., Ferguson, H. C., Ashby, M. L. N., Barro, G., Castellano, M., Dahlen, T., Donley, J. L., Faber, S. M., Grogin, N., Guo, Y., Huang, K.-H., Kocevski, D. D., Koekemoer, A. M., Lee, K.-S., McGrath, E. J., Peth, M., Willner, S. P., Almaini, O., Cooper, M., Cooray, A., Conselice, C. J., Dickinson, M., Dunlop, J. S., Fazio, G. G., Foucaud, S., Gardner, J. P., Giavalisco, M., Hathi, N. P., Hartley, W. G., Koo, D. C., Lai, K., de Mello, D. F., McLure, R. J., Lucas, R. A., Paris, D., Pentericci, L., Santini, P., Simpson, C., Sommariva, V., Targett, T., Weiner, B. J., Wuyts, S., and the CANDELS Team: 2013, *ApJl Supp.* **206**, 10
- Gavazzi, G., Fumagalli, M., Cucciati, O., and Boselli, A.: 2010, *Astronomy and Astrophysics* **517**, A73
- Giavalisco, M., Dickinson, M., Ferguson, H. C., Ravindranath, S., Kretchmer, C., Moustakas, L. A., Madau, P., Fall, S. M., Gardner, J. P., Livio, M., Papovich, C., Renzini, A., Spinrad, H., Stern, D., and Riess, A.: 2004a, *ApJl* **600**, L103
- Giavalisco, M., Ferguson, H. C., Koekemoer, A. M., Dickinson, M., Alexander, D. M., Bauer, F. E., Bergeron, J., Biagetti, C., Brandt, W. N., Casertano, S., Cesarsky, C., Chatzichristou, E., Conselice, C., Cristiani, S., Da Costa, L., Dahlen, T., de Mello, D., Eisenhardt, P., Erben, T., Fall, S. M., Fasnacht, C., Fosbury, R., Fruchter, A., Gardner, J. P., Grogin, N., Hook, R. N., Hornschemeier, A. E., Idzi, R., Jogee, S., Kretchmer, C., Laidler, V., Lee, K. S., Livio, M., Lucas, R., Madau, P., Mobasher, B., Moustakas, L. A., Nonino, M., Padovani, P., Papovich, C., Park, Y., Ravindranath, S., Renzini, A., Richardson, M., Riess, A., Rosati, P., Schirmer, M., Schreier, E., Somerville, R. S., Spinrad, H., Stern, D., Stiavelli, M., Strolger, L., Urry, C. M., Vandame, B., Williams, R., and Wolf, C.: 2004b, *ApJl* **600**, L93

Grogin, N. A., Kocevski, D. D., Faber, S. M., Ferguson, H. C., Koekemoer, A. M., Riess, A. G., Acquaviva, V., Alexander, D. M., Almaini, O., Ashby, M. L. N., Barden, M., Bell, E. F., Bournaud, F., Brown, T. M., Caputi, K. I., Casertano, S., Cassata, P., Castellano, M., Challis, P., Chary, R.-R., Cheung, E., Cirasuolo, M., Conselice, C. J., Roshan Cooray, A., Croton, D. J., Daddi, E., Dahlen, T., Davé, R., de Mello, D. F., Dekel, A., Dickinson, M., Dolch, T., Donley, J. L., Dunlop, J. S., Dutton, A. A., Elbaz, D., Fazio, G. G., Filippenko, A. V., Finkelstein, S. L., Fontana, A., Gardner, J. P., Garnavich, P. M., Gawiser, E., Giavalisco, M., Grazian, A., Guo, Y., Hathi, N. P., Häussler, B., Hopkins, P. F., Huang, J.-S., Huang, K.-H., Jha, S. W., Kartaltepe, J. S., Kirshner, R. P., Koo, D. C., Lai, K., Lee, K.-S., Li, W., Lotz, J. M., Lucas, R. A., Madau, P., McCarthy, P. J., McGrath, E. J., McIntosh, D. H., McLure, R. J., Mobasher, B., Moustakas, L. A., Mozena, M., Nandra, K., Newman, J. A., Niemi, S.-M., Noeske, K. G., Papovich, C. J., Pentericci, L., Pope, A., Primack, J. R., Rajan, A., Ravindranath, S., Reddy, N. A., Renzini, A., Rix, H.-W., Robaina, A. R., Rodney, S. A., Rosario, D. J., Rosati, P., Salimbeni, S., Scarlata, C., Siana, B., Simard, L., Smidt, J., Somerville, R. S., Spinrad, H., Straughn, A. N., Strolger, L.-G., Telford, O., Teplitz, H. I., Trump, J. R., van der Wel, A., Villforth, C., Wechsler, R. H., Weiner, B. J., Wiklind, T., Wild, V., Wilson, G., Wuyts, S., Yan, H.-J., and Yun, M. S.: 2011, *ApJ Supp.* **197**, 35

Gronwall, C., Ciardullo, R., Hickey, T., Gawiser, E., Feldmeier, J. J., van Dokkum, P. G., Urry, C. M., Herrera, D., Lehmer, B. D., Infante, L., Orsi, A., Marchesini, D., Blanc, G. A., Francke, H., Lira, P., and Treister, E.: 2007, *ApJ* **667**, 79

Guo, Y., Ferguson, H. C., Giavalisco, M., Barro, G., Willner, S. P., Ashby, M. L. N., Dahlen, T., Donley, J. L., Faber, S. M., Fontana, A., Galametz, A., Grazian, A., Huang, K.-H., Kocevski, D. D., Koekemoer, A. M., Koo, D. C., McGrath, E. J., Peth, M., Salvato, M., Wuyts, S., Castellano, M., Cooray, A. R., Dickinson, M. E., Dunlop, J. S., Fazio, G. G., Gardner, J. P., Gawiser, E., Grogin, N. A., Hathi, N. P., Hsu, L.-T., Lee, K.-S., Lucas, R. A., Mobasher, B., Nandra, K., Newman, J. A., and van der Wel, A.: 2013, *ApJ Supp.* **207**, 24

Guo, Y., Giavalisco, M., Cassata, P., Ferguson, H. C., Williams, C. C., Dickinson, M., Koekemoer, A., Grogin, N. A., Chary, R.-R., Messias, H., Tundo, E., Lin, L., Lee, S.-K., Salimbeni, S., Fontana, A., Grazian, A., Kocevski, D., Lee, K.-S., Villanueva, E., and van der Wel, A.: 2012, *ApJ* **749**, 149

Hilz, M., Naab, T., and Ostriker, J. P.: 2013, *MNRAS* **429**, 2924

Hopkins, A. M. and Beacom, J. F.: 2006, *ApJ* **651**, 142

Horne, K.: 1986, *Publications of the Astronomical Society of the Pacific* **98**, 609

Huang, J.-S., Zheng, X. Z., Rigopoulou, D., Magdis, G., Fazio, G. G., and Wang, T.: 2011, *ApJl* **742**, L13

Ilbert, O., McCracken, H. J., Le Fèvre, O., Capak, P., Dunlop, J., Karim, A., Renzini, M. A., Caputi, K., Boissier, S., Arnouts, S., Aussel, H., Comparat, J., Guo, Q., Hudelot, P., Kartaltepe, J., Kneib, J. P., Krogager, J. K., Le Floch, E., Lilly, S., Mellier, Y., Milvang-Jensen, B., Moutard, T., Onodera, M., Richard, J., Salvato, M., Sanders, D. B., Scoville, N., Silverman, J. D., Taniguchi, Y., Tasca, L., Thomas, R., Toft, S., Tresse, L., Vergani, D., Wolk, M., and Zirm, A.: 2013, *Astronomy and Astrophysics* **556**, A55

Iverson, R. J., Smail, I., Amblard, A., Arumugam, V., De Breuck, C., Emonts, B. H. C., Feain, I., Greve, T. R., Haas, M., Ibar, E., Jarvis, M. J., Kovács, A., Lehnert, M. D., Nesvadba, N. P. H., Röttgering, H. J. A., Seymour, N., and Wylezalek, D.: 2012, *MNRAS* **425**, 1320

Karim, A., Swinbank, A. M., Hodge, J. A., Smail, I. R., Walter, F., Biggs, A. D., Simpson, J. M., Danielson, A. L. R., Alexander, D. M., Bertoldi, F., de Breuck, C., Chapman, S. C., Coppin, K. E. K., Dannerbauer, H., Edge, A. C., Greve, T. R., Iverson, R. J., Knudsen, K. K., Menten, K. M., Schinnerer, E., Wardlow, J. L., Weiß, A., and van der Werf, P.: 2013, *MNRAS* **432**, 2

Kauffmann, G., White, S. D. M., and Guiderdoni, B.: 1993, *MNRAS* **264**, 201

Koekemoer, A. M., Faber, S. M., Ferguson, H. C., Grogin, N. A., Kocevski, D. D., Koo, D. C., Lai, K., Lotz, J. M., Lucas, R. A., McGrath, E. J., Ogaz, S., Rajan, A., Riess, A. G., Rodney, S. A., Strolger, L., Casertano, S., Castellano, M., Dahlen, T., Dickinson, M., Dolch, T., Fontana, A., Giavalisco, M., Grazian, A., Guo, Y., Hathi, N. P., Huang, K.-H., van der Wel, A., Yan, H.-J., Acquaviva, V., Alexander, D. M., Almaini, O., Ashby, M. L. N., Barden, M., Bell, E. F., Bournaud, F., Brown, T. M., Caputi, K. I., Cassata, P., Challis, P. J., Chary, R.-R., Cheung, E., Cirasuolo, M., Conselice, C. J., Roshan Cooray, A., Croton, D. J., Daddi, E., Davé, R., de Mello, D. F., de Ravel, L., Dekel, A., Donley, J. L., Dunlop, J. S., Dutton, A. A., Elbaz, D., Fazio, G. G., Filippenko, A. V., Finkelstein, S. L., Frazer, C., Gardner, J. P., Garnavich, P. M., Gawiser, E., Gruetzbauch, R., Hartley, W. G., Häussler, B., Herrington, J., Hopkins, P. F., Huang, J.-S., Jha, S. W., Johnson, A., Kartaltepe, J. S., Khostovan, A. A., Kirshner, R. P., Lani, C., Lee, K.-S., Li, W., Madau, P., McCarthy, P. J., McIntosh, D. H., McLure, R. J., McPartland, C., Mobasher, B., Moreira, H., Mortlock, A., Moustakas, L. A., Mozena, M., Nandra, K., Newman, J. A., Nielsen, J. L., Niemi, S., Noeske, K. G., Papovich, C. J., Pentericci, L., Pope, A., Primack, J. R., Ravindranath, S., Reddy, N. A., Renzini, A., Rix, H.-W., Robaina, A. R., Rosario, D. J., Rosati, P., Salimbeni, S., Scarlata, C., Siana, B., Simard, L., Smidt, J., Snyder, D., Somerville, R. S., Spinrad, H., Straughn, A. N., Telford, O., Teplitz, H. I., Trump, J. R., Vargas, C., Villforth, C., Wagner, C. R., Wandro, P., Wechsler, R. H., Weiner, B. J., Wiklind, T., Wild, V., Wilson, G., Wuyts, S., and Yun, M. S.: 2011, *ApJl*

*Supp.* **197**, 36

Kriek, M., van der Wel, A., van Dokkum, P. G., Franx, M., and Illingworth, G. D.: 2008, *ApJ* **682**, 896

Kriek, M., van Dokkum, P. G., Labbé, I., Franx, M., Illingworth, G. D., Marchesini, D., and Quadri, R. F.: 2009, *ApJ* **700**, 221

Kunth, D., Mas-Hesse, J. M., Terlevich, E., Terlevich, R., Lequeux, J., and Fall, S. M.: 1998, *Astronomy and Astrophysics* **334**, 11

Labbé, I., Huang, J., Franx, M., Rudnick, G., Barmby, P., Daddi, E., van Dokkum, P. G., Fazio, G. G., Schreiber, N. M. F., Moorwood, A. F. M., Rix, H.-W., Röttgering, H., Trujillo, I., and van der Werf, P.: 2005, *ApJl* **624**, L81

Lacey, C. and Cole, S.: 1993, *MNRAS* **262**, 627

Laidler, V. G., Papovich, C., Grogin, N. A., Idzi, R., Dickinson, M., Ferguson, H. C., Hilbert, B., Clubb, K., and Ravindranath, S.: 2007, *Publications of the Astronomical Society of the Pacific* **119**, 1325

Madau, P.: 1995, *ApJ* **441**, 18

Madau, P., Ferguson, H. C., Dickinson, M. E., Giavalisco, M., Steidel, C. C., and Fruchter, A.: 1996, *MNRAS* **283**, 1388

Madau, P., Pozzetti, L., and Dickinson, M.: 1998, *ApJ* **498**, 106

Magnelli, B., Elbaz, D., Chary, R. R., Dickinson, M., Le Borgne, D., Frayer, D. T., and Willmer, C. N. A.: 2011, *Astronomy and Astrophysics* **528**, A35

Magnelli, B., Lutz, D., Santini, P., Saintonge, A., Berta, S., Albrecht, M., Altieri, B., Andreani, P., Aussel, H., Bertoldi, F., Béthermin, M., Bongiovanni, A., Capak, P., Chapman, S., Cepa, J., Cimatti, A., Cooray, A., Daddi, E., Danielson, A. L. R., Dannerbauer, H., Dunlop, J. S., Elbaz, D., Farrah, D., Förster Schreiber, N. M., Genzel, R., Hwang, H. S., Ibar, E., Ivison, R. J., Le Floch, E., Magdis, G., Maiolino, R., Nordon, R., Oliver, S. J., Pérez García, A., Poglitsch, A., Popesso, P., Pozzi, F., Riguccini, L., Rodighiero, G., Rosario, D., Roseboom, I., Salvato, M., Sanchez-Portal, M., Scott, D., Smail, I., Sturm, E., Swinbank, A. M., Tacconi, L. J., Valtchanov, I., Wang, L., and Wuyts, S.: 2012, *Astronomy and Astrophysics* **539**, A155

- Mallery, R. P., Mobasher, B., Capak, P., Kakazu, Y., Masters, D., Ilbert, O., Hemmati, S., Scarlata, C., Salvato, M., McCracken, H., LeFevre, O., and Scoville, N.: 2012, *ApJ* **760**, 128
- Mancini, C., Matute, I., Cimatti, A., Daddi, E., Dickinson, M., Rodighiero, G., Bolzonella, M., and Pozzetti, L.: 2009, *Astronomy and Astrophysics* **500**, 705
- Marchesini, D., Whitaker, K. E., Brammer, G., van Dokkum, P. G., Labbé, I., Muzzin, A., Quadri, R. F., Kriek, M., Lee, K.-S., Rudnick, G., Franx, M., Illingworth, G. D., and Wake, D.: 2010, *ApJ* **725**, 1277
- Martig, M., Bournaud, F., Teyssier, R., and Dekel, A.: 2009, *ApJ* **707**, 250
- Mo, H. J. and White, S. D. M.: 2002, *MNRAS* **336**, 112
- Mobasher, B., Dickinson, M., Ferguson, H. C., Giavalisco, M., Wiklind, T., Stark, D., Ellis, R. S., Fall, S. M., Grogin, N. A., Moustakas, L. A., Panagia, N., Sosey, M., Stiavelli, M., Bergeron, E., Casertano, S., Ingraham, P., Koekemoer, A., Labbé, I., Livio, M., Rodgers, B., Scarlata, C., Vernet, J., Renzini, A., Rosati, P., Kuntschner, H., Kümmel, M., Walsh, J. R., Chary, R., Eisenhardt, P., Pirzkal, N., and Stern, D.: 2005, *ApJ* **635**, 832
- Mosleh, M., Williams, R. J., Franx, M., and Kriek, M.: 2011, *ApJ* **727**, 5
- Muzzin, A., Marchesini, D., Stefanon, M., Franx, M., McCracken, H. J., Milvang-Jensen, B., Dunlop, J. S., Fynbo, J. P. U., Brammer, G., Labbé, I., and van Dokkum, P. G.: 2013, *ApJ* **777**, 18
- Navarro, J. F., Frenk, C. S., and White, S. D. M.: 1996, *ApJ* **462**, 563
- Newman, A. B., Ellis, R. S., Bundy, K., and Treu, T.: 2012, *ApJ* **746**, 162
- Nonino, M., Dickinson, M., Rosati, P., Grazian, A., Reddy, N., Cristiani, S., Giavalisco, M., Kuntschner, H., Vanzella, E., Daddi, E., Fosbury, R. A. E., and Cesarsky, C.: 2009, *ApJ Supp.* **183**, 244
- Oesch, P. A., Labbé, I., Bouwens, R. J., Illingworth, G. D., Gonzalez, V., Franx, M., Trenti, M., Holden, B. P., van Dokkum, P. G., and Magee, D.: 2013, *ApJ* **772**, 136
- Ono, Y., Ouchi, M., Mobasher, B., Dickinson, M., Penner, K., Shimasaku, K., Weiner, B. J.,

- Kartaltepe, J. S., Nakajima, K., Nayyeri, H., Stern, D., Kashikawa, N., and Spinrad, H.: 2012, *ApJ* **744**, 83
- Ouchi, M., Shimasaku, K., Furusawa, H., Saito, T., Yoshida, M., Akiyama, M., Ono, Y., Yamada, T., Ota, K., Kashikawa, N., Iye, M., Kodama, T., Okamura, S., Simpson, C., and Yoshida, M.: 2010, *ApJ* **723**, 869
- Papovich, C., Moustakas, L. A., Dickinson, M., Le Floch, E., Rieke, G. H., Daddi, E., Alexander, D. M., Bauer, F., Brandt, W. N., Dahlen, T., Egami, E., Eisenhardt, P., Elbaz, D., Ferguson, H. C., Giavalisco, M., Lucas, R. A., Mobasher, B., Pérez-González, P. G., Stutz, A., Rieke, M. J., and Yan, H.: 2006, *ApJ* **640**, 92
- Peng, C. Y., Ho, L. C., Impey, C. D., and Rix, H.-W.: 2002, *The Astronomical Journal* **124**, 266
- Pérez-González, P. G., Rieke, G. H., Villar, V., Barro, G., Blaylock, M., Egami, E., Gallego, J., Gil de Paz, A., Pascual, S., Zamorano, J., and Donley, J. L.: 2008, *ApJ* **675**, 234
- Reddy, N. A. and Steidel, C. C.: 2009, *ApJ* **692**, 778
- Reddy, N. A., Steidel, C. C., Pettini, M., Adelberger, K. L., Shapley, A. E., Erb, D. K., and Dickinson, M.: 2008, *ApJ Supp.* **175**, 48
- Reed, D., Gardner, J., Quinn, T., Stadel, J., Fardal, M., Lake, G., and Governato, F.: 2003, *MNRAS* **346**, 565
- Rix, H.-W., Barden, M., Beckwith, S. V. W., Bell, E. F., Borch, A., Caldwell, J. A. R., Häussler, B., Jahnke, K., Jogee, S., McIntosh, D. H., Meisenheimer, K., Peng, C. Y., Sanchez, S. F., Somerville, R. S., Wisotzki, L., and Wolf, C.: 2004, *ApJ Supp.* **152**, 163
- Rudnick, G., Labbé, I., Förster Schreiber, N. M., Wuyts, S., Franx, M., Finlator, K., Kriek, M., Moorwood, A., Rix, H.-W., Röttgering, H., Trujillo, I., van der Wel, A., van der Werf, P., and van Dokkum, P. G.: 2006, *ApJ* **650**, 624
- Schaerer, D. and de Barros, S.: 2009, *Astronomy and Astrophysics* **502**, 423
- Schaerer, D. and de Barros, S.: 2010, *Astronomy and Astrophysics* **515**, A73
- Shankar, F., Marulli, F., Bernardi, M., Mei, S., Meert, A., and Vikram, V.: 2013, *MNRAS*

428, 109

Shapley, A. E., Steidel, C. C., Pettini, M., and Adelberger, K. L.: 2003, *ApJ* **588**, 65

Shapley, A. E., Steidel, C. C., Pettini, M., Adelberger, K. L., and Erb, D. K.: 2006, *ApJ* **651**, 688

Shen, S., Mo, H. J., White, S. D. M., Blanton, M. R., Kauffmann, G., Voges, W., Brinkmann, J., and Csabai, I.: 2003, *MNRAS* **343**, 978

Sheth, R. K., Mo, H. J., and Tormen, G.: 2001, *MNRAS* **323**, 1

Shimasaku, K., Kashikawa, N., Doi, M., Ly, C., Malkan, M. A., Matsuda, Y., Ouchi, M., Hayashino, T., Iye, M., Motohara, K., Murayama, T., Nagao, T., Ohta, K., Okamura, S., Sasaki, T., Shioya, Y., and Taniguchi, Y.: 2006, *PASJ* **58**, 313

Spitler, L. R., Straatman, C. M. S., Labbé, I., Glazebrook, K., Tran, K.-V. H., Kacprzak, G. G., Quadri, R. F., Papovich, C., Persson, S. E., van Dokkum, P., Allen, R., Kawinwanichakij, L., Kelson, D. D., McCarthy, P. J., Mehrtens, N., Monson, A. J., Nanayakkara, T., Rees, G., Tilvi, V., and Tomczak, A. R.: 2014, *ApJL* **787**, L36

Stark, D. P., Ellis, R. S., Bunker, A., Bundy, K., Targett, T., Benson, A., and Lacy, M.: 2009, *ApJ* **697**, 1493

Stefanon, M., Marchesini, D., Rudnick, G. H., Brammer, G. B., and Whitaker, K. E.: 2013, *ApJ* **768**, 92

Steidel, C. C., Adelberger, K. L., Giavalisco, M., Dickinson, M., and Pettini, M.: 1999, *ApJ* **519**, 1

Steidel, C. C., Adelberger, K. L., Shapley, A. E., Pettini, M., Dickinson, M., and Giavalisco, M.: 2003, *ApJ* **592**, 728

Steidel, C. C., Erb, D. K., Shapley, A. E., Pettini, M., Reddy, N., Bogosavljević, M., Rudie, G. C., and Rakic, O.: 2010, *ApJ* **717**, 289

Steidel, C. C., Giavalisco, M., Pettini, M., Dickinson, M., and Adelberger, K. L.: 1996, *ApJL* **462**, L17

Storey, P. J. and Hummer, D. G.: 1995, *MNRAS* **272**, 41

Straatman, C. M. S., Labbé, I., Spitler, L. R., Allen, R., Altieri, B., Brammer, G. B., Dickinson, M., van Dokkum, P., Inami, H., Glazebrook, K., Kacprzak, G. G., Kawinwanichakij, L., Kelson, D. D., McCarthy, P. J., Mehrrens, N., Monson, A., Murphy, D., Papovich, C., Persson, S. E., Quadri, R., Rees, G., Tomczak, A., Tran, K.-V. H., and Tilvi, V.: 2014, *ApJ* **783**, L14

Tacconi, L. J., Genzel, R., Smail, I., Neri, R., Chapman, S. C., Ivison, R. J., Blain, A., Cox, P., Omont, A., Bertoldi, F., Greve, T., Förster Schreiber, N. M., Genel, S., Lutz, D., Swinbank, A. M., Shapley, A. E., Erb, D. K., Cimatti, A., Daddi, E., and Baker, A. J.: 2008, *ApJ* **680**, 246

Toft, S., Smolčić, V., Magnelli, B., Karim, A., Zirm, A., Michalowski, M., Capak, P., Sheth, K., Schawinski, K., Krogager, J.-K., Wuyts, S., Sanders, D., Man, A. W. S., Lutz, D., Staguhn, J., Berta, S., Mccracken, H., Krpan, J., and Riechers, D.: 2014, *ApJ* **782**, 68

van der Wel, A., Franx, M., van Dokkum, P. G., Skelton, R. E., Momcheva, I. G., Whitaker, K. E., Brammer, G. B., Bell, E. F., Rix, H.-W., Wuyts, S., Ferguson, H. C., Holden, B. P., Barro, G., Koekemoer, A. M., Chang, Y.-Y., McGrath, E. J., Häussler, B., Dekel, A., Behroozi, P., Fumagalli, M., Leja, J., Lundgren, B. F., Maseda, M. V., Nelson, E. J., Wake, D. A., Patel, S. G., Labbé, I., Faber, S. M., Grogin, N. A., and Kocevski, D. D.: 2014, *ApJ* **788**, 28

van Dokkum, P. G., Franx, M., Kriek, M., Holden, B., Illingworth, G. D., Magee, D., Bouwens, R., Marchesini, D., Quadri, R., Rudnick, G., Taylor, E. N., and Toft, S.: 2008, *ApJ* **677**, L5

Westera, P., Lejeune, T., Buser, R., Cuisinier, F., and Bruzual, G.: 2002, *Astronomy and Astrophysics* **381**, 524

Whitaker, K. E., van Dokkum, P. G., Brammer, G., Kriek, M., Franx, M., Labbé, I., Marchesini, D., Quadri, R. F., Bezanson, R., Illingworth, G. D., Lee, K.-S., Muzzin, A., Rudnick, G., and Wake, D. A.: 2010, *ApJ* **719**, 1715

White, S. D. M. and Frenk, C. S.: 1991, *ApJ* **379**, 52

Wiklind, T., Dickinson, M., Ferguson, H. C., Giavalisco, M., Mobasher, B., Grogin, N. A., and Panagia, N.: 2008, *ApJ* **676**, 781

- Williams, C. C., Giavalisco, M., Cassata, P., Tundo, E., Wiklind, T., Guo, Y., Lee, B., Barro, G., Wuyts, S., Bell, E. F., Conselice, C. J., Dekel, A., Faber, S. M., Ferguson, H. C., Grogin, N., Hathi, N., Huang, K.-H., Kocevski, D., Koekemoer, A., Koo, D. C., Ravindranath, S., and Salimbeni, S.: 2014a, *ApJ* **780**, 1
- Williams, C. C., Giavalisco, M., Lee, B., Tundo, E., Mobasher, B., Nayyeri, H., Ferguson, H. C., Koekemoer, A., Trump, J. R., Cassata, P., Dekel, A., Guo, Y., Lee, K.-S., Pentericci, L., Bell, E. F., Castellano, M., Finkelstein, S. L., Fontana, A., Grazian, A., Grogin, N., Kocevski, D., Koo, D. C., Lucas, R. A., Ravindranath, S., Santini, P., Vanzella, E., and Weiner, B. J.: 2014b, *ArXiv e-prints*
- Williams, R. J., Quadri, R. F., Franx, M., van Dokkum, P., and Labbé, I.: 2009, *ApJ* **691**, 1879
- Wuyts, S., Labbé, I., Franx, M., Rudnick, G., van Dokkum, P. G., Fazio, G. G., Förster Schreiber, N. M., Huang, J., Moorwood, A. F. M., Rix, H.-W., Röttgering, H., and van der Werf, P.: 2007, *ApJ* **655**, 51
- Yan, H., Dickinson, M., Giavalisco, M., Stern, D., Eisenhardt, P. R. M., and Ferguson, H. C.: 2006, *ApJ* **651**, 24
- Younger, J. D., Fazio, G. G., Huang, J.-S., Yun, M. S., Wilson, G. W., Ashby, M. L. N., Gurwell, M. A., Lai, K., Peck, A. B., Petitpas, G. R., Wilner, D. J., Iono, D., Kohno, K., Kawabe, R., Hughes, D. H., Aretxaga, I., Webb, T., Martínez-Sansigre, A., Kim, S., Scott, K. S., Austermann, J., Perera, T., Lowenthal, J. D., Schinnerer, E., and Smolčić, V.: 2007, *ApJ* **671**, 1531
- Younger, J. D., Fazio, G. G., Huang, J.-S., Yun, M. S., Wilson, G. W., Ashby, M. L. N., Gurwell, M. A., Peck, A. B., Petitpas, G. R., Wilner, D. J., Hughes, D. H., Aretxaga, I., Kim, S., Scott, K. S., Austermann, J., Perera, T., and Lowenthal, J. D.: 2009, *ApJ* **704**, 803